

NAVAL POSTGRADUATE SCHOOL

MONTEREY, CALIFORNIA



DISSERTATION

**ENTRAINMENT, DETRAINMENT AND
LARGE-SCALE HORIZONTAL GRADIENTS
IN OCEANIC DEEP CONVECTION**

by

Rebecca E. Stone

June 1999

Dissertation Supervisor: Roland W. Garwood, Jr.

Approved for public release; distribution is unlimited.

DTIC QUALITY INSPECTED

19990825 074

REPORT DOCUMENTATION PAGE

Form Approved OMB No. 0704-0188

Public reporting burden for this collection of information is estimated to average 1 hour per response, including the time for reviewing instruction, searching existing data sources, gathering and maintaining the data needed, and completing and reviewing the collection of information. Send comments regarding this burden estimate or any other aspect of this collection of information, including suggestions for reducing this burden, to Washington Headquarters Services, Directorate for Information Operations and Reports, 1215 Jefferson Davis Highway, Suite 1204, Arlington, VA 22202-4302, and to the Office of Management and Budget, Paperwork Reduction Project (0704-0188) Washington DC 20503.

1. AGENCY USE ONLY (<i>Leave blank</i>)	2. REPORT DATE JUNE 99	3. REPORT TYPE AND DATES COVERED Doctoral Thesis	
4. TITLE AND SUBTITLE ENTRAINMENT, DETERAINMENT, AND LARGE-SCALE HORIZONTAL GRADIENTS IN OCEANIC DEEP CONVECTION			5. FUNDING NUMBERS
6. AUTHOR(S) Rebecca E. Stone			
7. PERFORMING ORGANIZATION NAME(S) AND ADDRESS(ES) Naval Postgraduate School Monterey CA 93943-5000			8. PERFORMING ORGANIZATION REPORT NUMBER
9. SPONSORING/MONITORING AGENCY NAME(S) AND ADDRESS(ES)			10. SPONSORING/MONITORING AGENCY REPORT NUMBER
11. SUPPLEMENTARY NOTES The views expressed in this thesis are those of the author and do not reflect the official policy or position of the Department of Defense or the U.S. Government.			
12a. DISTRIBUTION/AVAILABILITY STATEMENT Approved for public release; distribution is unlimited.		12b. DISTRIBUTION CODE	
13. ABSTRACT (<i>maximum 200 words</i>) The theory of oceanic convection and entrainment has been developed mainly in horizontally homogeneous regimes, yet large-scale spatial variability is known to control the sites and intensity of deep convection. Wintertime Greenland Sea conditions were selected to simulate convection and quantify the interplay between local forcing and large-scale gradients. Here circulation and preconditioning produce horizontal gradients in the stratification; some of the resulting stratification is conducive to the formation of thermobaric convective instabilities. A large eddy simulation (LES) model modified to include large-scale horizontal density gradients was used to study the effects of the gradients on turbulence. Horizontal turbulent kinetic energy (TKE) and scalar variances increased compared to simulations with no large-scale gradient. The additional horizontal TKE is created at scales larger than the convective plume scale. A mean horizontal circulation develops in response to the large-scale overturning. The balance between convection and overturning increases stratification in the lower region of the mixed layer, and plumes may undergo slantwise convection. One-dimensional bulk TKE model results were compared to a large eddy simulation of wintertime Greenland Sea convection. One-dimensional and LES results were similar in the distribution of TKE components and in the ratio A_R of entrainment buoyancy flux to surface buoyancy flux for the winter period modeled. The value of A_R was large because of strong shear production, 0.42 for the one-dimensional model, and 0.36 for the LES. Detraining thermobaric plumes were simulated by LES under various conditions of rotation and stratification. A critical depth h_{cr} and critical velocity w_{cr} hypothesized by Garwood et al. (1994) were shown to be predictors for onset of detrainment. The skewness of vertical velocity in a horizontal slice just below the mixed layer is shown to be an indicator for detrainment events. The fraction of mixed-layer water present at depth quantifies plume transport below the layer.			
14. SUBJECT TERMS Ocean Mixed Layer Ocean Convection Polar Oceans Deep Entrainment			15. NUMBER OF PAGES 140
			16. PRICE CODE
17. SECURITY CLASSIFICATION OF REPORT Unclassified	18. SECURITY CLASSIFICATION OF THIS PAGE Unclassified	19. SECURITY CLASSIFICATION OF ABSTRACT Unclassified	20. LIMITATION OF ABSTRACT UL

Approved for public release; distribution is unlimited.

**ENTRAINMENT, DETRAINMENT, AND LARGE-SCALE
HORIZONTAL GRADIENTS IN OCEANIC DEEP CONVECTION**

Rebecca E. Stone
Lieutenant Commander, United States Navy
B.S., San Diego State University, 1985
M.S., Naval Postgraduate School, 1997

Submitted in partial fulfillment
of the requirements for the degree of

DOCTOR OF PHILOSOPHY IN PHYSICAL OCEANOGRAPHY

from the

NAVAL POSTGRADUATE SCHOOL
June 1999

Author:

Rebecca E. Stone

Rebecca E. Stone



Approved by:

Roland W. Garwood, Jr.
Professor of Oceanography
Dissertation Supervisor

Peter S. Guest

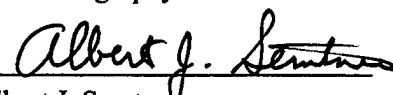
Peter S. Guest
Research Associate Professor
of Meteorology



Ramsey R. Harcourt
Research Assistant Professor
of Oceanography

Wieslaw Maslowski

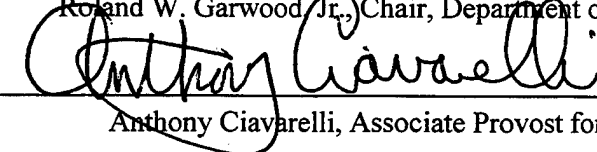
Wieslaw Maslowski
Assistant Professor
of Oceanography



Albert J. Semtner
Professor of Oceanography

Approved by:

Roland W. Garwood Jr., Chair, Department of Oceanography



Anthony Ciavarelli, Associate Provost for Instruction

ABSTRACT

The theory of oceanic convection and entrainment has been developed mainly in horizontally homogeneous regimes, yet large-scale spatial variability is known to control the sites and intensity of deep convection. Wintertime Greenland Sea conditions were selected to simulate convection and quantify the interplay between local forcing and large-scale gradients. Here circulation and preconditioning produce horizontal gradients in the stratification; some of the resulting stratification is conducive to the formation of thermobaric convective instabilities.

A large eddy simulation (LES) model modified to include large-scale horizontal density gradients was used to study the effects of the gradients on turbulence. Horizontal turbulent kinetic energy (TKE) and scalar variances increased compared to simulations with no large-scale gradient. The additional horizontal TKE is created at scales larger than the convective plume scale. A mean horizontal circulation develops in response to the large-scale overturning. The balance between convection and overturning increases stratification in the lower region of the mixed layer, and plumes may undergo slantwise convection.

One-dimensional bulk TKE model results were compared to a large eddy simulation of wintertime Greenland Sea convection. One-dimensional and LES results were similar in the distribution of TKE components and in the ratio A_R of entrainment buoyancy flux to surface buoyancy flux for the winter period modeled. The value of A_R was large because of strong shear production, 0.42 for the one-dimensional model, and 0.36 for the LES. Detraining thermobaric plumes were simulated by LES under various conditions of rotation and stratification. A critical depth h_{cr} and critical velocity w_{cr} hypothesized by Garwood et al. (1994) were shown to be predictors for onset of detrainment. The skewness of vertical velocity in a horizontal slice just below the mixed layer is shown to be an indicator for detrainment events. The fraction of mixed-layer water present at depth quantifies plume transport below the layer.

TABLE OF CONTENTS

I. INTRODUCTION	1
A. STATEMENT OF PROBLEM	1
B. THE GREENLAND SEA REGION	2
C. OVERVIEW	4
D. LITERATURE REVIEW	5
1. Mixed Layer Theory and Modeling	5
2. Deep Convection	6
3. Various Modeling Approaches	8
4. Large Eddy Simulation	12
II. THEORETICAL OVERVIEW	15
A. FUNDAMENTAL EQUATIONS	16
1. General Equations	16
2. Turbulent Energy Cascade	17
3. One-Dimensional Equations	17
4. Scalings	20
B. EQUATIONS FOR SCALAR VARIANCE	21
C. THERMOBARIC INSTABILITIES	23
1. Thermobaric Plumes	24
2. Thermobaric Interleaving	25

III. MODELS FOR LARGE EDDY AND ONE-DIMENSIONAL SIMULATION	27
A. ONE-DIMENSIONAL FORMULATION	27
B. LARGE EDDY FORMULATION	29
C. IMPOSITION OF HORIZONTAL GRADIENTS IN THE LES	32
IV. GREENLAND SEA ENTRAINING MIXED LAYER CASE STUDY	33
A. DESCRIPTION OF PARAMETERS	33
B. COMPARISON	34
V. SIMULATIONS OF THERMOBARIC PARCEL INSTABILITIES	39
A. DESCRIPTION OF PARAMETERS	39
B. PLUME FORMATION	41
C. PLUME ENTRAINMENT AND EFFECT ON INTERIOR FLUID	44
VI. SIMULATIONS IN THE PRESENCE OF A LARGE-SCALE GRADIENT	47
A. DESCRIPTION OF PARAMETERS	47
B. SIMULATIONS OF ACTIVE CONVECTION	50
1. Bulk Turbulent Kinetic Energy and Variance	50
2. Currents	52
3. Horizontal Fluxes	53
4. Stability	56

C. POST-CONVECTION SPIN-DOWN	57
VII. CONCLUSIONS AND RECOMMENDATIONS	59
A. CONCLUSIONS	59
B. RECOMMENDATIONS	61
1. One-Dimensional Modeling	61
2. Large-Scale LES	61
3. Restratification	62
LIST OF REFERENCES	63
APPENDIX	69
INITIAL DISTRIBUTION LIST	121

x

LIST OF FIGURES

1	Schematic of the Greenland Sea	69
2	Thermobaric Plume Schematic	70
3	Thermobaric Interleaving Schematic	71
4	Forcing and resulting mixed-layer deepening as predicted by the one-dimensional model and by LES.	72
5	Mixed-layer deepening, temperature, and salinity as predicted by the one-dimensional model and by LES.	73
6	Turbulent kinetic energy (TKE) components as predicted by the one-dimensional model and by LES.	74
7	Contributions to $\overline{u^2}$ as computed by the one-dimensional model and by LES.	75
8	Contributions to $\overline{v^2}$ as computed by the one-dimensional model and by LES.	76
9	Contributions to $\overline{w^2}$ as computed by the one-dimensional model and by LES.	77
10	TKE contributions as computed by the one-dimensional model and by LES.	78
11	TKE contributions as computed by the one-dimensional model and by LES.	79
12	Initial profiles of temperature and salinity for the thermobaric plume experiments.	80
13	Profiles of buoyancy for a mixed-layer parcel if plunged to any depth below the initial interface.	81
14	Initial N^2 profiles for the varied stratification cases.	82
15	Energy-density spectra for vertical velocity at 95m	83
16	Energy-density spectra for vertical velocity at 95m	84
17	A field of detraining thermobaric plumes, rendered using an isosurface of temperature. Width of domain is 2.56km. Plumes are descending about 400m below the interface, which is at a depth of 200m.	85
18	Time series from unstratified experiments.	86

19	Profiles from unstratified experiments.	87
20	Time series from experiments varying the stratification.	88
21	Profiles from experiments varying the stratification.	89
22	Skewness of Vertical Velocity at 285m.	90
23	Plots of LES horizontal mean temperature as a function of depth and time, from unstratified experiments. Top: Rotation and Full Thermobaricity, Center: No Rotation, Bottom: Thermobaricity Off Below the Mixed Layer	91
24	Plots of LES horizontal mean temperature as a function of depth and time, from experiments varying the stratification. Top: Unstratified, Up- per Center: Weak Stratification, Lower Center: Moderate Stratification, Bottom: Strong Stratification.	92
25	Profiles of temperature at the initial time and 10 hours after the onset of detrainment.	93
26	Profiles of the fraction of mixed-layer water present 10 and 20 hours after the onset of detrainment. Solid lines are at 10 hours; dashed lines are at 20 hours.	94
27	Horizontal cross-sections of temperature and salinity	95
28	Horizontal cross-sections of temperature and salinity	95
29	Vertical cross-section of vertical velocity from gsea3.2.	96
30	Vertical cross-section of vertical velocity from gstrat2.	96
31	Conditions used in the horizontal gradient experiments.	97
32	Energy-density spectra for vertical velocity at 190m	98
33	Temperature variance spectra at 190m	99
34	LES Salinity at a depth of 40m from the weak gradient experiment. Box is 2.56km on a side. The color scale is (S-34.85)e-3 psu.	100
35	LES Vertical Velocity at a depth of 40m from the weak gradient experi- ment. Box is 2.56km on a side. The color scale is in m/s.	101
36	LES Temperature at a depth of 40m from the weak gradient experiment. Box is 2.56km on a side. The color scale is in °Ce-3.	102

37	Bulk Mean Turbulent Energy as a function of time.	103
38	Ratio of Vertical to Total TKE.	104
39	Bulk Temperature and Salinity Variances from horizontal means.	105
40	LES Salinity at 20m depth from the strong gradient experiment when the box mode is large. Box is 2.56km on a side. The color scale is in $(S-34.85)e-3$ psu.	106
41	LES nonhydrostatic pressure per unit density and horizontal flow fields at 20m depth from the strong gradient experiment when the box mode is large. Box is 2.56km on a side. The color scale is in $m^2 s^{-2} e-3$. The longest arrows represent horizontal speeds of 9 cm/s.	107
42	LES Vertical Velocity at 20m depth from the strong gradient experiment when the box mode is large. Box is 2.56km on a side. The color scale is in m/s e-3.	108
43	Mean Velocity Profiles.	109
44	Schematic showing enhancement of geostrophic currents.	110
45	Horizontal-mean Velocity at the first grid level.	111
46	Horizontal Flux Profiles.	112
47	Horizontal Flux plots for the Strong Gradient case.	113
48	Profiles of detrended temperature and potential buoyancy. Top left and right are from the experiments with 200 W/m ² . Center left and right are from the experiments with 400 W/m ² . Bottom left and right are from the experiment with the strong gradient and 400 W/m ²	114
49	Stability (N^2) Profiles. Top is from the experiments with 200 W/m ² . Center is from the experiments with 400 W/m ² . Bottom is from the experiment with the strong gradient and 400 W/m ²	115
50	Postconvection Plots of TKE behavior in time.	116

51	Potential buoyancy and horizontal flow 40m below the surface in the weak gradient experiment 48 hours after cooling stops. Box is 2.56km on a side. Color scale is in $m/s^2 e^{-3}$. The longest arrows represent horizontal speeds of 3 cm/s.	117
52	Potential buoyancy and horizontal flow 40m below the surface in the strong gradient experiment 48 hours after cooling stops. Box is 2.56km on a side. Color scale is in $m/s^2 e^{-3}$. The longest arrows represent horizontal speeds of 3.5 cm/s.	118
53	Postconvection Plots of N^2 and M^2 profiles	119

ACKNOWLEDGMENT

The Author would like to acknowledge the support of the Office of Naval Research, Code 322OM, and the National Science Foundation, Office of Polar Programs.

The Author would like to thank Professor R. W. Garwood both for his guidance and also for the freedom to launch off in other directions at times; Dr. R. R. Harcourt for his questions and assistance; and Dr. P. Lherminier for her fresh perspective and encouragement.

I also thank my mother Virginia Stone for her help and extra affection toward my children during the final months of this work. Finally, I am deeply indebted to my husband Joe Callaway; his love and support made it possible for me to persevere to completion.

I. INTRODUCTION

A. STATEMENT OF PROBLEM

All interaction of the atmosphere with the ocean must begin where the two fluids are in contact - that is, in the adjacent, fully turbulent layers of the ocean and atmosphere. The oceanic mixed layer is more buoyant than the water below, so that changes in the atmosphere are to some extent isolated from the deep ocean by the more buoyant layer. Exceptions to this general structure are in the polar ocean regions, where mixing may occur to great depths, or even to the bottom. This coupling of the ocean to the atmosphere through deep mixed layers in polar regions drives the global thermohaline conveyor belt and thus influences the earth's climate system.

One-dimensional models are widely used to predict mixed-layer properties, as well as the depth of mixing. The depth of mixing changes due to entrainment, that is, by mixing into it the nonturbulent fluid from below. Generally, a model's constants are tuned to give correct entrainment for some set of typical mid-latitude situations and will not be as applicable to polar and subpolar scenarios. To extend the range of conditions for which a model is useful, there needs to be comparison to data from a wide range of conditions. Given the scarcity of detailed data sets of turbulence, especially in the near-polar regions, the realistic physics of large eddy simulation (LES) models provides important data for comparison. Energy distribution among the components and the relative importance of energy sources need to be compared between one-dimensional and LES models.

Nonlinearities in the equation of state for seawater add complexity to mixed-layer dynamics at high latitudes. Near freezing temperature, the thermal expansion coefficient is especially sensitive to pressure; this effect, termed thermobaricity, can produce instabilities when a cold fresh mixed layer overlies warmer, more saline water, resulting in detrainment of mixed-layer water into the ocean interior. Detraining plumes have been simulated by Garwood et al. (1994) in a regime with neutral stratification below the mixed layer. It has not yet been shown how nonzero stratification will affect plume formation, plume entrainment, and the interior fluid.

One-dimensional models and, typically, LES simulations of ocean turbulence use an assumption of large-scale horizontal homogeneity. Yet convection, especially the selection of sites for deep convection, is known to be affected by the large-scale ocean conditions. There is a need for basic knowledge of how horizontal inhomogeneities may interact with turbulence. Energy component balance and energy sources for convection may be altered by a horizontal gradient or by vertical current shear, and stability may differ from the stability found in horizontally homogeneous domains.

B. THE GREENLAND SEA REGION

Most of the volume of the world ocean is insulated from the atmosphere by the buoyant upper layer of the ocean, with only a few sites subject to deep mixing. The known sites of deep convection are located in the Weddell Sea, the Mediterranean Sea, the Labrador Sea, and the Greenland Sea. As early as 1906, Nansen observed extremely small differences

in properties of Greenland Sea surface and deep waters, and proposed that deep water formation occurred there. A schematic of the Greenland Sea is shown in Figure 1. In the upper layers, warm, salty water from the Norwegian Atlantic Current is advected in by the West Spitzbergen Current. Some of this flow is recirculated in the Return Atlantic Current, where it joins the cold, fresh East Greenland Current flowing in from the Arctic Ocean. The eastern edge of the East Greenland Current is called the East Greenland Polar Front. The circulation is completed with the cold and fresh Jan Mayen Current. The cyclonic circulation results in a doming of isopycnals in the central Greenland Sea gyre. This brings the weakly stratified interior waters close to the surface (Rudels and Quadfasel, 1991; Schott et al., 1993; Worcester et al., 1993) and is the first step in preconditioning for deep convection.

In early winter, as the marginal ice zone propagates rapidly eastward, brine release and entrainment act to increase the salinity of the surface waters. In combination with strong surface cooling, the buoyancy of the mixed layer is thus eroded. Mixed-layer deepening during this period may extend far enough into the warm Atlantic Intermediate Water so that, when subsequent cooling and stirring occur, warming by entrainment dominates over surface cooling (Visbeck et al., 1995). Any ice present is rapidly melted, and further ice formation is prevented; an ice-free area known as the Nordbukta forms. The Nordbukta is transitory, and is bounded on the west by the East Greenland Polar Front, and on the south and east by a cold icy tongue called the Is Odden. The Nordbukta, situated over the Greenland Sea gyre, is further preconditioned for deep convection. Within the preconditioned region, convection is believed to be localized by local forcing, migrating cyclonic or anticyclonic eddies, or

other unknown mechanisms (Häkkinen, 1987; Häkkinen et al., 1992; Häkkinen, 1995; Killworth, 1979; Killworth, 1983; Lherminier, 1999; Morawitz et al., 1996).

C. OVERVIEW

Chapter I introduces the topic of study and motivation and reviews the literature. Chapter II lays out the fundamental equations and modeling techniques used in this study. Chapter III presents the case study of a wintertime Greenland Sea scenario; one-dimensional model results are compared to an LES simulation of the same period. Chapter IV presents LES numerical experiments in which thermobaric plumes were simulated under various conditions. The detrainment of plumes from the mixed layer and their subsequent mixing with the interior are affected by the differing interior stratifications used in several model scenarios. Chapter V shows results for LES simulations of active convection and turbulent spin-down in the presence of large-scale horizontal density gradients. Behavior of turbulent kinetic energy (TKE) components and scalar variances differs from convection in a horizontally homogeneous regime. Chapter VI summarizes important conclusions and makes recommendations for further study.

D. LITERATURE REVIEW

1. Mixed Layer Theory and Modeling

The importance of ocean mixed-layer physics is expressed by Garwood (1976):

Interest in the ocean mixed layer stems from both theoretical and practical considerations. Thermal energy and mechanical energy received from the atmosphere not only control the local dynamics, but the layer itself modulates the flux of this energy to the deeper water masses. Conversely, flux of heat back to the atmospheric boundary layer has an important influence upon the climate and its fluctuations.

Garwood (1976) and Zilitinkevich et al. (1979) provide background summaries of historical contributions to the field of mixed-layer dynamics. Early modeling frameworks involved only the mean momentum budget, with no inclusion of mechanical energy - either buoyancy or turbulent kinetic energy. Kraus and Turner (1967) first included mechanical stirring in their model, parameterizing shear production of turbulent kinetic energy (TKE) on the wind stress. Niiler (1974) emphasized the importance of using the turbulent kinetic energy equation in modeling the mixed layer, and included entrainment shear production and damping in the TKE budget. Garwood (1977) refined the mechanical energy budgets used so that entrainment depended on the vertical energy component rather than bulk total turbulent energy. In a more detailed three-component TKE equation model, mixed-layer deepening was shown to depend on wind direction, Garwood et al. (1985).

Price et al. (1986) used a simplified one-dimensional bulk gradient Richardson number-based model to study the separate and combined effects of diurnal heating and cooling, wind stress, and entrainment. The model gave realistic profiles of temperature and

velocity, and predicted a trapping depth for the upper ocean's response to the diurnal forcing cycle.

McDougall (1987) coined the term "thermobaricity" in his study of the effects of nonlinearities in the seawater equation of state for isopycnal mixing. Gill (1973) first included thermobaricity in a static model for shelf convection. The dynamic mixed-layer importance of thermobaricity, which is the pressure dependence of the thermal expansion coefficient, which he termed thermobaricity, was explained by Garwood (1991), using a model that individually calculated the three components of turbulent kinetic energy.

Large et al. (1994) have studied the use of a scheme called K Profile Parameterization (KPP) which uses a nonlocal transport term K for the boundary layer, assigns an eddy viscosity K for the ocean interior, and matches the K profile at the boundary layer interface. This approach does allow a representation of entrainment, but the nonlocal transport term is determined only by surface fluxes and does not parameterize the effect of entrainment fluxes.

2. Deep Convection

Early observations in the Mediterranean Sea show that regions of deep water formation are selected by the large-scale stratification, to first order (Gascard, 1973). Later Killworth (1979, 1983) noted that chimneys, or regions of open-ocean deep water formation, are narrower than can be explained by large-scale gyres and cooling regimes; some other preconditioning mechanism must determine the specific area for overturning. Cyclonic eddies produced by baroclinic instability of the mean flow tend to reduce stratification by lifting and cooling a localized area of approximately chimney scale ($\sim 20\text{km}$); such eddies

lifting and cooling a localized area of approximately chimney scale (~20km); such eddies were Killworth's likely suspects for the preconditioning mechanism.

From observations in the Labrador Sea, Clarke and Gascard (1983) found open-ocean deep water formation occurring under approximately the same conditions specified by Killworth. Further observations made in winter 1994-1995, reported in Lilly et al. (1998), showed intermediate-depth winter convection, with 200-1000 m wide plumes reaching 1750m in depth. The depth varied greatly with location, and the water-mass properties were not horizontally homogenized to that depth.

Greenland Sea observations in the winter of 1988-1989 highlight the variable nature of convection in the Greenland Sea. There is seasonal variability, as the area becomes ice-covered and then ice-free again when the Nordbukta opens, and interannual variability, as winter forcing produces mixing to great depth in some years, and only intermediate depths in others (Schott et al., 1993). In 1989, Morawitz et al. (1996) measured a chimney of scale 40 km or less, which penetrated to below 1000m, and speculated that its location was preconditioned by a hole in the underlying Arctic Intermediate Water, resulting from unsteadiness of inflow in the summer of 1988. However, a net salinity gain for the column was observed but unexplained. Observations in the winter of 1993-1994 also showed a feature that could be classified as a chimney, an anticyclonic eddy with horizontal scale ~50 km. Although convection was limited to intermediate depth throughout the basin, this feature was the site for the deepest mixing observed (800m). However, the winter of these

observations was an atypical one, since no Is Odden formed and the surface buoyancy loss was less than the decadal mean (Lherminier, 1998).

Marshall and Schott (1999) provide a recent summary of observations, theory and models of open-ocean deep convection, including discussions of the importance of rotation, thermobaricity, and horizontal inhomogeneity. They note that the interplay of plume scales, mesoscale eddy scales, and large-scale preconditioning is important in all known sites of open-ocean deep convection.

3. Various Modeling Approaches

The importance of deep convection to the climate has motivated many modeling approaches. Ultimately, climate models must be able to realistically convey heat and tracers from the atmosphere to the intermediate and bottom waters of the ocean. An important step in this complex problem is the development of a computationally simple one-dimensional model that can be applied to each vertical column of a GCM grid, and result in realistic vertical profiles and water mass production.

The simplest representation of the polar atmosphere's effect on the heat distribution of the ocean is that buoyancy loss at the surface is compensated by overturning to remove hydrostatic instability through convective adjustment. Sander et al. (1995) compared the results of a nonhydrostatic model to those for pure convective adjustment. He concluded that convective adjustment may be adequate when small-scale dynamics are relatively unimportant, but that the vertical advective transport of tracers is inhibited. In such schemes,

buoyancy loss is conceived as a mechanism for overturning by convective adjustment only, and is not recognized as an important source of mechanical energy for entrainment.

Visbeck et al. (1995) used an ice-coupled model to study the factors necessary for deep water formation in the Greenland Sea. They found that a strictly one-dimensional approach could not account for the differences in deepening between the water columns of the Nordbukta and those of the Is Odden. However, a quasi two-dimensional approach that included an average ice export did accurately reproduce observed ocean response.

Garwood et al. (1994) hypothesized two kinds of thermobaric conditional instabilities: a thermobaric layer instability, in which a layer may become statically unstable if advected downward; and a thermobaric parcel instability, in which parcels overshoot the mixed-layer interface, become thermobarically unstable, are detrained from the mixed layer, and accelerated downward. Detraining plumes were simulated in an LES model, and proposed scalings were given for critical depth and velocity. Garwood and Isakari (1993) developed a scheme for use in ocean general circulation models, in place of the convective adjustment routine, that includes the effects of parcel instabilities, with possible detrainment of fluid from the mixed layer. Paluskieicz and Romea (1997) report on the development of a similar scheme.

Häkkinen (1992) used a large-scale three-dimensional coupled ice-ocean model with 2.5 order turbulence closure (Mellor and Yamada, 1974), without a convective adjustment scheme, to model deep convection in the Greenland Sea. Häkkinen imposed a barotropic mean flow over shelf break topography containing either a canyon or a spur. She found that

in the presence of an ice edge, which induces upwelling, either the canyon or the spur can provide preconditioning and determine a deep convection site.

Several studies focus not on the initiation and location of deep convection, but on its later development and effects once a given region has been subject to deep mixing (Jones and Marshall, 1993; Legg and Marshall, 1993; Send and Marshall, 1995; Jones and Marshall, 1997). These studies hypothesize that the sinking, spreading, and restratification phases of deep convection will be modeled effectively by largely neglecting plume-scale processes, representing them by a vertical mixing time scale, and focusing on the breakup of the mixing site by baroclinic instability.

Stone (1997) used a one-dimensional, three-component model to study mixed-layer deepening in the Greenland Sea as observed during February and March 1994. Comparison of energy contributions from buoyancy flux versus wind forcing showed a surprising dominance of wind energy, and underscored the need for further study of the relative importance of wind and cooling in models of deep mixed regimes.

Akitomo (1999a, 1999b) investigated the effects of thermobaricity on open-ocean deep convection. High-resolution numerical experiments with constant eddy viscosity and eddy diffusivity were initialized with realistic ocean conditions; rapid overturning occurred in the Weddell Sea due to thermobaric instability, and more gradual deepening occurred in the Greenland Sea due to greater stratification.

Yoshikawa et al. (1999) used a large-scale nonhydrostatic model with constant eddy viscosity to study convective processes in the presence of a geostrophic velocity shear. They

found that the convective plumes accelerate the growth of baroclinic instability and enhance vertical motion.

Straneo and Kawase (1999) compared two models of localized convection, one due to localized forcing, and the other due to uniform forcing but localized preconditioning. They found that the localized forcing tends to overemphasize the importance of baroclinic instability during active convection, and increasing the horizontal gradients during the course of convection, whereas convection in the preconditioned scenario decreased the horizontal gradients initially present. Studies using a two-dimensional model (Straneo et al., 1999) show that the interaction between horizontal gradients and active convection results in slantwise convection and can alter mixed-layer deepening from that predicted by one-dimensional considerations. Marshall and Schott (1999) provide a discussion of slantwise convection, and discuss the transition from convection to baroclinic instability for cases with localized forcing.

The focus of this dissertation is a better understanding of the physics involved in deep mixing; there are still gaps in the detailed knowledge of ocean turbulence that may affect large-scale parameterizations. An important limitation to many models being used to study deep convection is the use of hydrostatic physics and/or the use of unrealistic eddy viscosities and eddy diffusivities even when nonhydrostatic terms are resolved. Detailed data sets of geophysical turbulence are needed to test how well viscous models apply to the ocean. Because of the difficulty of obtaining data sets of geophysical turbulence, large eddy simulation is an important tool for improving our understanding of deep turbulent mixing

in the ocean. We turn to large eddy simulation because of its ability to represent turbulence to as fine a scale as desired; the grid spacing is chosen small enough to resolve energy down to scales including a part of the $-5/3$ log-slope inertial energy cascade. Processes on scales smaller than this are parameterized (see Chapter II, Section A).

4. Large Eddy Simulation

Large eddy simulation (LES) is a modeling technique that resolves the energy-containing and flux-supporting eddies at and below the integral scales of motion. Unlike direct numerical simulation (DNS), LES does not resolve the Kolmogoroff microscale, and eddies smaller than the LES resolution are parameterized. Unlike Reynolds average numerical simulation (RANS), the parameterization uses an eddy viscosity that is time and space dependent (Orszag, 1993). Smagorinsky (1963) and Lilly (1967) pioneered the use of such nonlinear eddy viscosities to parameterize the effect of unresolved turbulence. Deardorff (1973) added a dynamic equation for the subgrid energy to determine the nonlinear eddy viscosity. In an atmospheric boundary layer model, he was able to achieve realistic temperature variances, turbulent intensities, and to preserve the sharpness of the inversion base during entrainment. Moeng (1984) created a new LES model for study of the atmospheric planetary boundary layer, following Deardorff. She used spectral methods in the horizontal to take advantage of FFT algorithms and improved closure assumptions in the subgrid parameterization by using a spectral cut-off filter to separate large-eddy and subgrid domains. Further work by Moeng and Wyngaard (1988) refined the subgrid dissipation and

eddy viscosity parameterizations to improve the inertial range spectra. They also demonstrated the relative insensitivity of the model to the subgrid parameterization.

The atmospheric boundary layer LES model of Moeng (1984) was modified to represent the oceanic boundary layer, and was used to simulate escaping thermobaric plumes by Garwood et al. (1994). The work included free convection in a neutral layer, and free convection in a neutral layer with salinity-stratified water below. Some plumes that reached the interface passed through and were termed thermobaric plumes because the increase in the thermal expansion coefficient caused them to change from being positively buoyant at the interface to neutrally and then negatively buoyant as the parcels' momentum carried them below the interface.

The LES model has been further modified to improve the resolved spectra by using horizontally isotropic filtering methods (Harcourt and Garwood, 1994), and to control errors by using an upwind numerical scheme for scalar advection near sharp boundaries (Harcourt, 1999).

II. THEORETICAL OVERVIEW

The ocean mixed layer, characterized both by turbulence and by temperatures and salinities relatively homogenized with depth, resides above the nonturbulent, stably stratified interior of the ocean. A sharp density gradient is usually at the lower boundary of the mixed layer, while its upper boundary is the wavy air-sea interface. For the highly variable fluxes from the atmosphere to have any effect upon the underlying water masses, they must be communicated through this turbulent layer.

Although temperature and salinity are characteristically unstratified within the mixed layer, the amount of inhomogeneity varies greatly. Variances within the mixed layer depend on surface fluxes of temperature and salinity, via cooling, rain, and entrainment of contrasting fluid from below. Lateral mixing in a horizontally inhomogeneous regime also produces variance.

The physical properties of seawater itself add complexity to mixed-layer dynamics. Near freezing temperature, the thermal expansion coefficient is especially sensitive to pressure; this effect, termed thermobaricity, can produce instabilities when a cold fresh mixed layer overlies warmer, more saline water. This type of instability may result in detrainment of mixed-layer water into the stratified water below. Another interesting consequence of thermobaricity is the possibility of fluids of equal density but contrasting temperature and salinity laterally interleaving, with the warm, salty intrusions being preferentially preserved.

A. FUNDAMENTAL EQUATIONS

1. General Equations

The Navier-Stokes equations of motion are the starting point for calculating mixed-layer turbulence:

$$\frac{\partial u_i}{\partial t} = - u_j \frac{\partial u_i}{\partial x_j} - \frac{1}{\rho} \frac{\partial p}{\partial x_i} - 2 \epsilon_{ijk} \Omega_j u_k - \delta_{i3} g + v \frac{\partial^2 u_i}{\partial x_j^2} \quad (2.A.1)$$

The indices $i = 1, 2, 3$ correspond to the Cartesian coordinate directions of east, north, and up; Ω is earth's rotation: $[\Omega_i] = \Omega [0 \cos \phi \sin \phi]$; molecular viscosity is v ; gravitational acceleration is g ; and ϕ is latitude.

The turbulent kinetic energy (TKE) equation is formed from the equations of motion by decomposing the variables into their mean and turbulent parts, $u_i = \bar{u}_i + u'_i$, where the turbulent part is not assumed to be small compared to the mean. Using the Boussinesq approximation and incompressibility, the total TKE equation for the system is

$$\begin{aligned} \frac{\partial \bar{u}_i'^2}{\partial t} &= - \frac{\partial}{\partial x_j} (\bar{u}_j \bar{u}_i'^2) - 2 \bar{u}_i' \bar{u}_j' \frac{\partial \bar{u}_i}{\partial x_j} - \frac{\partial}{\partial x_j} (\bar{u}_i'^2 \bar{u}_j') \\ &\quad + \frac{2}{\rho_0} p' \frac{\partial \bar{u}_i'}{\partial x_i} - \frac{2}{\rho_0} \frac{\partial}{\partial x_i} (\bar{u}_i' p') + v \bar{u}_i' \frac{\partial^2 u_i'}{\partial x_j^2} \\ &\quad - 4 \epsilon_{ijk} \Omega_j \bar{u}_i' \bar{u}_k' - 2 \delta_{i3} \frac{g}{\rho_0} \bar{u}_i' \bar{\rho}' \end{aligned} \quad (2.A.2)$$

The equation for mean flow is formed from equation (2.A.1) by decomposing, averaging, making the Boussinesq approximation, and neglecting viscous effects on the mean flow:

$$\frac{\partial \bar{u}_i}{\partial t} = -\bar{u}_j \frac{\partial \bar{u}_i}{\partial x_j} - \frac{1}{\rho_0} \frac{\partial \bar{p}}{\partial x_i} - \delta_{ij} g \left(\frac{\bar{\rho} - \rho_0}{\rho_0} \right) + 2 \epsilon_{ijk} \Omega_j \bar{u}_i - \frac{\partial \bar{u}_i \bar{u}_j}{\partial x_j} \quad (2.A.3)$$

The equations for scalars potential temperature and salinity are formed from conservation of energy and mass:

$$\frac{\partial \theta}{\partial t} = -\bar{u}_i \frac{\partial \theta}{\partial x_i} + \kappa_T \nabla^2 \theta \quad (2.A.4)$$

$$\frac{\partial S}{\partial t} = -\bar{u}_i \frac{\partial S}{\partial x_i} + \kappa_S \nabla^2 S \quad (2.A.5)$$

where κ_T and κ_S are molecular diffusivities.

2. Turbulent Energy Cascade

It is important in a turbulence-resolving model to be sure that the smallest scales resolved are part of the inertial subrange. In an energy spectrum, if the energy per unit wavenumber E ($\text{m}^3 \text{s}^{-2}$) is a function of only the wave-number k (m^{-1}) and viscous dissipation ϵ ($\text{m}^2 \text{s}^{-3}$), then the energy in the larger scales cascades down to smaller scales following

$$E \propto \epsilon^{2/3} k^{-5/3} \quad (2.A.6)$$

The portion of the spectrum that follows this -5/3 law is referred to as the turbulent inertial subrange, and connects the scales at which the system is being forced to the scales at which dissipation is occurring (Kolmogoroff, 1941).

3. One-Dimensional Equations

A set of one-dimensional equations derived from the more general equations (2.A.1)-(2.A.5) is presented briefly here; full details of its derivation can be found in Stone (1997).

The general equations have been decomposed, averaged, and vertically integrated over a depth h . The hydrostatic and Boussinesq approximations have been made; horizontal homogeneity has been invoked; and viscous effects on the mean flow have been neglected.

The equations for the ageostrophic mean flow are

$$\frac{\partial(h\langle\bar{U}\rangle)}{\partial t} = 2\Omega_3 h\langle\bar{V}\rangle + \frac{\tau_x}{\rho_0} \quad (2.A.7)$$

$$\frac{\partial(h\langle\bar{V}\rangle)}{\partial t} = -2\Omega_3 h\langle\bar{U}\rangle + \frac{\tau_y}{\rho_0} \quad (2.A.8)$$

The geostrophic balance has been subtracted from these horizontal momentum equations. Overbars indicate averaging in time, the angle brackets indicate the vertical average, and the wind stresses are τ_x and τ_y .

The temperature and salinity equations are

$$\frac{\partial\bar{\theta}}{\partial t} = \frac{1}{h} \left(\frac{Q_0}{\rho_0 c_p} - w_e \Delta\bar{\theta} \right) \quad (2.A.9)$$

$$\frac{\partial\bar{s}}{\partial t} = \frac{1}{h} \left(\bar{s} F_{sw} - w_e \Delta\bar{s} \right) \quad (2.A.10)$$

The temperature flux at the surface has been written as

$$\overline{\theta'w'}|_0 = \frac{Q_0}{\rho_0 c_p} \quad (2.A.11)$$

with Q_0 the rate of cooling of the surface, and c_p the specific heat of seawater at constant pressure. The surface salinity flux is

$$\overline{s'w'}|_0 = \bar{s} F_{sw} \quad (2.A.12)$$

with F_{sw} being the net rate of equivalent water fluxed upward at the surface due to precipitation, evaporation, melting, and freezing, and having units meters/second. Fluxes of conserved quantities at the bottom of the mixed layer are calculated, assuming

approximately-linear flux profiles within the layer, as

$$\overline{C'w'}|_{-h} = -w_e \Delta C \quad (2.A.13)$$

where C is the conserved quantity and w_e is the entrainment velocity. Also, $\frac{\partial h}{\partial t} = w_e$ in the absence of upwelling or downwelling.

The turbulent kinetic energy equations are

$$\begin{aligned} \frac{\partial h \langle u'^2 \rangle}{\partial t} &= \frac{2m_3}{u_*} \left(\frac{\tau_x}{\rho_0} \right)^2 + w_e (\Delta \bar{u})^2 + 2\Omega_2 h \frac{\tau_x}{\rho_0} \\ &+ 2m_2 (\langle E \rangle - 3 \langle u'^2 \rangle) \langle E \rangle^{\frac{1}{2}} - \frac{2}{3} m_1 \langle E \rangle^{\frac{3}{2}} \end{aligned} \quad (2.A.14)$$

$$\begin{aligned} \frac{\partial h \langle v'^2 \rangle}{\partial t} &= \frac{2m_3}{u_*} \left(\frac{\tau_y}{\rho_0} \right)^2 + w_e (\Delta \bar{v})^2 \\ &+ 2m_2 (\langle E \rangle - 3 \langle v'^2 \rangle) \langle E \rangle^{\frac{1}{2}} - \frac{2}{3} m_1 \langle E \rangle^{\frac{3}{2}} \end{aligned} \quad (2.A.15)$$

$$\begin{aligned} \frac{\partial h \langle w'^2 \rangle}{\partial t} &= gh \left[\frac{\rho_0}{\rho c_p} (a_0 + \frac{a_1 h}{3}) + \beta \bar{S} Vol \right] \\ &- gh w_e [\Delta \bar{\theta} (a_0 + \frac{a_1 h}{1.5}) - \beta \Delta \bar{S}] - 2\Omega_2 h \frac{\tau_x}{\rho_0} \\ &+ 2m_2 (\langle E \rangle - 3 \langle w'^2 \rangle) \langle E \rangle^{\frac{1}{2}} - \frac{2}{3} m_1 \langle E \rangle^{\frac{3}{2}} \end{aligned} \quad (2.A.16)$$

The thermal expansion coefficient is treated not as constant, but is allowed to vary linearly with depth:

$$\alpha(z) = a_0 - a_1 z \quad (2.A.17)$$

The constants m_1, m_2, m_3 are the dissipation constant, the pressure redistribution constant,

and the shear production constant. The friction velocity is given by $u^* \equiv \frac{1}{\rho_0} \sqrt{\tau_x^2 + \tau_y^2}$, the total turbulent kinetic energy is $\langle E \rangle = (\langle u'^2 \rangle + \langle v'^2 \rangle + \langle w'^2 \rangle)^{1/2}$, and the dissipation is $D = 2m_1 \langle E \rangle^{3/2}$.

4. Scalings

Some useful scalings are presented here for use in later chapters. First, a measure of buoyant production of TKE due to surface fluxes is the free-convection velocity scale w_0^* calculated from surface fluxes in the TKE equation

$$w_0^{*3} = -2g \int_0^h [\alpha(z) \overline{w' \theta'}|_0 - \beta \overline{w' S'}|_0] (1 - \frac{z}{h}) dz = -g \frac{\rho_0}{\rho c_p} h (a_0 + \frac{a_1 h}{3}) + g F_{SW} h \beta \quad (2.A.18)$$

This is the rate at which TKE is produced by hydrostatic adjustment of buoyancy loss. If a_1 is zero, then

$$w_0^{*3} = -B_0 h \quad (2.A.19)$$

When a_1 is nonzero, the velocity scale includes the additional energy produced by downward acceleration of parcels due to thermobaricity. The total buoyant production is given by a velocity scale that includes the effect of buoyant damping

$$w^{*3} = -2 \int_0^h \overline{w' b'} dz \quad (2.A.20)$$

Since w_0^{*3} is known, and w^{*3} can be calculated, the buoyant damping of TKE due to entrainment can be deduced

$$w_E^{*3} = w^{*3} - w_0^{*3} \quad (2.A.21)$$

A natural Rossby number for a layer of depth h in free convection, found by scaling of the momentum equation, is

$$R_o = \frac{w^*}{f h} \quad (2.A.22)$$

The Rossby internal radius of deformation, the distance a parcel must travel before the effect

of rotation becomes significant, is

$$R_d = \frac{\sqrt{g'h}}{f} \quad (2.A.23)$$

and can be applied to a layer homogeneous in potential temperature but with depth-dependent $\alpha(z)$ as

$$R_d = \frac{\sqrt{ga_1\theta H^2}}{f} \quad (2.A.24)$$

B. EQUATIONS FOR SCALAR VARIANCE

Beginning with the temperature equation (2.A.4), and the equation for mean temperature formed by decomposition and averaging equation (2.A.4),

$$\frac{\partial \bar{\theta}}{\partial t} = -\overline{u'_i \frac{\partial \theta'}{\partial x_i}} + \kappa_T \nabla^2 \bar{\theta} \quad (2.B.1)$$

equation (2.B.1) is subtracted from equation (2.A.4) to give an equation for the temperature perturbation.

$$\frac{\partial \theta'}{\partial t} = -\overline{u'_i \frac{\partial \theta}{\partial x_i}} + \overline{u'_i \frac{\partial \theta'}{\partial x_i}} + \kappa_T \nabla^2 \theta' \quad (2.B.2)$$

Multiplying equation (2.B.2) by θ' and averaging gives

$$\frac{\partial}{\partial t} \left(\frac{\overline{\theta'^2}}{2} \right) = -\overline{u'_i \theta' \frac{\partial \bar{\theta}}{\partial x_i}} - \overline{u'_i \theta' \frac{\partial \theta'}{\partial x_i}} - \overline{u'_i \theta' \frac{\partial \theta'}{\partial x_i}} + \kappa_T \overline{\theta' \nabla^2 \theta'} \quad (2.B.3)$$

If we assume that $\overline{\theta'^2}$ is horizontally homogeneous, $\overline{w} = 0$, and neglect curvature effects on diffusion, equation (2.B.3) becomes

$$\begin{aligned} \frac{\partial}{\partial t} \left(\frac{\overline{\theta'^2}}{2} \right) &= -\overline{u' \theta' \frac{\partial \bar{\theta}}{\partial x}} - \overline{w' \theta' \frac{\partial \bar{\theta}}{\partial z}} - \left(\frac{\partial}{\partial x} \overline{u' \frac{\theta'^2}{2}} + \frac{\partial}{\partial y} \overline{v' \frac{\theta'^2}{2}} + \frac{\partial}{\partial z} \overline{w' \frac{\theta'^2}{2}} \right) \\ &\quad - \kappa_T \left(\frac{\partial \theta'}{\partial x} \frac{\partial \theta'}{\partial x} + \frac{\partial \theta'}{\partial y} \frac{\partial \theta'}{\partial y} + \frac{\partial \theta'}{\partial z} \frac{\partial \theta'}{\partial z} \right) \end{aligned} \quad (2.B.4)$$

The first two terms on the right-hand-side are horizontal and vertical gradient production, the first term in parentheses is turbulent transport, and the last is dissipation.

For application to the one-dimensional model of this paper, we require horizontal homogeneity of $\bar{\theta}$ and integrate Equation 2.B.4 over a mixed layer of depth h . Net turbulent transport vanishes since there is no flux of variance through the surface or the interface. Since the vertical derivative of $\bar{\theta}$ is non-zero only near the surface and near the interface, the integral of the gradient production term can be written as two separate terms.

The contribution from the interface is

$$\frac{w_e(\Delta\bar{\theta})^2}{2} \quad (2.B.5)$$

where w_e is the entrainment velocity and $\Delta\bar{\theta}$ is the potential temperature jump across the interface. The contribution from the surface is

$$-\overline{w'\theta'}|_0 \delta\bar{\theta} = \left(\frac{Q_0}{\rho c_p}\right) \left(\frac{m_3}{u^*} \frac{Q_0}{\rho c_p}\right) = \frac{m_3}{u^*} \left(\frac{Q_0}{\rho c_p}\right)^2 \quad (2.B.6)$$

where $\frac{Q_0}{\rho c_p}$ is the surface heat flux, m_3 is a constant of proportionality, and the near-surface gradient $\delta\bar{\theta}$ depends on both the surface heat flux and a velocity scale u^* in forced convection, or w^* in free convection. The dissipation rate of temperature variance must depend on the amount of variance present and on some dissipation time scale T_χ , such that

$$\chi \equiv \kappa_T \overline{\frac{\partial\theta'}{\partial x_i} \frac{\partial\theta'}{\partial x_i}} \sim m_1 \frac{\langle \overline{\theta'^2} \rangle}{T_x} \quad (2.B.7)$$

where m_1 is a constant of proportionality, and angle brackets mean the vertical average has

been taken. Variance must dissipate on the same time scale on which energy dissipates, that

is, $\tau_x = \frac{h}{\sqrt{E}}$, so

$$\int_{-h}^0 \chi dz = m_1 \langle \bar{\theta}^{1/2} \rangle \langle E \rangle^{1/2} \quad (2.B.8)$$

The one-dimensional temperature variance budget then has the form

$$\frac{\partial}{\partial t} \left[h \frac{\langle \bar{\theta}^{1/2} \rangle}{2} \right] = \frac{m_3 (\frac{Q_0}{\rho c_p})^2}{u^*} + \frac{w_e (\Delta \bar{\theta})^2}{2} - m_1 \langle \bar{\theta}^{1/2} \rangle \langle E \rangle^{1/2} \quad (2.B.9)$$

In steady state, solving for temperature variance gives the result

$$\langle \bar{\theta}^{1/2} \rangle = \frac{\frac{m_3}{u^*} \left(\frac{Q_0}{\rho c_p} \right)^2 + \frac{w_e (\Delta \bar{\theta})^2}{2}}{m_1 \langle E \rangle^{1/2}} \quad (2.B.10)$$

The first term in the numerator is the surface production of temperature variance, and the second is entrainment production.

Similarly, if the salinity flux at the surface is negligible,

$$\langle \bar{s}^{1/2} \rangle = \frac{w_e (\Delta \bar{s})^2}{2 m_1 \langle E \rangle^{1/2}} \quad (2.B.11)$$

C. THERMOBARIC INSTABILITIES

The thermal expansion coefficient of seawater,

$$\alpha = -\frac{1}{\rho_0} \frac{\partial \rho}{\partial \theta} \quad (2.C.1)$$

varies with both temperature and pressure. The variation with pressure can give rise to instabilities that are termed thermobaric instabilities. The vertical dependence of α can be

expressed as

$$\alpha(z) = \alpha_0 - \frac{\partial \alpha}{\partial z} z \quad (2.C.2)$$

The thermobaric depth scale H_α indicates the depth at which the thermal expansion coefficient is twice its surface value

$$H_\alpha = \frac{-\alpha_0}{\frac{\partial \alpha}{\partial z}} \quad (2.C.3)$$

Taking $\frac{\partial \alpha}{\partial z}$ as a constant, $\alpha(z)$ can be written

$$\alpha(z) = \alpha_0 \left(1 - \frac{z}{H_\alpha}\right) \quad (2.C.4)$$

1. Thermobaric Plumes

A parcel that is displaced downward, such as in Figure (2), will experience a change in buoyancy

$$\Delta b = -g \alpha_1 \theta_1 \Delta z \quad (2.C.5)$$

where $\alpha_1 = \frac{\partial \alpha}{\partial z}$. If this buoyancy difference is greater than the environment's buoyancy difference for the two levels, the parcel will continue its vertical motion away from its original position. Mixed layer parcels near the interface experience displacements downward during active convection, and if the displacement Δz is greater than a critical depth

$$h_{cr} = \left(\frac{\beta \Delta S}{\alpha_0 \Delta \theta} - 1\right) H_\alpha \quad (2.C.6)$$

thermobaric plumes may escape from the mixed layer (Garwood et al., 1994). The critical depth would be reached by a parcel with initial downward speed

$$w_{cr} = (h_{cr} - h) \left(\frac{\alpha_0 g \Delta \theta}{H_\alpha}\right)^{1/2} \quad (2.C.7)$$

2. Thermobaric Interleaving

It is possible for a parcel to be laterally displaced in such a way that it forms a temperature and salinity contrast with the parcels immediately above and below it, but leaves the profile of potential density unperturbed, such as in Figure (3). The density-compensated intrusion has temperature and salinity characteristics such that

$$\alpha_{\eta=0} \delta\theta = \beta \delta S \quad (2.C.8)$$

and the background buoyancy gradient is

$$\frac{d\bar{b}}{dz} = g\alpha \frac{d\bar{\theta}}{dz} - g\beta \frac{d\bar{S}}{dz} = N^2 \quad (\geq 0) \quad (2.C.9)$$

We define the vertical coordinate $\eta = 0$ at the level of the intrusion, and

$$\alpha = \alpha_{\eta=0} \left(1 - \frac{\eta}{H_\alpha}\right) \quad (2.C.10)$$

If the intrusion is displaced vertically, it experiences a vertical acceleration due to buoyant forces

$$\frac{d^2\eta}{dt^2} = b' = \alpha g \theta' - \beta g S' \quad (2.C.11)$$

where

$$\theta' = \delta\theta - \eta \frac{d\bar{\theta}}{dz} \quad (2.C.12)$$

and

$$S' = \delta S - \eta \frac{d\bar{S}}{dz} \quad (2.C.13)$$

Substituting equations (2.C.8), (2.C.9), (2.C.10), (2.C.12), and (2.C.13) into (2.C.11), we get

the wave equation

$$\frac{d^2\eta}{dt^2} + \left(\frac{g \alpha_{\eta=0} \theta'}{H_\alpha} + N^2\right) \eta = 0 \quad (2.C.14)$$

with stable, oscillating solutions for warm intrusions ($\theta' > 0$). For cold intrusions ($\theta' < 0$) there is a critical background stratification

$$N_c^2 = - \frac{g \alpha_{\eta=0} \theta'}{H_\alpha} \quad (2.C.15)$$

below which the intrusion will be unstable to vertical perturbations. Thus we expect that in regions where thermobaricity is strong, profiles may reveal some preference for warm salty intrusions, and that cold fresh intrusions will be less commonly observed.

The time scale for oscillations (or growth) is

$$\tau = \frac{2 \pi}{\sqrt{\left(\frac{g \alpha_{\eta=0} \theta'}{H_\alpha} + N^2 \right)}} \quad (2.C.16)$$

The background stratification is normally the dominant term, yielding time scales of 10-100 minutes.

III. MODELS FOR LARGE EDDY AND ONE-DIMENSIONAL SIMULATION

A. ONE-DIMENSIONAL FORMULATION

The one-dimensional equations of Chapter II are closed by scaling the TKE budget at the bottom of the mixed layer. Shear production and dissipation are small compared to the transport of turbulence from above and the buoyant damping due to entrainment, so that the balance is mainly among storage, turbulent transport, and buoyant damping. See Stone (1997) for details. The entrainment velocity w_e is

$$w_e = \frac{m_4 \sqrt{\langle \bar{E} \rangle} \sqrt{\langle w'^2 \rangle}}{\langle \bar{E} \rangle + gh(\alpha \Delta \bar{\theta} - \beta \Delta \bar{S})} \quad (3.A.1)$$

The dimensionless constant m_4 is introduced to compensate for the fact that one-dimensional equations cannot account for the vertical distribution of energy within the layer, and turbulence is typically more concentrated in the upper mixed layer than near the entrainment zone.

Table 1 summarizes the one-dimensional model equations used in this study. The system of equations was cast as a MATLAB function, and the function was then called using the MATLAB utility ODE45, a Runge-Kutta ordinary differential equation solver that has automatic step-size control.

$$\frac{\partial \bar{\theta}}{\partial t} = \frac{1}{h} \left(\frac{\varrho_0}{\rho_0 c_p} - w_e \Delta \bar{\theta} \right)$$

$$\frac{\partial \bar{S}}{\partial t} = \frac{1}{h} \left(\bar{S} F_{sw} - w_e \Delta \bar{S} \right)$$

$$\frac{\partial(h<\bar{U}>)}{\partial t} = 2\Omega_3 h <\bar{V}> + \frac{\tau_x}{\rho_0}$$

$$\frac{\partial(h<\bar{V}>)}{\partial t} = -2\Omega_3 h <\bar{U}> + \frac{\tau_y}{\rho_0}$$

$$w_e = \frac{m_4 <\bar{E}> \sqrt{<\bar{w}^2>}}{<\bar{E}> + gh(\alpha \Delta \bar{\theta} - \beta \Delta \bar{S})}$$

$$\frac{\partial h <\bar{u}^2>}{\partial t} = \frac{2m_3}{u_*} \left(\frac{\tau_x}{\rho_0} \right)^2 + w_e (\Delta \bar{u})^2 + 2\Omega_2 h \frac{\tau_x}{\rho_0} + 2m_2 (<\bar{E}> - 3<\bar{u}^2>) <\bar{E}>^{\frac{1}{2}} - \frac{2}{3} m_1 <\bar{E}>^{\frac{3}{2}}$$

$$\frac{\partial h <\bar{v}^2>}{\partial t} = \frac{2m_3}{u_*} \left(\frac{\tau_y}{\rho_0} \right)^2 + w_e (\Delta \bar{v})^2 + 2m_2 (<\bar{E}> - 3<\bar{v}^2>) <\bar{E}>^{\frac{1}{2}} - \frac{2}{3} m_1 <\bar{E}>^{\frac{3}{2}}$$

$$\begin{aligned} \frac{\partial h <\bar{w}^2>}{\partial t} = & gh \left[\frac{\varrho_0}{\rho c_p} \left(a_0 + \frac{a_1 h}{3} \right) + \beta \bar{S} Vol \right] + 2m_2 (<\bar{E}> - 3<\bar{w}^2>) <\bar{E}>^{\frac{1}{2}} - \frac{2}{3} m_1 <\bar{E}>^{\frac{3}{2}} \\ & - gh w_e \left[\Delta \bar{\theta} \left(a_0 + \frac{a_1 h}{1.5} \right) - \beta \Delta \bar{S} \right] - 2\Omega_2 h \frac{\tau_x}{\rho_0} \end{aligned}$$

Table 1. One-Dimensional Model Equations.

B. LARGE EDDY FORMULATION

The LES model calculates three-dimensional, nonhydrostatic, geophysical turbulence using the vorticity forms of equation (2.A.1) with the Boussinesq approximation, the continuity equation, plus the heat and salinity budgets expanded from equation (2.A.4):

$$\frac{\partial u}{\partial t} = v \zeta_z - w \zeta_y - \frac{\partial P^*}{\partial x} + 2 \Omega_z v - 2 \Omega_y w - \frac{\partial \tau_{xx}}{\partial x} - \frac{\partial \tau_{xy}}{\partial y} - \frac{\partial \tau_{xz}}{\partial z} \quad (3.B.1)$$

$$\frac{\partial v}{\partial t} = w \zeta_x - u \zeta_z - \frac{\partial P^*}{\partial y} - 2 \Omega_z u - \frac{\partial \tau_{xy}}{\partial x} - \frac{\partial \tau_{yy}}{\partial y} - \frac{\partial \tau_{yz}}{\partial z} \quad (3.B.2)$$

$$\frac{\partial w}{\partial t} = u \zeta_y - v \zeta_x - \frac{\partial P^*}{\partial z} + g [\alpha(\theta - \theta_0) - \beta(S - S_0)] + 2 \Omega_y u - \frac{\partial \tau_{xz}}{\partial x} - \frac{\partial \tau_{yz}}{\partial y} - \frac{\partial \tau_{zz}}{\partial z} \quad (3.B.3)$$

$$\frac{\partial u}{\partial x} + \frac{\partial v}{\partial y} + \frac{\partial w}{\partial z} = 0 \quad (3.B.4)$$

$$\frac{\partial \theta}{\partial t} = -u \frac{\partial \theta}{\partial x} - v \frac{\partial \theta}{\partial y} - w \frac{\partial \theta}{\partial z} + \frac{\partial}{\partial x} (K_\theta \frac{\partial \theta}{\partial x}) + \frac{\partial}{\partial y} (K_\theta \frac{\partial \theta}{\partial y}) + \frac{\partial}{\partial z} (K_\theta \frac{\partial \theta}{\partial z}) \quad (3.B.5)$$

$$\frac{\partial S}{\partial t} = -u \frac{\partial S}{\partial x} - v \frac{\partial S}{\partial y} - w \frac{\partial S}{\partial z} + \frac{\partial}{\partial x} (K_s \frac{\partial S}{\partial x}) + \frac{\partial}{\partial y} (K_s \frac{\partial S}{\partial y}) + \frac{\partial}{\partial z} (K_s \frac{\partial S}{\partial z}) \quad (3.B.6)$$

Here u , v , and w are the easterly, northerly, and vertical velocity components, ζ is vorticity, $2 \Omega_z$ is the vertical Coriolis parameter, $2 \Omega_y$ is the horizontal Coriolis parameter, and α is the thermal expansion coefficient. Shear stresses are expressed as τ_{ij} such that

$$\tau_{ij} = -K_M \left(\frac{\partial u_i}{\partial x_j} + \frac{\partial u_j}{\partial x_i} \right) \quad (3.B.7)$$

The dynamic pressure P^* includes terms for resolved and unresolved energy e

$$P^* = \frac{p}{\rho_0} + \frac{2}{3}e + \frac{u_k u_k}{2} \quad (3.B.8)$$

In the model code, α is calculated using a_0 and a_1 as in equation (2.A.17). Specified values for wind and surface buoyancy flux enter the equations through the surface boundary conditions by specifying values for τ_{13} in the momentum equations and values for $K_\theta \frac{\partial \theta}{\partial z}$ and $K_s \frac{\partial S}{\partial z}$ in the scalar equations. The bottom boundary condition is slip with respect to the mean flow and no-slip with respect to perturbations from the mean. Boundary conditions are doubly periodic in x and y . The system of equations is solved using second order centered finite differencing in the vertical, the spectral method of Fox and Orszag (1973) in the horizontal, and time advancement with an Adams-Bashforth scheme.

Turbulence is assumed to be isotropic at the grid scale and smaller. Subgrid scale fluxes of momentum, salinity, and temperature are calculated using second order turbulence closure, giving eddy mixing coefficients K_M , K_S , and K_θ , respectively, that are time- and space-dependent (Smagorinsky, 1963). The coefficients depend on the length scale λ of the unresolved turbulence, the grid scale δ and the velocity scale given by the unresolved turbulent kinetic energy e :

$$K_M = K_\theta = K_S = c_K \lambda \sqrt{e} \quad (3.B.9)$$

The subgrid turbulence length scale in neutral and unstable conditions is the resolution scale δ , related to the grid spacing Δx , Δy , and Δz by:

$$\lambda = \delta = (c_\delta \Delta x \Delta y \Delta z)^{1/3} \quad (3.B.10)$$

The equation for unresolved TKE includes terms for advection, shear production, buoyancy flux, turbulent transport, and dissipation (Deardorff, 1973):

$$\frac{\partial e}{\partial t} = - u_i \frac{\partial e}{\partial x_i} - \tau_{ij} \frac{\partial u_i}{\partial x_j} + g K_\theta (\alpha \frac{\partial \theta}{\partial z} - \beta \frac{\partial S}{\partial z}) + \frac{\partial}{\partial x_i} (2 K_M \frac{\partial e}{\partial x_i}) - \epsilon \quad (3.B.11)$$

where

$$\tau_{ij} = - K_M \left(\frac{\partial u_i}{\partial x_j} + \frac{\partial u_j}{\partial x_i} \right) \quad (3.B.12)$$

Subgrid dissipation ϵ is modeled as:

$$\epsilon = c_\epsilon \frac{e^{3/2}}{\lambda} \quad (3.B.13)$$

When stratification is stable, the length scale of the unresolved turbulence may be smaller than the resolution scale δ , so

$$\lambda = \min(\delta, \lambda_{stab}) \quad (3.B.14)$$

where

$$\lambda_{stab} = c_{stab} \frac{\sqrt{e}}{N} \quad (3.B.15)$$

and N is the buoyancy frequency. The dissipation constant is also reduced in stable conditions, using:

$$c_\epsilon = c_{\epsilon 1} + c_{\epsilon 2} \frac{\lambda}{\delta} \quad (3.B.16)$$

Choice of model constants $c_K = 0.128$, $c_\delta = 1.14$, $c_{stab} = 0.76$, $c_\epsilon = 2.29$, $c_{\epsilon 1} = 0.19$, and $c_{\epsilon 2} = 2.1$ follows Harcourt (1999). Additional details concerning the basic numerical method are provided by Moeng (1984), Garwood et al. (1994), and Harcourt (1999).

C. IMPOSITION OF HORIZONTAL GRADIENTS IN THE LES

Since it was desirable for the LES model to retain doubly periodic boundary conditions, zonal gradients were imposed in the LES domain not by changing temperature or salinity across the box explicitly, but by adding a gradient term to the x derivative after it is calculated in the spectral domain and passed back to the spatial domain. The zonal advection terms of equations (3.B.5) and (3.B.6) are calculated

$$\frac{\partial \theta}{\partial x} = \dots(\text{as previously calculated})\dots + tgrad \quad (3.C.1)$$

$$\frac{\partial S}{\partial x} = \dots(\text{as previously calculated})\dots + sgrad \quad (3.C.2)$$

The pressure gradient term for u momentum, equation (3.B.1), has an additional term that is depth dependent

$$\frac{\partial p}{\partial x} = \dots(\text{as previously calculated})\dots + pgrad(iz) \quad (3.C.3)$$

The depth dependent pressure gradient is calculated starting at the bottom level in the LES domain and integrating upward to produce the correct thermal wind shear

$$pgrad(nnz) = -\alpha tgrad \frac{dz}{2} + \beta sgrad \frac{dz}{2} \quad (3.C.4)$$

$$pgrad(iz) = pgrad(iz + 1) - \alpha tgrad dz + \beta sgrad dz \quad (3.C.5)$$

where α and β are computed level by level.

IV. GREENLAND SEA ENTRAINING MIXED LAYER CASE STUDY

Previous work recommended the comparison of the one-dimensional model and LES for Greenland Sea entrainment (Stone, 1997). Balance among energy components and the dominance of wind or cooling are particularly at issue, and the one-dimensional model constants have been adjusted to better emulate LES-predicted balances.

A. DESCRIPTION OF PARAMETERS

Both the LES model and the one-dimensional model were initialized with temperature and salinity data from a sounding taken by the R/V Valdivia near 74.5°N, 2.5°W on February 16th, 1994. There was a 200-m deep mixed layer of cold fresh water over relatively warm and saline water. Another sounding was taken on March 19th, 31 days later; the mixed layer had deepened to 600 m. The profiles used as the initial conditions were subjected to a convective adjustment scheme to avoid initial instabilities below the 200-m layer. Comparison of heat and salinity content of the water column between the two soundings showed an average loss of 130 W/m² and no net salinity flux. Wind and heat flux data from the European Center for Medium Range Weather Forecasts (ECMWF) were used to force both models, reduced by a factor of 0.56 so that the average heat loss over the period matched that observed in the water column. Applicability of this one-dimensional assumption was discussed in Stone (1997). Figure 4 shows the wind speed and net heat fluxes for the period simulated, as well as the predicted mixed-layer depths. Values for a_0

and a_1 were 3.6e-5 and 2.8e-8, respectively.

Values for the dissipation, pressure redistribution, shear production, and entrainment constants used in the one-dimensional model are shown in Table 2.

m_1	m_2	m_3	m_4
1.0	3.0	1.9	0.3

Table 2. Values of One-Dimensional Model Constants

The LES simulation was done on a grid having 50 vertical levels, 96x96 horizontal grid points, 20m horizontal grid spacing and 19m vertical grid spacing. The grid spacing for horizontal and vertical grids differs so that the resulting resolution is isotropic. The strong wind forcing led to high surface velocities and required a short time step of 30 seconds.

B. COMPARISON

The comparison of results from one-dimensional and LES models focuses on the relative balance of energy components and the relative importance of TKE budget terms. Figure 6 shows TKE components from each model. The total TKE is similar, and although both models show that TKE is anisotropic, the energy is distributed differently among components for the two models. The one-dimensional model has most energy in the v component during the peaks because most of the strong wind forcing was from southerly

winds. The LES energy components tend to distribute wind shear production more evenly between u and v because it resolves shear and turning between each vertical grid level.

Figures 7 and 8 show u and v TKE budget terms; there are significant differences in the sources of turbulent energy. The one-dimensional model equations include the three TKE component equations, so the terms of the TKE budget plotted in Figures 7 and 8 are explicit within the one-dimensional model. The LES TKE production terms plotted are calculated from the mean covariances $\overline{u'w'}$ and $\overline{v'w'}$ and the mean shears $\frac{\partial \bar{u}}{\partial z}$ and $\frac{\partial \bar{v}}{\partial z}$ for shear production. In general, the one-dimensional model is sensitive to wind direction through the shear production term while the LES allows shear to spiral as it is transmitted downward, so that shear production from v wind is put into both u and v turbulent energy. The pressure redistribution term of the one-dimensional model is the term that moves energy produced by v wind shear into u and w components, but the resulting balance is not the same as that in the LES.

Figure 9 allows comparison of buoyant production and buoyant damping. Buoyant production due to surface forcing for both models is computed as w_0^* ³ using Equation 2.A.19. Buoyant damping for the one-dimensional model is calculated using the term in Equation 2.A.16 that contains w_e . To calculate LES total buoyancy flux w^* ³, either the mean covariances $\overline{w'\theta'}$ and $\overline{w'S'}$, or the net mean changes in θ and S profiles over many timesteps can be used. In this case the change in mean profile method was chosen. Buoyant damping for the LES is then computed as total buoyancy flux minus buoyant production due to surface flux, as shown in Equation 2.A.21.

The ratio of entrainment buoyancy flux to surface buoyancy flux used by Stull (1988)

$$A_R = \frac{-\overline{b'w'}|_{-h}}{\overline{b'w'}|_0} \quad (4.B.1)$$

is applied here to the ocean with thermobaricity in a more general form,

$$A'_R = \frac{\overline{w_E^*}^3}{\overline{w_0^*}^3} \quad (4.B.2)$$

Note that $A'_R = A_R$ only for an idealized bulk mixed layer in the absence of thermobaricity.

The ratios are averaged over the entire period and over the two periods with the strongest cooling and are shown in Table 3. These values are large compared to standard values for free convection (Stull, 1988) due both to the strong wind stress and to thermobaricity (Harcourt, 1999).

	Entire Period (days 47.7-83.8)	Days 53.0-57.5	Days 74.0-78.0
1-D	.42	.35	.44
LES	.36	.40	.31

Table 3. Comparison of ratios of entrainment damping to buoyant production.

The one-dimensional model plot indicates that during the strongest forcing event, occurring on about Julian day 76, vertical TKE is getting about as much energy from wind shear via pressure redistribution as from cooling.

Figure 10 shows the total TKE budget terms for each model. Shear production is not as dominant in the LES as in the one-dimensional model, but is still 2-3 times as large as buoyant production. These balances are among *bulk* quantities, however; shear production

in the one-dimensional model is immediately available for entrainment, while in the LES much of the energy produced by shear is produced in the upper levels and dissipated locally.

Figure 11 is similar to Figure 10 except the buoyant production and damping terms are summed to show the net effect.

V. SIMULATIONS OF THERMOBARIC PARCEL INSTABILITIES

The thermobaric plumes described in section 2.C.1 were simulated using the LES model for mixed-layer and interior stratification conditions designed to be similar to wintertime Greenland Sea stratification conditions. Parcels first detrained from the mixed layer in agreement with the predictions for critical depth h_{cr} and critical velocity w_{cr} hypothesized by Garwood (1994) in Equations 2.C.6 and 2.C.7. The escaping plumes exhibit a characteristic mushroom-cap shape, and affect water properties at depth.

A. DESCRIPTION OF PARAMETERS

The simulations of parcel instabilities began with a 180m-deep mixed layer over a layer of neutral or stably stratified fluid. Uniform cooling of 200 W/m² and 5 m/s northward wind was applied at the surface. At the onset of cooling, the sharp interface was perturbed with inertial waves excited by convective plumes, and entrainment began. All the simulations used a grid spacing of 10m, 128x128 horizontal grid points, and 80 vertical levels, except the case with the strongest stratification, which had the lowest 30 levels removed to save computing time.

Two groups of experiments were conducted; in the first group, rotation and thermobaricity were varied. Table 4 shows experiment designations and parameters. The case titled Rotation and Full Thermobaricity included Ω_y and Ω_z and calculated depth-dependent α throughout. The case titled No Rotation had $\Omega_y = \Omega_z = 0$. The case titled

Thermobaricity Off Below the Mixed Layer included rotation terms, but calculated α as depth-dependent down to 220m, then kept the 220m value for the fluid below. In this way, turbulence within the mixed layer retained the effect of thermobaricity, but parcels at the interface were not accelerated downward if they reached depths below 220m. Initial mixed-layer temperature and salinity properties were -1.13 °C and 34.834 psu; lower layer properties were -0.43 °C and 34.900 psu. Values for α_0 and α_1 were 6.5e-5 and 2.75e-8, respectively, giving an initial buoyancy drop at the base of the mixed layer of 3.4142e-6 m/s².

Rotation and Full Thermobaricity	No Rotation	Thermobaricity Off Below the Mixed Layer
gsea3	gsea4	gsea5

Table 4. First group of thermobaric plume simulations, all with unstratified lower layer.

Unstratified $N^2 = 0$	Weak Stratification $N^2 = 8.5e-8$	Moderate Stratification $N^2 = 1.7e-7$	Strong Stratification $N^2 = 3.9e-7$
gsea3.2	gstrat2	gstrat4	gstrat

Table 5. Second group of thermobaric plume simulations, with varying stratification below mixed layer.

In the second group of experiments, stratification below the mixed layer was varied. Table 5 shows experiment designations and parameters. In each case, the mixed-layer

temperature, salinity, and the buoyancy jump at the base of the mixed layer were initialized identically. Figure 12 shows the initial temperature and salinity profiles; Figure 13 shows the stratification in the various experiments. Figure 14 shows the relative buoyancy a mixed-layer parcel would have if plunged to any depth below the initial interface. The zero intercept of each relative buoyancy profile is the depth below which a mixed-layer parcel would become hydrostatically unstable. Values for a_0 and a_1 were 3.69e-5 and 2.65e-8, respectively, and the initial buoyancy jump varied only slightly from that in the first group of experiments, at 3.4289e-6 m/s². Representative vertical velocity spectra are shown in Figures 15 and 16.

B. PLUME FORMATION

Detrainment of parcels occurred in all the unstratified cases and in weak and moderate stratification. Detection of escaping plumes was accomplished using graphical animation. Figure 17 shows a typical field of branching and mushroom-cap-shaped detraining plumes.

Figure 18, top frame, contains a plot of mixed-layer depth for the unstratified experiments. Mixed-layer depth was determined by the maximum gradient of the horizontally-averaged temperature, spline interpolated between grid levels. The critical depth h_{cr} of Equation 2.C.6 is also plotted. Since the interface is vigorously deformed and oscillating, the bottom of the mixed-layer should be considered the median position of a sharp but moving interface, rather than as the location of strongest gradient within a diffuse

region. The mixed layer is deepening and becoming more saline through entrainment and is cooling due to the surface heat loss. The simulation without rotation entrains slightly faster, without the stabilizing effect of rotation. Critical depth is reduced because the ratio $\frac{\beta \Delta S}{\alpha_0 \Delta \theta}$ is decreasing. The buoyancy jump across the interface, which was initially salinity-dominated, is becoming less so as it weakens. After detrainment begins, the mixed layer shallows as a result of the mass lost from the mixed layer by detrainment. The standard case was run to catastrophic detrainment, that is, until escaping fluid volume had completely depleted the upper layer.

The vertical velocities plotted in Figure 18 are the rms values for the bulk horizontally-averaged w variance. The vertical velocity variance is in steady state, but the critical velocity w_{cr} of Equation 2.C.7 is decreasing. Plume formation occurs for both of the thermobaric cases when w_{cr} drops to within about twice the rms fluctuation of w .

The bottom frame in Figure 18 shows the buoyant production averaged over the domain *below* the mixed layer, which is normally zero without plume detrainment. Buoyant production is calculated from the covariance of vertical velocity perturbations with temperature and salinity perturbations, plus subgrid contributions. The experiment with rotation off has plumes escaping earliest, since vertical motions are not constrained. Of the two predictors for the onset of escaping plumes, h_{cr} and w_{cr} , the critical depth exhibits more clearly the difference in timing or the start of detrainment between the experiments with and without rotation; each begins buoyant production below when the mean position of the mixed-layer interface is about 50m above the critical depth.

Figure 19 shows 4-hour-averaged profiles of buoyant production before and during detrainment, except for the case with thermobaricity off, which had no detrainment, but is plotted for comparison. Buoyant production within the mixed layer, which normally has a nearly-linear profile, is affected by the buoyant flux profile below.

Figure 20, top frame, shows a plot of mixed-layer depth and h_{cr} for the set of stratified experiments. For these experiments, the mixed layer also deepens and becomes more saline through entrainment and cools due to surface cooling. Critical depth shallows as the buoyancy jump across the interface weakens. The moderate stratification case was continued until catastrophic detrainment occurred.

The center frame in Figure 20 depicts the rms values for the bulk horizontally-averaged w variance and the critical velocities. The vertical velocity variance is near steady state, but w_{cr} is again decreasing as h , h_{cr} , and $\Delta\theta$ all change. Plume detrainment does occur when w_{cr} is less than twice the rms fluctuation of w , but buoyant production below the mixed layer, shown in the bottom frame of Figure 20, is not as clear an indicator for escaping plumes. This is because there is strong buoyant damping occurring as the plumes entrain water from their new surrounding stratified environment.

Figure 21 shows profiles of buoyant production before and during detrainment. Buoyant production within the mixed layer is relatively unaffected by the process below. Comparing Figures 19 and 21, buoyant production again is seen to be a less clear indicator of detrainment in the stratified cases than it is in neutral stratification. Figure 22 plots the skewness of vertical velocity

$$SK_w = \frac{\overline{w}^{1/3}}{(\overline{w}^{1/2})^{3/2}} \quad (5.B.1)$$

The magnitude of this parameter is small for wave motion ($SK_w \ll 1$). Increases in magnitude of SK_w indicate that large deviations from the mean are concentrated on one side of the mean; the distribution is skewed. In the LES-produced data, skewness at a given level changes suddenly with the passage of plumes through that level. A depth of 285m was chosen for evaluation because it was not affected by the mixed-layer interface, and because there was no significant delay between plume detrainment and the arrival of plumes at that depth. A skewness of -0.7 was chosen somewhat arbitrarily for use in the following section as a consistent indicator for the onset of detrainment.

C. PLUME ENTRAINMENT AND EFFECT ON INTERIOR FLUID

The effect of detraining plumes on the interior of the ocean can be seen in Figure 23 for the unstratified set of experiments. With thermobaricity included at all depths, there is more effect on temperature in the lower levels than the mid-levels. For the experiments where stratification is varied, the effect is not illustrated well by the color plots of temperature (Figure 24). Profiles of temperature before and during detrainment are similarly difficult to compare (Figure 25). Since there is no salinity flux, the fraction of mixed-layer water present at any level can be calculated using the initial salinity at that level, the current salinity at that level, and the current mixed-layer salinity:

$$A_{mix}(z) = \frac{S(z)_{current} - S(z)_{initial}}{S_{ML} - S(z)_{initial}} \quad (5.C.1)$$

Figure 26 plots the fraction of mixed-layer water present at each level, 10 and 20 hours after detrainment begins. This quantity better distinguishes the differences among the scenarios.

In the environments with nonzero stratification, the effect of plume entrainment did not produce a region at depth that contained a greater fraction of mixed-layer water than the fraction present at mid-depths below the mixed layer.

The parameterization of Paluskieicz and Romea (1997) assumes a top-hat distribution for a plume's temperature and salinity across a horizontal slice, and determines the plume entrainment rate as proportional to a calculated vertical velocity profile, which typically has a maximum below the mixed layer. While no direct comparison of detrainment's effect on interior water properties as calculated by the parameterization and by LES is made here, a check against LES data for these two assumptions made by the scheme can be done. Figures 27-30 show temperature and salinity cross-sections for detraining plumes. Temperature and salinity are relatively constant across the plumes in all simulations, with gradients concentrated at a sharp edge, but more so for the unstratified cases. Figures 31 and 32 shows vertical cross-sections of w that capture several detraining plumes. Plume velocities can have local maxima below the mixed layer in both the stratified and unstratified cases.

VI. SIMULATIONS IN THE PRESENCE OF A LARGE-SCALE GRADIENT

Active convection and postconvective spin-down were modeled with horizontal gradients imposed in the east-west direction using the scheme of Section 3.C. The horizontal gradients result in mean north-south currents generated by thermal wind shear. Mean profiles of u show a slow overturning trend. Scalar variances of temperature and salinity and TKE increase as a result of the large-scale gradient. Furthermore, horizontal fluxes and stability within the mixed layer are affected by the interaction of overturning and turbulence.

A. DESCRIPTION OF PARAMETERS

The numerical experiments in this chapter used a domain 2.56km x 2.56km x 400m deep, 128x128 horizontal grid points, and 20 vertical levels, with the exception of the case with no surface-forced convection. This case was 1.28km x 1.28km x 400m deep and had 41 vertical levels. Aside from the mean horizontal gradients, the LES domain was initially horizontally and vertically homogeneous, so that when convection began, the entire domain became fully turbulent, with no entraining layer. Uniform cooling of either 200 or 400 W/m² was applied, with negligible surface wind stress. Table 6 shows the parameters that were varied in the different experiments. The latitude of 75°N determined Ω_z , but Ω_y was held to a zero value. The suffix “tbo” on an experiment designation indicates that the effect of thermobaricity was turned off by setting a_t to zero.

Numerical Experiments - LES and Horizontal Stratification					
	Surface Forcing Regime				
Horizontal Gradient Regime		Quiescence	Active Convection $Q_0=200 \text{ W/m}^2$	Active Convection $Q_0=400 \text{ W/m}^2$	Post Convection $Q_0=0$
	No Gradient		gr5200	gr5, gr5tbo	gr5co
	Weak Gradient	gradbcomp	gr9	gr4, gr4tbo	gb7, gb7tbo
	Strong Gradient			gr6	gr6co

Table 6. Names and titles of horizontal gradient experiments.

The two nonzero horizontal gradient regimes are described by the parameters in Table 7, and Figure 31 plots the buoyancy gradients and resultant geostrophic velocities. In both regimes, temperature and salinity decrease eastward, and their gradients are partially

	$\bar{\theta}$ °C	\bar{S} psu	a_0 °C ⁻¹	a_1 °C ⁻¹ m ⁻¹	tgrad °C m ⁻¹	sgrad psu m ⁻¹	max bgrad s ⁻²	R _d m
Weak Gradient	-1.5	34.85	3.15e-5	2.92e-8	-6.25e-6	-6.05e-7	2.7e-9	1835
Strong Gradient	-1.0	34.85	3.84e-5	2.86e-8	-1.33e-4	-6.70e-6	-1.2e-8	1573

Table 7. Values used in the horizontal gradient experiments.

compensating in buoyancy. In the weak gradient experiment, salinity (*sgrad*) dominates the buoyancy gradient (*bgrad*), and a northward geostrophic flow results. The buoyancy gradient changes with depth due to the pressure dependence of the thermal expansion coefficient, in conjunction with the temperature gradient (*tgrad*).

$$bgrad = -g(a_0 + a_1 z)tgrad + g\beta sgrad \quad (6.A.1)$$

The small buoyancy gradient, with temperature and salinity gradients almost completely compensating, was originally chosen in hopes of generating the intrusions discussed in Section 2.C.2. No cases, either with or without cooling, exhibited interleaving.

The vertical density gradient is used to compute the Rossby radius of deformation

$$R_d = \frac{\sqrt{g a_1 \theta H^2}}{f} \quad (6.A.2)$$

The sizes of the deformation radii are close to the box dimension of 2.56km; features the scale of the Rossby radius cannot be well resolved in these numerical experiments.

In the strong gradient experiment, properties and gradients were chosen to be similar to a rim current region at the edge of the Greenland Sea gyre near 75°N and 6°E in 1989, reported by Budéus et al. (1993), with the thermal expansion coefficient chosen to correspond to a temperature of 1.0 °C. Temperature and salinity decrease eastward, but the effect of temperature dominates the buoyancy gradient. This buoyancy gradient is an order of magnitude larger than in the weak gradient experiment. Thermal wind shear produces surface currents on the order of 1-2 cm/s for both cases, but in opposite directions. Steady state was reached in the cases with no gradient and weak gradient, but a growing horizontal box mode was present in the strong gradient case; spectra are shown in Figures 32 and 33.

B. SIMULATIONS OF ACTIVE CONVECTION

A particularly striking feature of the simulations with large-scale gradients is the appearance of features such as those shown in the salinity field of Figures 34. The horizontal variability is organized at scales larger than the scale of convective plumes, shown in Figure 35. Temperature variability, shown in Figure 36, is similarly organized into larger scales, but the appearance of convergence zones of sinking surface-cooled water partially masks the organization into larger scales in the near-surface temperature field.

1. Bulk Turbulent Kinetic Energy and Variance

Figure 37 shows the bulk mean TKE for experiments with varying gradients. The total amount of TKE increases with the strength of the horizontal gradient. Most of the increase is in the horizontal TKE components; Figure 38 shows the ratio of vertical to total TKE; the ratio decreases with the strength of the horizontal gradient. Figure 39 shows bulk temperature and salinity variances. For the different experiments, the amount of variance increases with the strength of the horizontal gradient. The increase in TKE increases subgrid diffusivity, but the continual advection of more disparate parcels into the domain results in a net increase in the variance. Experiments with weak and no large-scale gradients showed little change in time, but in the strong gradient experiment, the variance increase was evident even before the TKE showed significant increase. The strong gradient experiment did not achieve steady state even after a period of more than 16 days. The peaks in TKE and variance were associated with the growth and destruction of a feature at the scale of the LES domain, shown in Figures 40-42. The nature of this feature was quite complicated: clear

signatures were found in the temperature, salinity, buoyancy, and pressure fields, but not in the vertical velocity field; and the horizontal velocity field shows detailed structure.

Table 8 lists some common quantities used in scaling turbulence and compares the results in these experiments with the scalings suggested by Harcourt (1999). These scalings suggest that $\frac{\overline{w'^2}_{bulk}}{w^*^2} \approx 0.375 R_0^{.2495}$ and $\frac{\overline{w'^2}_{peak}}{w^*^2} \approx 0.558 R_0^{.295}$. Compared with these scalings, the values found here are consistently lower by about ten percent, showing disagreement in the scaling coefficient. Although w^* increases slightly with larger horizontal gradients, the scaling relation between $\overline{w'^2}$ and w^*^2 appears to be less sensitive to the horizontal gradients. The scaling relations were determined by Harcourt (1999) using simulations without the thermobaric effect; the results in Table 8 show slightly better agreement in the cases with thermobaricity off.

	w^* (cm/s)	Natural R_o	$w'^2/TKE^{1/2}$	w'^2_{bulk}/w^*^2	$.375 R_o^{.2495}$	w'^2_{peak}/w^*^2	$.558 R_o^{.295}$
gr5	2.34	.44	.42	.29	.31	.39	.44
gr5tbo	2.34	.44	.42	.28	.31	.40	.44
gr5200	1.86	.35	.42	.27	.29	.36	.41
gr4	2.34	.44	.40	.29	.31	.39	.44
gr4tbo	2.38	.44	.40	.29	.31	.41	.44
gr9	1.86	.35	.40	.27	.29	.37	.41
gr6	2.48	.46	.33	.29	.31	.41	.45

Table 8. Turbulent scaling quantities for the experiments with horizontal gradients.

2. Currents

Figure 43 shows the time-mean profiles of the horizontal velocity components. The north-south velocity is similar to the geostrophic balance required for the buoyancy gradient that was prescribed. Velocities vanish at the bottom of the domain because the frame of reference for the LES moves with the mean flow at the bottom grid level. The mean east-west current profile for the weak gradient cases shows westward flow near the surface, which would bring in fresher and cooler water above, and eastward flow near the bottom, which would advect in warmer and more saline water below. Since the horizontal buoyancy gradient is salinity-dominated, the surface inflow is relatively buoyant, and the lower-level inflow is more dense. This tendency for more buoyant water to be advected in near the surface and less buoyant water to be advected in near the bottom is a feature of overturning. Overturning currents move the system toward a more stable stratification state. In the strong gradient case, the mean east-west current profile shows eastward flow in most of the layer, which would advect in warmer and more saline water above, and westward flow near the bottom, which would advect in cooler and fresher water below. The buoyancy gradient is temperature-dominated, so again the system is overturning. Comparison of the overturning currents for the cases with weak gradient and varying amounts of cooling shows that convection increases the speed with which the system advects fluid in the effort to reach a state with lower potential energy. In a rotating reference frame such as this, mean u currents affect mean v , so resolved values for v are different from the geostrophic values. Figure 44 shows schematically this effect at the first grid level.

Figure 45 shows time plots of the mean velocity at the first grid level. Pure inertial oscillation for the latitude 75°N has a period of 12.5 hours, and the case with no convection exhibits this period of oscillation. The cases with cooling show that convection does have an effect on the horizontally-averaged inertial currents. The period is modulated: the weaker cooling case shows oscillations with a period of 11 hours; the strong cooling cases show oscillations with periods of 10-11 hours. Also, the coherence of the oscillation in the horizontal mean flow at the surface varies in time, first being disrupted, but then reestablishing a coherent oscillation as ageostrophic motions continue to perturb the steady-state balance. These effects were not investigated in detail, but the time scales of the turbulent eddies were close to the inertial period, so that interaction between convective and inertial motions seems likely. Convective time scales $\frac{H}{w_{rms}}$ were calculated as 11.6 hours for the weak gradient - 200 W/m² case, 9.0 hours for the weak gradient - 400 W/m² case, and 8.3 hours for the strong gradient - 400 W/m² case.

3. Horizontal Fluxes

Mean currents in a horizontally nonhomogeneous regime advect salinity and temperature. Because mean currents are really the result of time-averaging a turbulent flow, the advection by the mean flow can be resolved as turbulent fluxes in the LES. Figure 46 shows the mean profiles of horizontal fluxes for the weak and no gradient cases. Considering fluxes in the direction of the geostrophic mean flow first, $\overline{v'\theta'}$ and $\overline{v's'}$, there is net movement of cold temperatures northward in the weak gradient cases, as the mean northward current carries away newly cooled water. Net movement of more saline water

northward is intensified near the bottom because the overturning continually moves more saline water into the lower region.

There are also turbulent fluxes caused by the overturning. Salinity flux $\overline{u' s'}$ is bow-shaped as westward current near the surface brings fresher water in with $\overline{u' \theta'} > 0$, and eastward current near the bottom brings in more saline water, again with $\overline{u' \theta'} > 0$. However, $\overline{u' \theta'}$ is mostly negative for the case with weak gradients and 400 W/m^2 cooling. This means there is net westward transport of warm temperatures despite the overturning current's tendency to move cooler water west in the upper part of the column. In the experiment with weak gradients and 200 W/m^2 cooling, the turbulent flux $\overline{u' \theta'}$ is close to zero over most of the column, where again a positive value would be expected. The reasons for this unexpected result are unclear, but could be due in part to the fact that the turbulent part of velocity, u' , is computed by subtracting the mean for each level, not the mean over the entire domain, or due in part to the effective shifting of the domain as the mean flow at the lowest level is subtracted. In any case, the effect of this flux in the variance budget of Section 2.B turns out to be relatively small. Using Equations 2.B.4 and 2.B.10, the steady-state one-dimensional bulk variance budget predicts that the temperature variance is

$$\begin{aligned} \langle \overline{\theta'^2} \rangle &= \frac{-2 \int_0^h \overline{w' \theta'} \frac{\partial \overline{\theta}}{\partial z} dz - 2 \int_0^h \overline{u' \theta'} \frac{\partial \overline{\theta}}{\partial x} dz}{m_1 \langle E \rangle^{1/2}} \\ &= 2 \frac{m_3}{w * m_1 \langle E \rangle^{1/2}} \left(\frac{Q_0}{\rho c_p} \right)^2 - 2 \frac{tgrad}{m_1 \langle E \rangle^{1/2}} \int_0^h \overline{u' \theta'} dz \end{aligned} \quad (6.B.1)$$

The first term on the right-hand-side is vertical gradient production, and the second is

horizontal gradient production. Similarly, the steady-state salinity variance should scale as

$$\overline{s'^2} = \frac{-2 \int_0^h \overline{u' s'} \frac{\partial \bar{s}}{\partial x} dz - 2 \int_0^h \overline{w' s'} \frac{\partial \bar{s}}{\partial z} dz}{m_1 \langle E \rangle^{1/2}} = -2 \frac{sgrad}{m_1 \langle E \rangle^{1/2}} \int_0^h \overline{u' s'} dz \quad (6.B.2)$$

Since there is no surface salinity flux, the only contribution using one-dimensional assumptions is horizontal gradient production. LES turbulent fluxes $\overline{u' s'}$ and $\overline{u' \theta'}$ were used with these equations to calculate the values in Table 9.

	Temperature Variance θ'^2	Vertical Gradient Production θ'^2	Horizontal Gradient Production θ'^2	Salinity Variance s'^2	Horizontal Gradient Production s'^2
gr5	4.87e-5	3.01e-6	0	1.10e-10	0
gr5200	1.99e-5	1.23e-6	0	1.76e-10	0
gr4	5.01e-5	2.93e-6	-1.75e-8	3.83e-9	3.68e-10
gr9	2.08e-5	1.19e-6	6.29e-9	4.50e-9	3.59e-10
gr6	1.29e-3	2.34e-6	5.39e-5	3.16e-6	1.32e-7

Table 9. Variance budget contributions.

If the relationship between temperature variance and its surface production in the no gradient cases is used to estimate $\frac{m_3}{m_1}$, a value of 16.2 is found. This value gives good agreement between surface production and total variance for the weak gradient cases, but not for the strong gradient, which is not in steady state. Since horizontal gradients are the only source of salinity variance, it is reasonable to estimate a constant of proportionality between

total salinity variance and its horizontal gradient production as well; the value is 10.4 for the 400 W/m² case and 12.5 for the 200 W/m² case. If a similar constant relates temperature variance to its gradient production, then the weak gradient case has variance production dominated by surface cooling, and advection accounts for a few percent of the variance.

Fluxes for the strong gradient case are shown in Figure 47. Bulk fluxes in time show that the system is not in steady state. The salinity flux profiles have the same shapes as the salinity flux profiles in the weak gradient case, but are more than an order of magnitude larger. Eastward flow through the upper 300m brings in more saline water, and westward flow below brings in fresher water, both giving positive flux values. Mean geostrophic current is southward everywhere, with no y gradient, but the continual salinization over most of the column, with freshening near the bottom, results in net transport of salt south. The shapes of the temperature flux profiles resemble the salinity flux profiles rather than the weak gradient case's temperature profiles. This is because the temperature gradient is strong enough to dominate over cooling in determining the profiles of horizontal flux.

4. Stability

Figure 48 shows profiles of detrended temperature and buoyancy. The shapes of the temperature and buoyancy profiles remain relatively unchanged by the gradient. The strong gradient case shows that profiles of temperature and buoyancy are not in steady state, as overturning continues to change the shape of the profiles. Figure 49 shows profiles of a more sensitive parameter, the buoyancy frequency N squared. All the simulations, with or without horizontal gradients, show an unstable profile over the upper 250m due to surface cooling and a stable region near the bottom. Steady-state N^2 profiles in the simulations with

gradients should be interpreted to mean that the tendency for turbulence to mix to the typical shape without gradients and the tendency for overturning to stratify the system are in balance. The weak gradient cases have reached this balance, but in the strong gradient case the overturning is stronger, and the stratification continues to increase in time. The cases with 400 W/m² cooling are more stable near the bottom than are the cases with 200 W/m² cooling. Stronger cooling means parcels become colder while at the surface before sinking. On average, there is a greater difference between mid-layer parcels and parcels that have sunk to the bottom with strong cooling than parcels more weakly cooled at the surface, resulting in greater average stratification near the bottom.

C. POST-CONVECTION SPIN-DOWN

When cooling at the surface is stopped, TKE drops rapidly to an almost constant value (Figure 50). Turbulent vertical energy becomes less than ten percent of the total energy, and vertical mixing no longer opposes the tendency for overturning. Figure 51 shows the potential buoyancy field and horizontal flow at 40m depth 48 hours after cooling has stopped in the experiment with the weak gradient. Figure 52 is the same except it is for the strong gradient. The scale of the rotating features is larger in the stronger gradient, and may be related to baroclinic instability. M^2 is defined analogously to N^2 as

$$M^2 = \frac{\partial b}{\partial x} \quad (6.B.3)$$

and the slope of a buoyancy surface is

$$s_b = \frac{-M^2}{N^2} \quad (6.B.4)$$

Figure 53 depicts values for M^2 and N^2 at the end of convection. However, it is unclear whether s_b can be a useful parameter to describe the tendency for baroclinic instability when convection stops in these cases; the instability analyses that use the slope of a buoyancy surface to predict growth of perturbations assume N^2 positive (Haine and Marshall, 1998).

VII. CONCLUSIONS AND RECOMMENDATIONS

A. CONCLUSIONS

One-dimensional modeling of the TKE budget for the Greenland Sea entraining mixed layer studied here agrees well with large eddy simulation when universal model constants for dissipation, shear production, and pressure redistribution are tuned for universal geographically-independent application. The generalized TKE bulk closure gives a similar distribution of TKE components to those found in LES as well as a similar ratio of entrainment buoyancy flux to surface buoyancy flux for the period modeled. The ratios are found to be 0.42 for the one-dimensional model, and 0.36 for the LES; they are unexpectedly large because of strong shear production and the impact of thermobaricity.

Convective plumes are able to be detrained from the mixed layer even with stratified fluid below. A critical depth h_{cr} and critical velocity w_{cr} hypothesized by Garwood et al. (1994) are useful indicators of the timing of the onset of detrainment. The skewness of vertical velocity in a horizontal slice just below the mixed layer is a better parameter than is buoyancy flux below the mixed layer for detection of detrainment events. The assumptions about plume temperature and salinity distributions and plume vertical velocity used in the parameterization of Paluskieicz and Romea (1997) are justified based on the LES simulations. Effects of detrainment between LES and this parameterization were not compared. The effect of detrainment on the fluid between the mixed-layer interface and the depth of neutral buoyancy for the detrained parcel differs greatly between cases with zero and

nonzero stratification below the mixed layer. Using the fraction of mixed-layer water present to indicate the amount of plume entrainment, plumes in the stratified cases entrain much more.

Convection with large-scale horizontal gradients, which brings together parcels originally from disparate environments, produces greater temperature and salinity variance than does convection with no large-scale gradients. Convection with horizontal gradients also increases TKE, mainly in the horizontal components. The additional horizontal TKE is present at scales larger than the convective plume scale, and the scale for the horizontal energy increases with the strength of the gradient. Thus the turbulence is less isotropic, but the increased anisotropy is found in the larger scales. Since the amount of vertical TKE is relatively unaffected by the presence of the horizontal gradient, one-dimensional TKE and entrainment models can safely neglect large-scale horizontal gradients when the modeled region is understood to be moving with the flow, and the water column is not subject to significant shear.

Mean horizontal velocities show that large-scale overturning occurs simultaneously with convection. The balance between the two processes results in greater stratification within the mixed layer than in a mixed layer with no horizontal gradients, at least in cases with relatively large vertical buoyancy gradients. The trajectory of a parcel embedded in a convective plume during large-scale overturning could be a slanted trajectory similar to that envisioned in recent literature that discusses slantwise convection. Analysis of the sources of scalar variance in regions with weak horizontal gradients and no entrainment shows that the variance production is dominated by surface processes.

In the spin-down of TKE when surface forcing is stopped, TKE falls to a steady value; horizontal gradients affect the amount of TKE that remains.

B. RECOMMENDATIONS

1. One-Dimensional Modeling

The one-dimensional model of the Greenland Sea entraining mixed layer was able to produce realistic balance among TKE components and among the TKE budget terms. However, inclusion of the tendency for wind stirring to more effectively deepen shallow mixed layers than deeper ones would be an important advance in one-dimensional mixed-layer modeling. Also, the inclusion of prescribed horizontal gradients in the one-dimensional model would give improved variance predictions.

2. Large-Scale LES

The problem of large-scale and convective-scale interaction will eventually require a departure from the doubly-periodic boundary conditions of the LES model used in this work, especially if spatially-varying rates of entrainment are to be allowed.

Further simulations of convection with large-scale gradients that include drifters would be useful to test how well LES fields fit the descriptions of slantwise convection found in recent literature.

Future work should also focus on the horizontal scales produced, what conditions allow baroclinic instabilities to exist simultaneously with convection, and how potential

energy is converted into horizontal turbulence when baroclinic instability processes are not evident.

3. Restratiification

Study of the spin-down of TKE after surface cooling stops and its dependence on horizontal gradients could improve understanding of the restratiification process.

Simulations of conditions in which thermobaric interleaving is expected to occur would test the hypotheses that warm intrusions are preferentially preserved, and have potential to explain historical and current observations.

LIST OF REFERENCES

Akitomo, K., 1999a. Open-ocean deep convection due to thermobaricity, Part 1. Scaling argument. *J. Geophys. Res.*, 104, 5225-5234.

Akitomo, K., 1999b. Open-ocean deep convection due to thermobaricity, Part 2. Numerical experiments. *J. Geophys. Res.*, 104, 5235-5249.

Brown, R. A., 1970. A secondary flow model for the planetary boundary layer. *J. Atmos. Sci.*, 27, 742-757.

Budéus, G., A.-A. Maul, G. Krause, 1993. Variability in the Greenland Sea as revealed by a repeated high spatial resolution conductivity-temperature-depth survey. *J. Geophys. Res.*, 98, 9985-10,000.

Clarke, R. A., and Gascard, J.-C., 1983. The formation of labrador sea deep water, Part I: Large-Scale Processes, *J. Phys. Oceanogr.*, 13, 1764-1778.

Deardorff, J. W., 1973. The use of subgrid transport equations in a three-dimensional model of atmospheric turbulence, *J. Fluids Engineering*, 429-438.

Fox, D. G., and S. A. Orszag, 1973. Pseudospectral approximation to two-dimensional turbulence, *J. Comput. Phys.*, 11, 612-619.

Garwood, R. W., Jr., 1976. A general model of the ocean mixed layer. *NOAA Tech. Rpt. ERL 384-PMEL 27*.

Garwood, R. W., Jr., 1977. An oceanic mixed layer model capable of simulating cyclic states. *J. Phys. Oceanogr.*, 7, 455-468.

Garwood, R. W., Jr., 1991. Enhancements to deep turbulent entrainment, In *Deep Convection and Deep Water Formation in the Oceans*, Ed. by P. C. Chu and J.-C. Gascard, 197-213, Elsevier Science.

Garwood, R. W., Jr., S. M. Isakari, 1993. Entropy-conserving deep convection in the Weddell Sea. *Proceedings*, Fourth Int'l Conference on Southern Hemisphere Meteorology and Oceanography.

Garwood, R. W., Jr., P. Muller, and P. C. Gallacher, 1985. Wind direction and equilibrium mixed layer depth: General theory. *J. Phys. Oceanogr.*, 15, 1325-1331.

Garwood, R. W., Jr., S. M. Isakari, and P. C. Gallacher, 1994. Thermobaric convection, in *The Polar Oceans and Their Role in Shaping the Global Environment*, O. Johannessen, R. Meunch and J. Overland, Eds., Geophysical Monograph 85, 199-209.

Gascard J.-C., 1973. Vertical motions in a region of deep water formation, *Deep-Sea Research*, 20, 1011-1027.

Gill, A. E., 1973. Circulation and bottom water formation in the Weddell Sea. *Deep-Sea Res.*, 20, 111-140.

Haine, T. W. N., and J. Marshall, 1998. Gravitational, symmetric, and baroclinic instability of the ocean mixed layer. *J. Phys. Oceanogr.*, 28, 634-658.

Häkkinen, S., Upwelling at the Ice Edge: A Mechanism for Deep Water Formation?, *J. Geophys. Res.*, 92, 5031-5034, 1987.

Häkkinen, S., Simulated Interannual Variability of the Greenland Sea Deep Water Formation and Its Connection to Surface Forcing, *J. Geophys. Res.*, 100, 4761-4770, 1995.

Häkkinen, S., G. L. Mellor and L. H. Kantha, Modeling deep convection in the Greenland Sea. *J. Geophys. Res.*, 97, 5389-5408, 1992.

Harcourt, R. R., 1999. Numerical simulation of deep convection and the response of drifters in the Labrador Sea. Dissertation, Univ. Of Ca., Santa Cruz, Dept. Of Physics.

Harcourt, R. R., and R. W. Garwood, Jr., Large eddy simulation of open ocean deep convective plumes. *Trans. Am. Geophys. Union*, 75, 364-365, 1994.

Jones, H., and J. Marshall, 1993. Convection with rotation in a neutral ocean: a study of open-ocean deep convection. *J. Phys. Oceanogr.*, 23, 1009-1039.

Jones, H., and J. Marshall, 1997. Restratification after deep convection. *J. Phys. Oceanogr.*, 27, 2276-2287.

Killworth, P. D., 1979. On "chimney" formations in the deep ocean. *J. Phys. Oceanogr.*, 9, 531-554.

Killworth, P. D., 1983. Deep convection in the world ocean, *Rev. Geophys. and Space Phys.*, Vol. 21, No. 1, 1-26.

Kolmogoroff, A. N., 1941. The local structure of turbulence in incompressible viscous fluid for very large Reynolds numbers. *Akad. Nauk USSR*, 30, 301.

Kraus, E. B., and J. S. Turner, 1967. A one-dimensional model of the seasonal thermocline, part II. *Tellus*, 19, 98-105.

Large, W. G., J. C. McWilliams, and S. C. Doney, 1994. Oceanic vertical mixing: A review and a model with a nonlocal boundary layer parameterization. *Rev. Geophys.*, 32, 363-403.

Legg, S., and J. Marshall, 1993. A heton model of the spreading phase of open-ocean deep convection. *J. Phys. Oceanogr.*, 23, 1040-1056.

Lherminier, P., 1998. Convection profonde en mer du groenland: etude experimental des phases du preconditionnement et de melange. Ph. D. Thesis, Universite Pierre et Marie Curie.

Lherminier, P., J.-C. Gascard, and D. Quadfasel, 1999. The Greenland Sea in Winter 1993 and 1994: pre-conditioning for deep convection. *Deep Sea Res. II*, in press.

Lilly, D. K., 1967. The representation of small-scale turbulence in numerical simulation experiments, In *Proceedings of IBM Scientific Symposium on Environmental Sciences*, IBM Form No. 320-1951, pp.195-210.

Lilly, J. M., P. B. Rhines, M. Visbeck, R. Davis, J. R. N. Lazier, F. Schott, and D. Farmer, 1998. Observing deep convection in the Labrador Sea during winter 1994-1995. Unpublished manuscript.

Marshall, J. C., and F. Schott, 1998. Open-Ocean Convection: Observations, Theory, and Models, submitted.

Marshall, J., C. Hill, L. Perelman, and A. Adcroft, 1997. Hydrostatic, quasi-hydrostatic, and nonhydrostatic ocean modeling. *J. Geophys. Res.*, 102, 5733-5752.

Mellor, G. L., and T. Yamada, A hierarchy of turbulence closure models for planetary boundary layers, *J. Atmos. Sci.*, 31, 1791-1806, 1974.

McDougall, T. J., 1987. Thermobaricity, cabbeling, and water-mass conversion. *J. Geophys. Res.*, 92, 5448-5464.

Moeng, C.-H., 1984. A large-eddy simulation model for the study of boundary-layer turbulence. *J. Atmos. Sci.*, 41, 2052-2062.

Moeng, C.-H., and Wyngaard, J. C., 1988. Spectral analysis of large-eddy simulations of the convective boundary layer. *J. Atmos. Sci.*, 45, 3573-3587.

Morawitz, W. M. L., P. J. Sutton, P. F. Worcester, B. D. Cornuelle, J. F. Lynch and R. Pawlowicz, 1996. Three-dimensional observations of a deep convective chimney in the greenland sea during winter 1988-89, *J. Phys. Oceanogr.*, 23, 1040-1056.

Niiler, P. P., 1975. Deepening of the wind-mixed layer. *J. Mar Res.*, 33(3), 405-422.

Olson, J. M., 1992. Conditional Instabilities of the Greenland Sea. MS Thesis, Naval Postgraduate School.

Orszag, S. A., I. Staroselsky and V. Yakhot, Some Basic Challenges for Large Eddy Simulation Research, in *Large Eddy Simulation of Complex Engineering and Geophysical Flows*, Ed. by B. Galperin and S. A. Orszag, 55-78, Cambridge University Press, 1993.

Paluskievicz, T., and R. D. Romea, 1997. A one-dimensional model for the parameterization of deep convection in the ocean. *Dyn. of Oceans and Atm.*, 26/1.

Price, J. F., R. A. Weller, and R. Pinkel, 1986. Diurnal cycling: observations and models of the upper ocean response to diurnal heating, cooling, and wind mixing. *J. Geophys. Res.*, 91, 8411-8427.

Rossby, C. G., and R. B. Montgomery, 1935. The layer of frictional influence in wind and ocean currents. *Pap. Phys. Oceanogr. Meteor.*, 3, Annual Reviews, 101 pp.

Rotta, J., 1951. Statische Theorie Nichthomogener Turbulenz, *Z. Physik*, Vol. 129, 547-572.

Rudels, B., and D. Quadfasel, 1991. Convection and deep water formation in the Arctic Ocean-Greenland Sea system. *J. Mar. Sys.*, 2, 435-450.

Rudels, B., D. Quadfasel, H. Friedrich, and M.-N. Houssais, 1989. Greenland Sea convection in the winter of 1987-1988. *J. Geophys. Res.*, 94, 3223-3227.

Sander, J., D. Wolf-Gladrow and D. Olbers, 1995. Numerical studies of open ocean deep convection. *J. Geophys. Res.*, 100, C10, 20, 579-600.

Schott, F., M. Visbeck, and J. Fischer, 1993. Observations of vertical currents and convection in the central Greenland Sea during the winter of 1988/1989. *J. Geophys. Res.*, 98, 14,401-14,421.

Send, U., and J. C. Marshall, 1995. Integral effects of deep convection. *J. Phys. Oceanogr.*, 25, 855-872.

Skyllingstad, E. D., T. Paluszakwics, D. W. Denbo, W. D. Smyth, 1996. Nonlinear vertical mixing processes in the ocean: modeling and parameterization. *Physica D*, 98, 574-593, Elsevier Science.

Smagorinsky, J., General circulation experiments with the primitive equations, *Mon. Wea. Rev.*, 91, 99-165, 1963.

Stone, R. E., 1997. Deep mixed layer entrainment. Master's Thesis, Naval Postgraduate School, Monterey, Ca.

Straneo, F., and M. Kawase, 1999. Comparisons of localized convection due to localized forcing and to preconditioning. *J. Phys. Oceanogr.*, 29, 55-68.

Straneo, F., M. Kawase, and S. C. Riser, 1999. Slantwise convection in a horizontally stratified ocean. Submitted to *J. Mar. Res.*

Stull, R. B., 1988. *An introduction to boundary layer meteorology*, p. 478. Dordrecht: Kluwer Academic Publishers.

Visbeck, M., J. Fischer, and F. Schott, 1995. Preconditioning in the Greenland Sea for deep convection: ice formation and ice drift. *J. Geophys. Res.*, 100, 18,489-18,502.

Worcester, P. F., J. F. Lynch, W. M. L. Morawitz, R. Pawlowicz, P. J. Sutton, B. D. Cornuelle, O. M. Johannessen, W. H. Munk, W. B. Owens, R. Shuchman, and R. C. Spindel, 1993. Evolution of the large-scale temperature field in the Greenland Sea during 1988-89 from tomographic measurements. *Geophys. Res. Ltrs.*, 20, 20, 2211-2214.

Yoshikawa, Y., K. Akitomo, and T. Awaji, 1999. Convection in the stratified ocean with background geostrophic current. Proceedings of the CREAMS'99 Int'l Symp.

Zilitinkevich, S. S., D. V. Chalikov and Yu. D. Resnyansky, 1979. Modeling the oceanic upper layer. *Oceanol. Acta.*, 2, 219-240.

APPENDIX. FIGURES

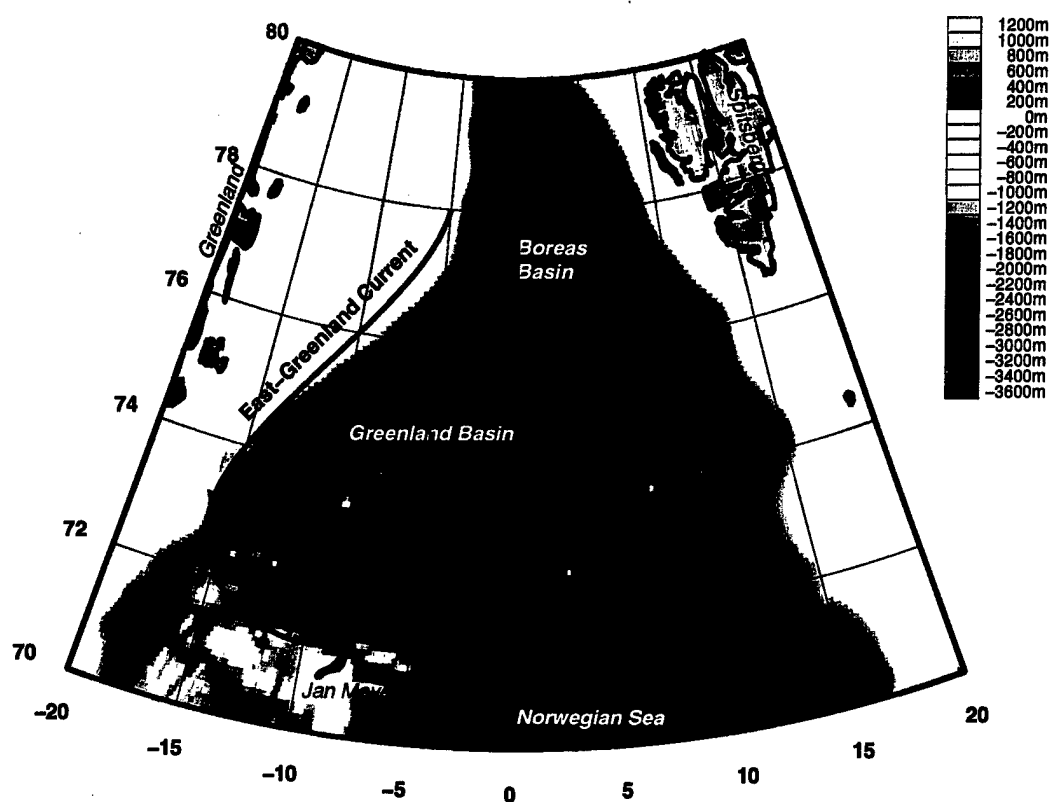


Figure 1. Schematic of the Greenland Sea.

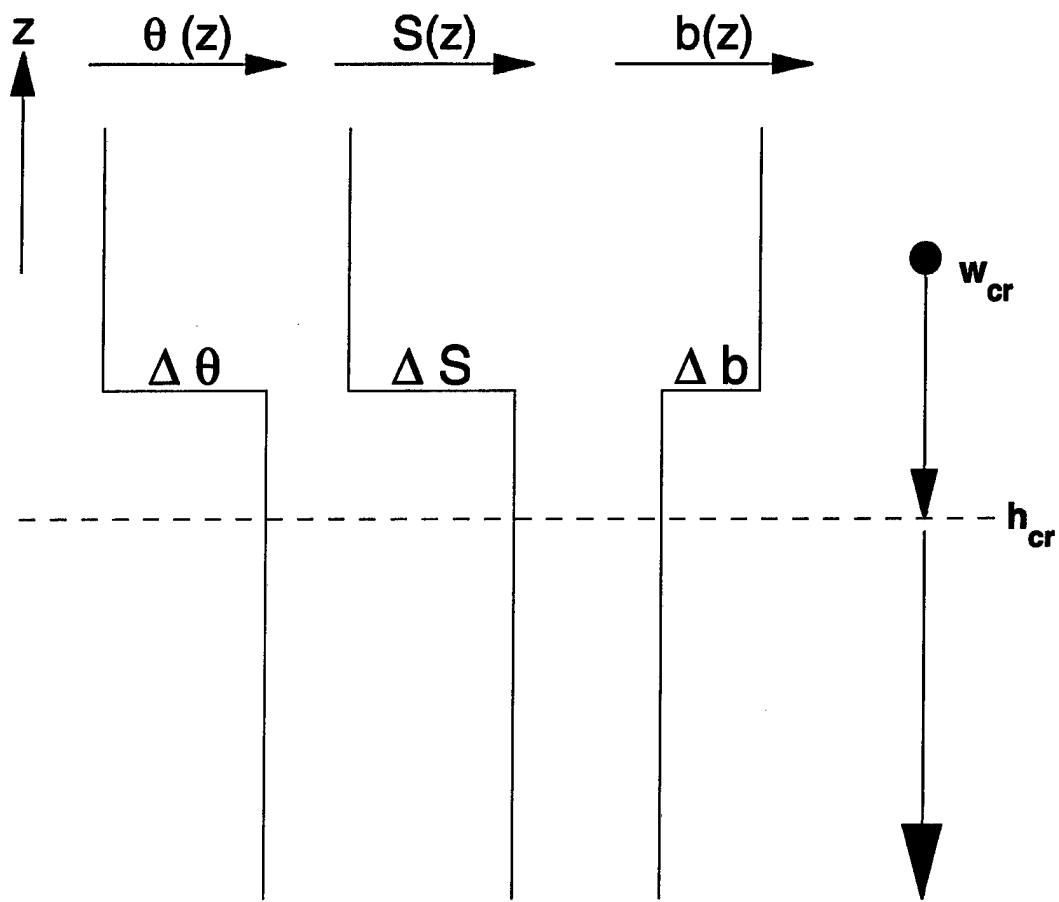


Figure 2. Thermobaric Plume Schematic shows parameters used in theoretical discussion. A cold (near freezing) and fresh mixed layer overlies a relatively warm and saline layer. If a mixed-layer parcel has downward velocity equal to or greater than the critical velocity w_{cr} , its momentum will carry it to the critical depth where its relative buoyancy will be negative, and it will be accelerated downward.

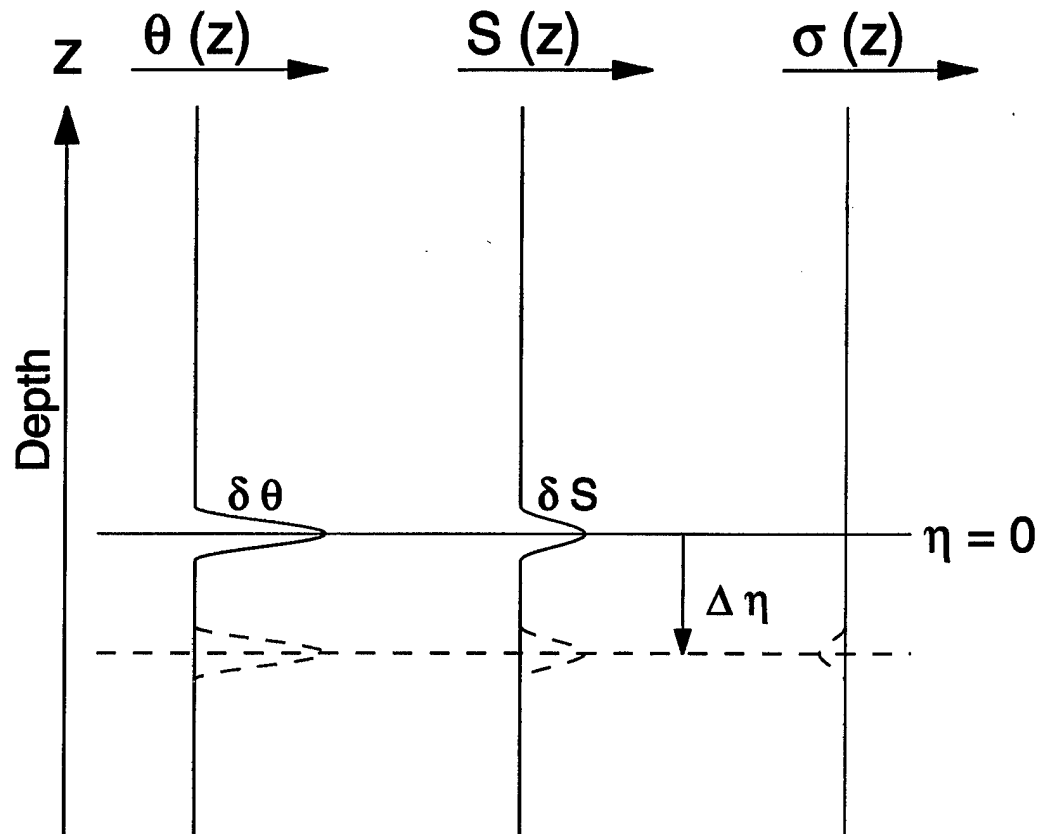


Figure 3. Thermobaric Interleaving Schematic shows parameters used in theoretical discussion. A density-compensated warm and saline intrusion will be stable to vertical displacements. A cold and fresh intrusion will be stable only if the background stratification is stronger than a critical value N_c^2 .

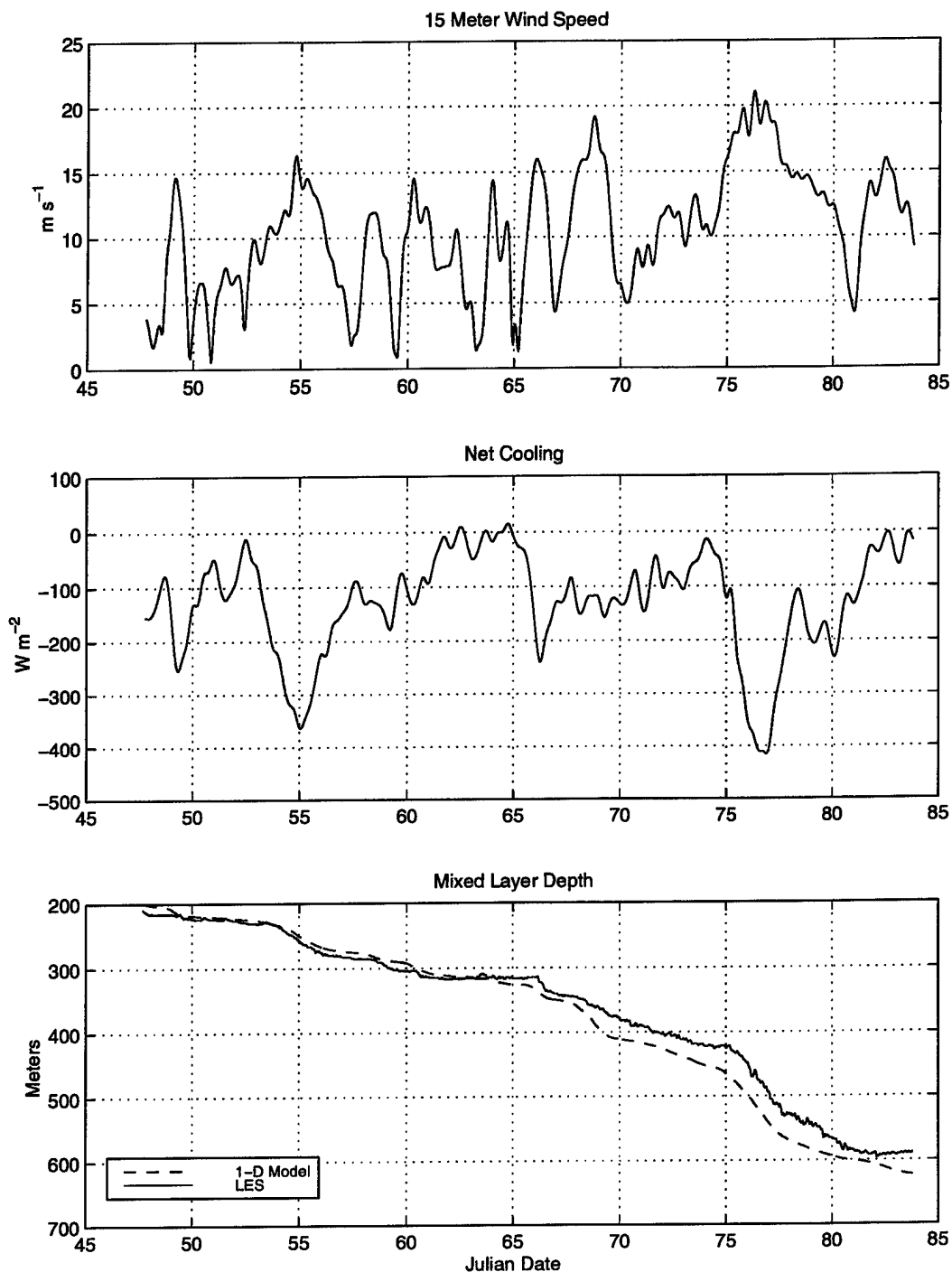


Figure 4. Forcing and resulting mixed-layer deepening as predicted by the one-dimensional model and by LES.

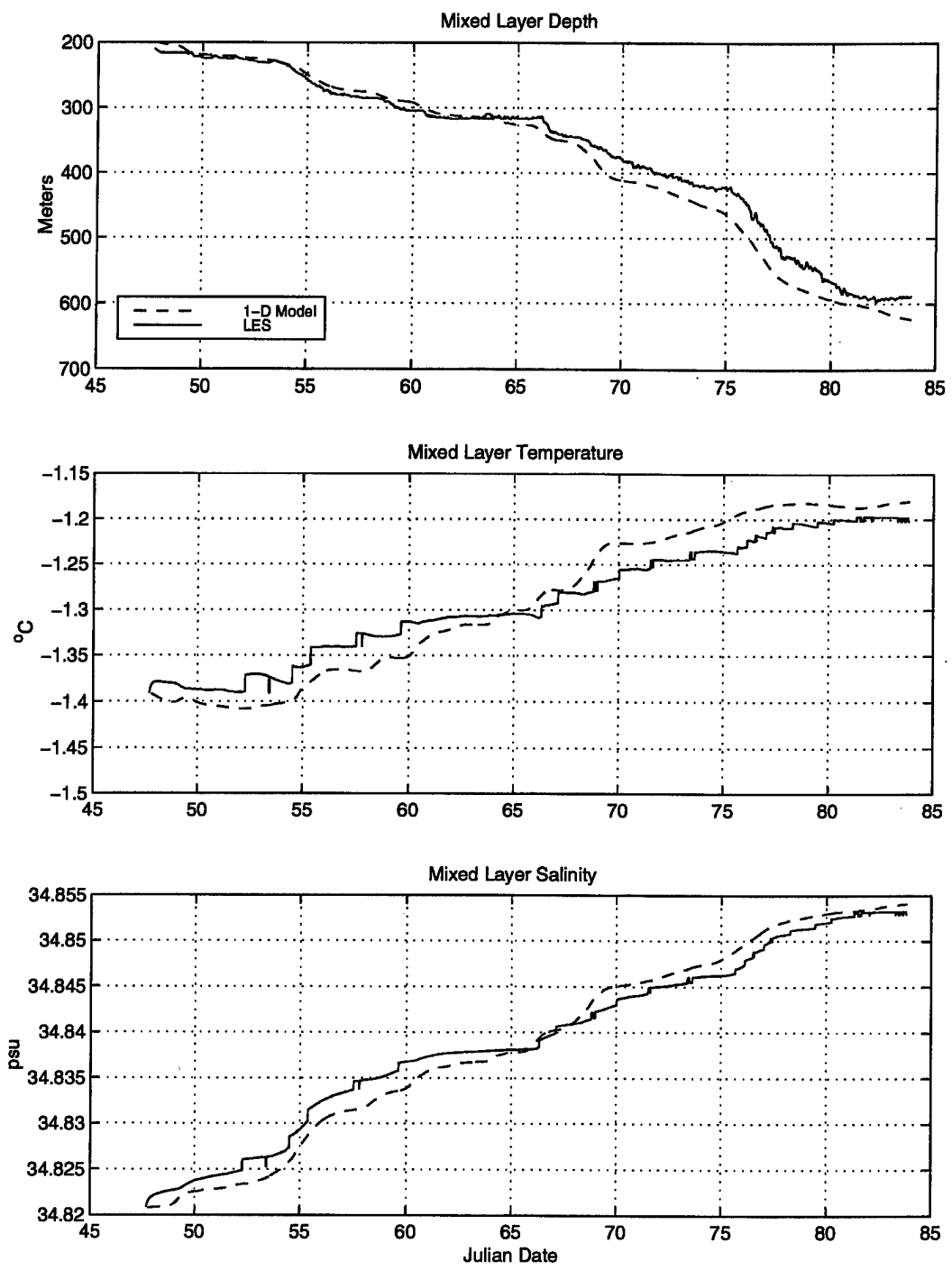


Figure 5. Mixed-layer deepening, temperature, and salinity as predicted by the one-dimensional model and by LES.

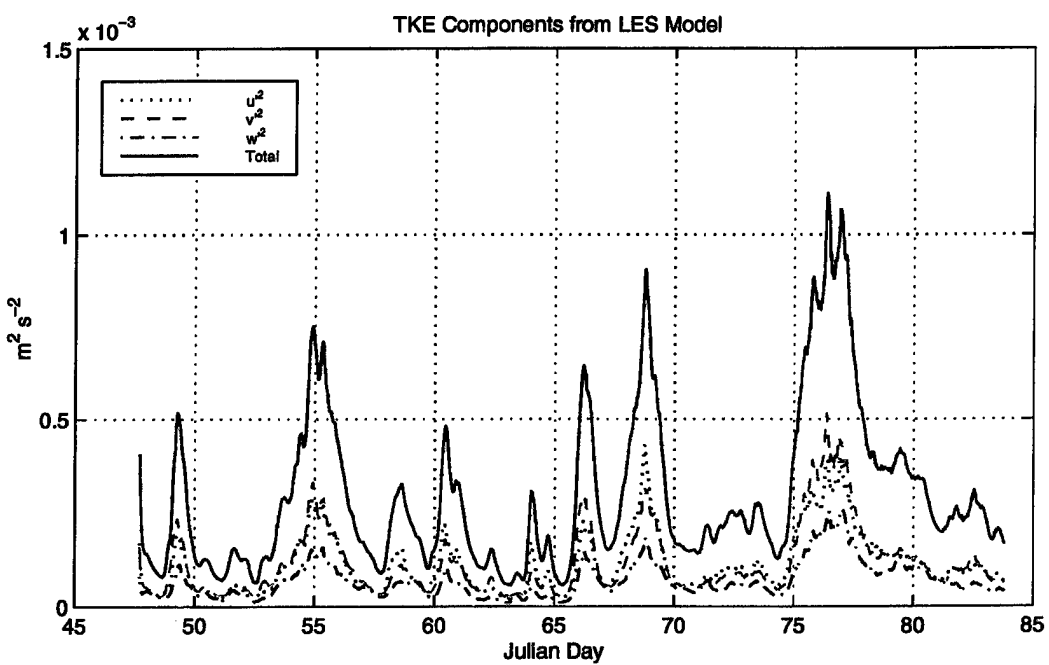
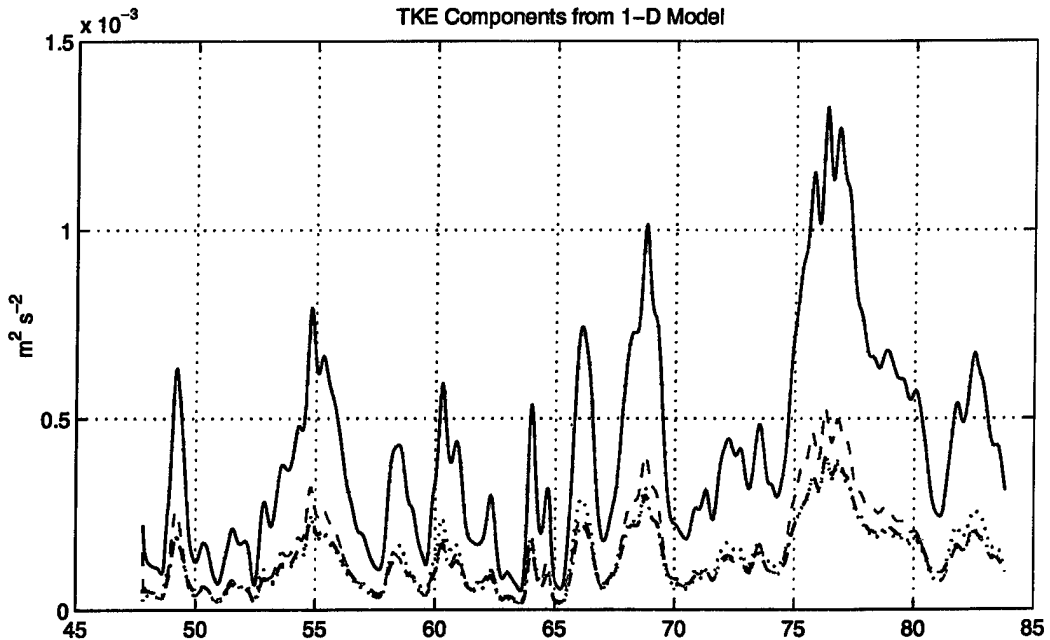


Figure 6. Turbulent kinetic energy (TKE) components as predicted by the one-dimensional model and by LES.

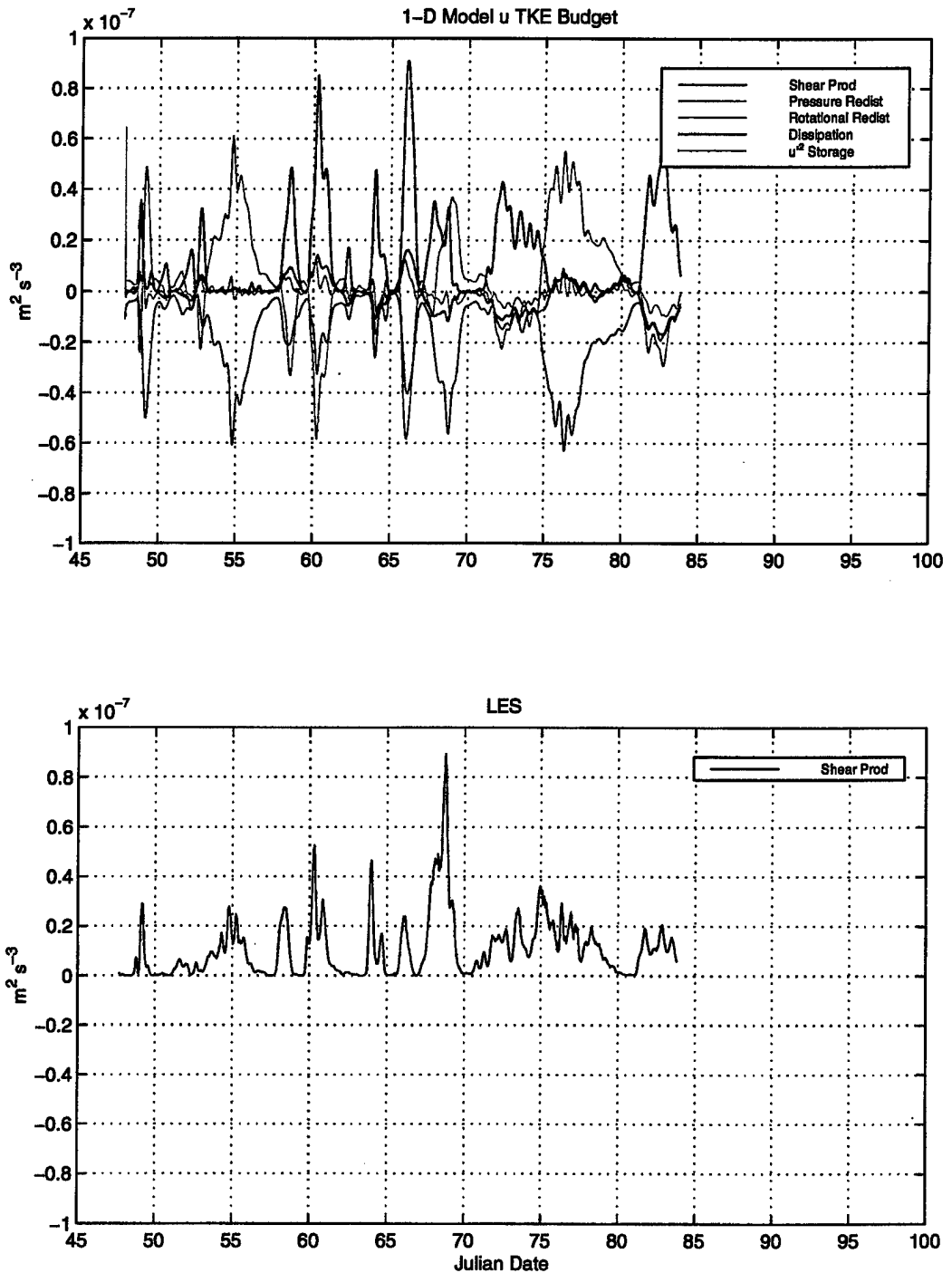


Figure 7. Contributions to $\overline{u'^2}$ as computed by the one-dimensional model and by LES.

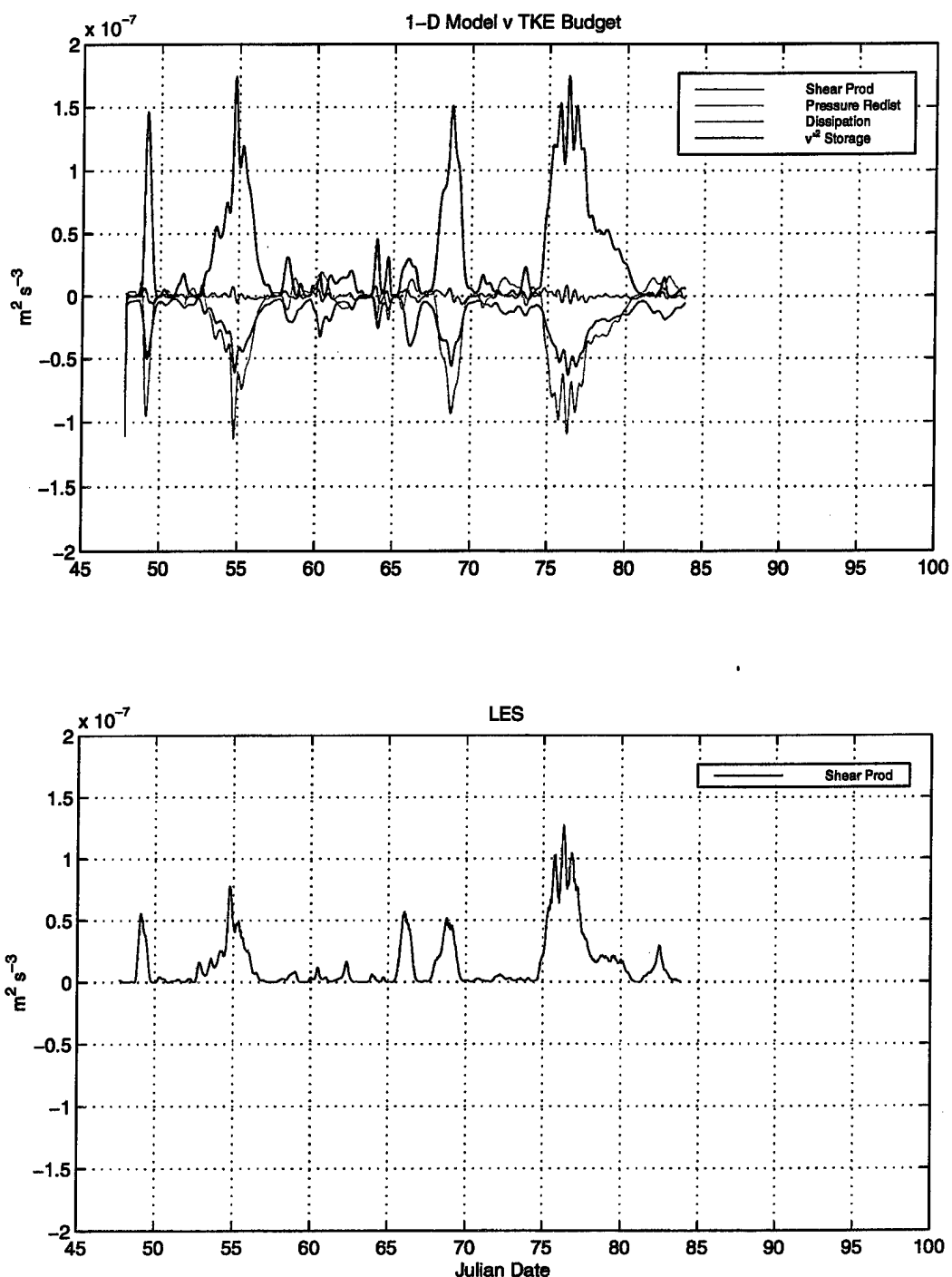


Figure 8. Contributions to $\overline{v'^2}$ as computed by the one-dimensional model and by LES.

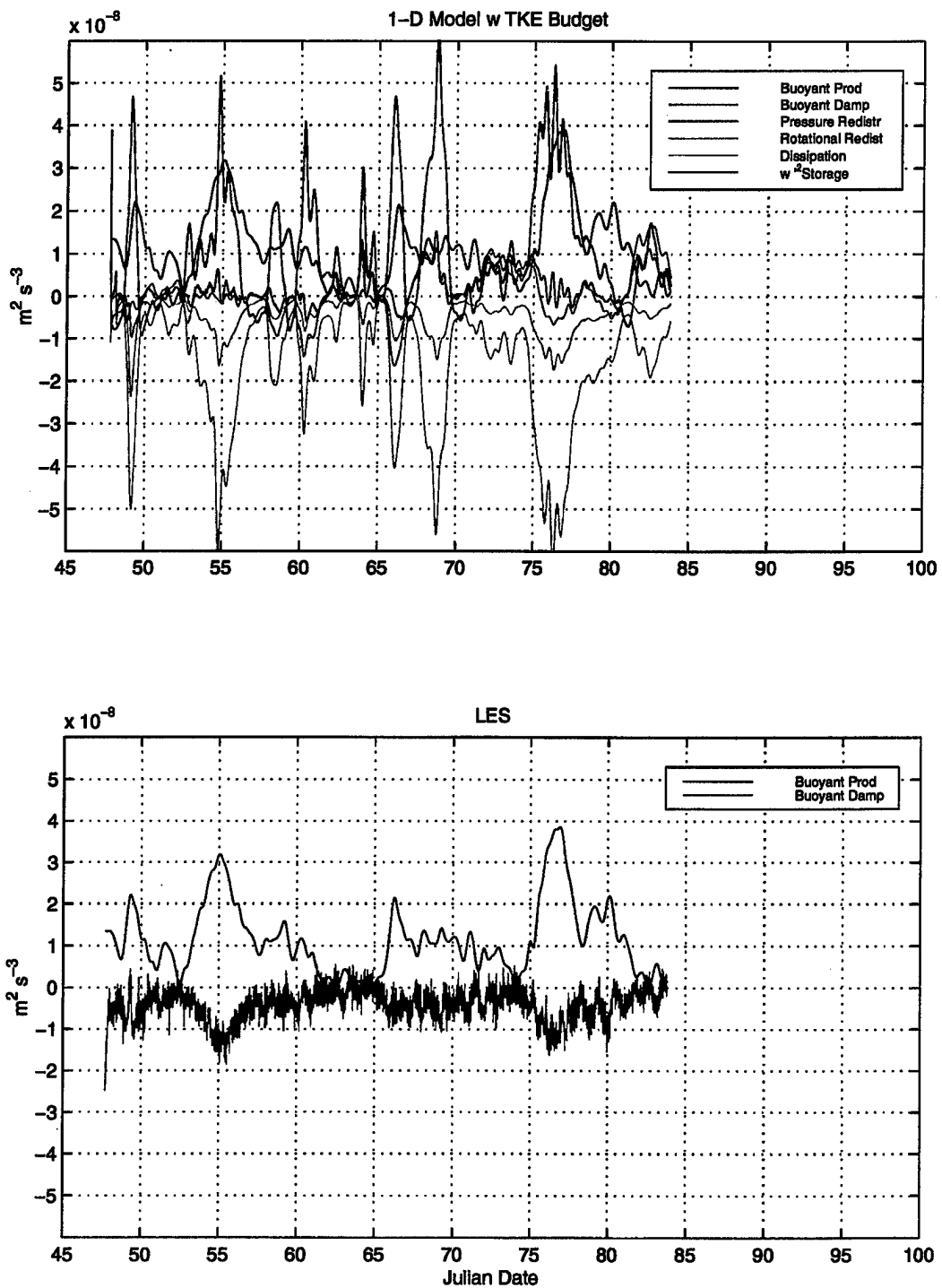


Figure 9. Contributions to $\overline{w'^2}$ as computed by the one-dimensional model and by LES.

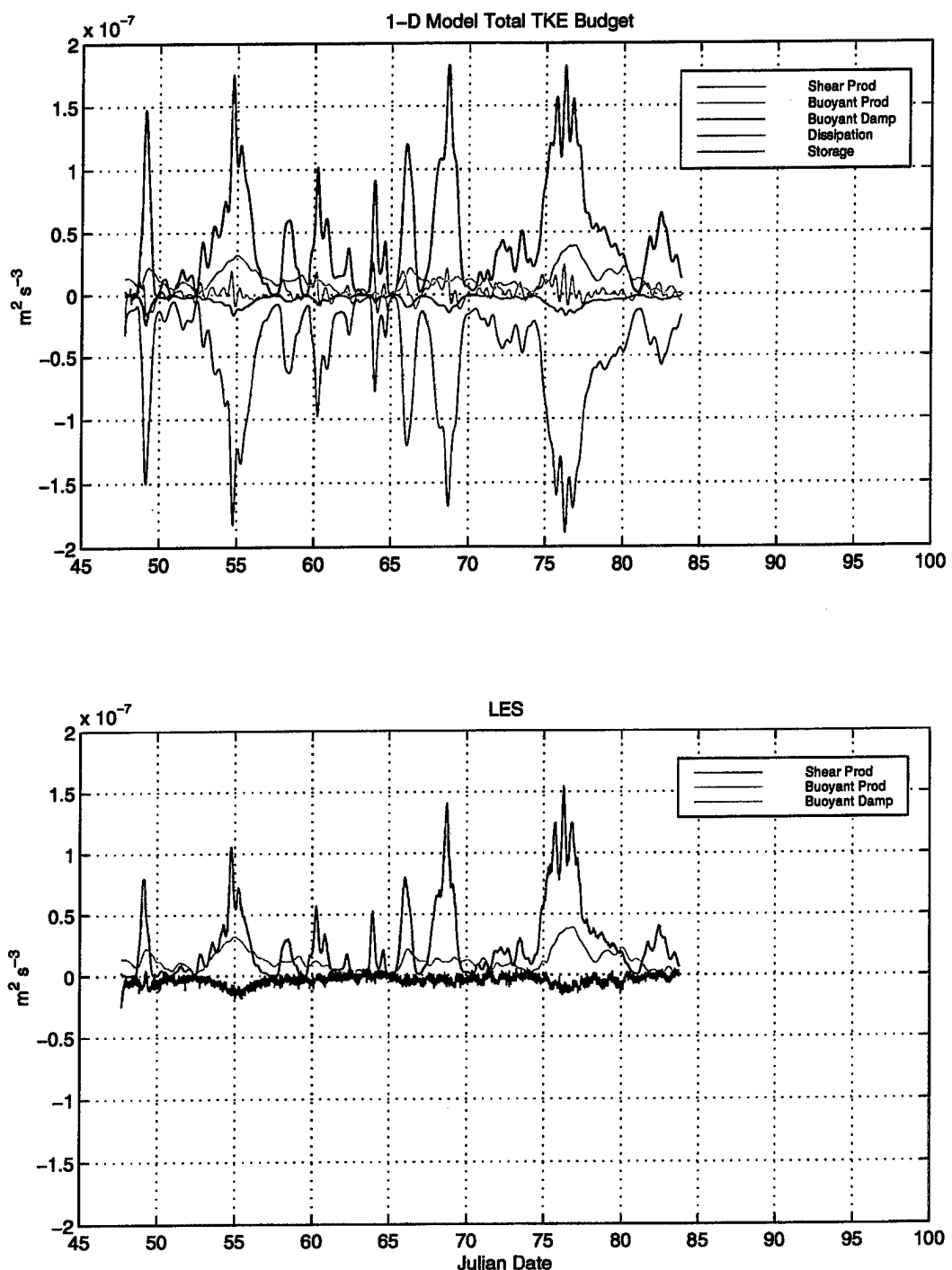


Figure 10. TKE contributions as computed by the one-dimensional model and by LES.

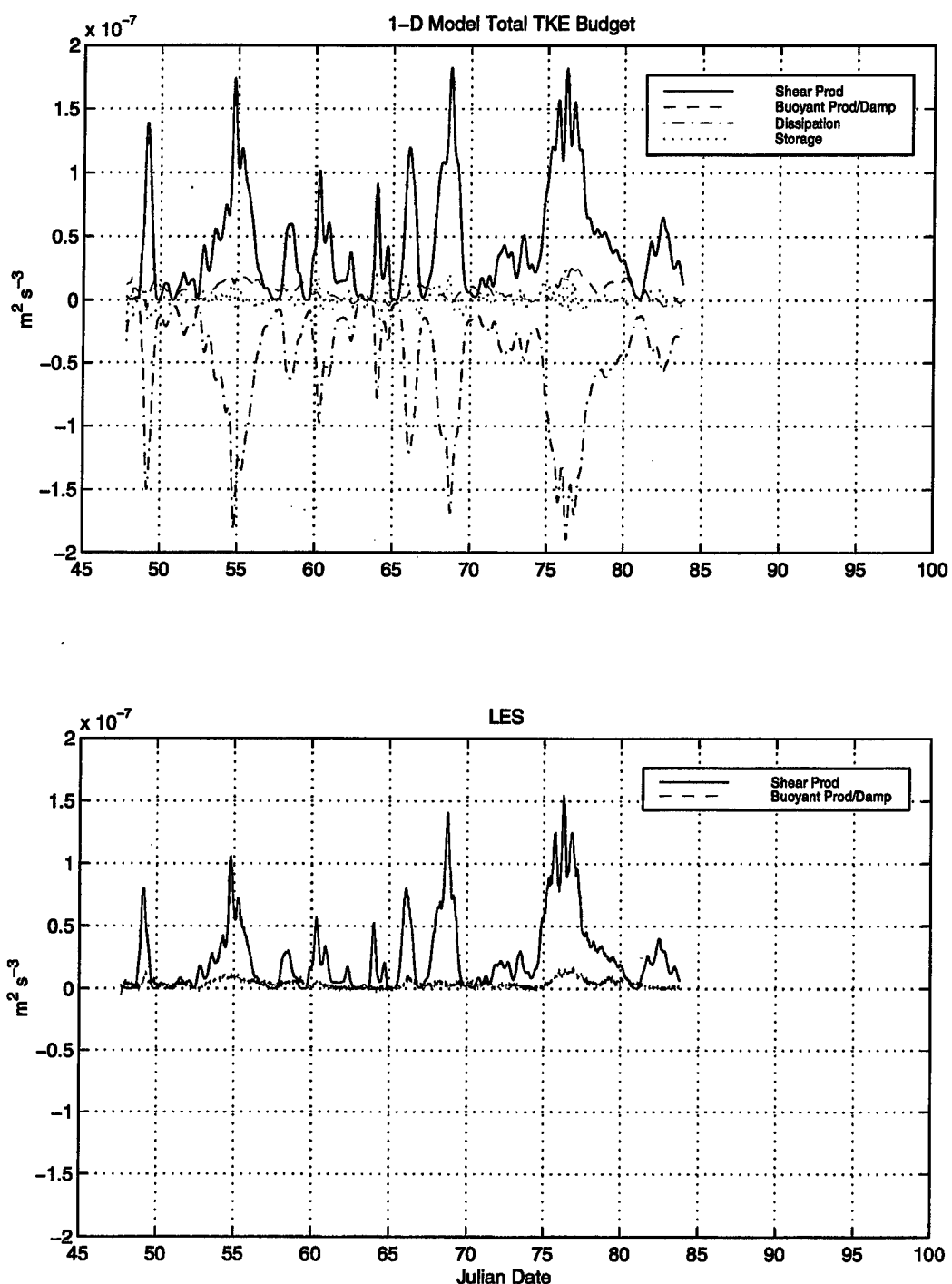


Figure 11. TKE contributions as computed by the one-dimensional model and by LES. Differs from Figure 9 in that surface and entrainment contributions to buoyant production/damping have been summed.

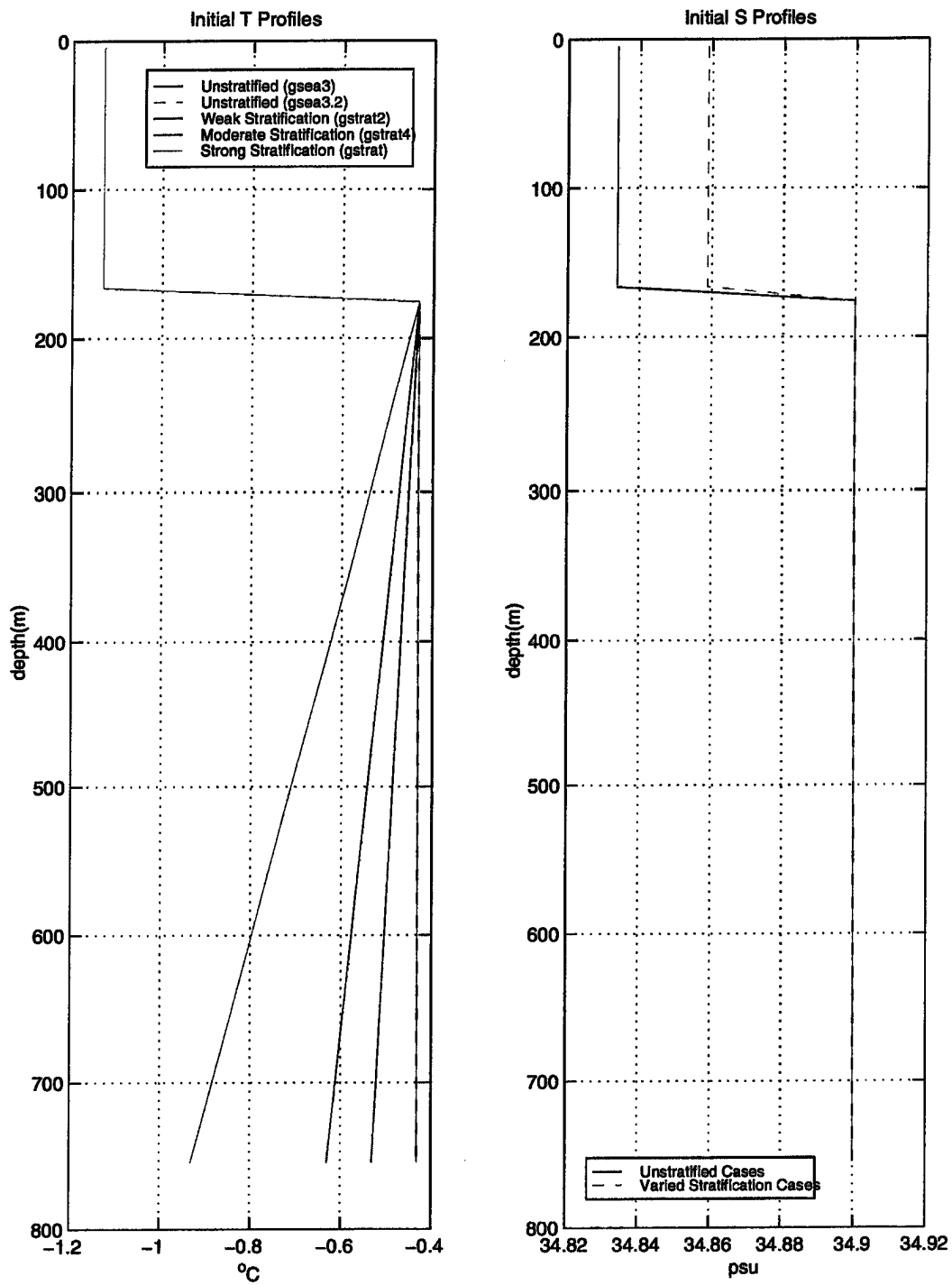


Figure 12. Initial profiles of temperature and salinity for the thermobaric plume experiments.

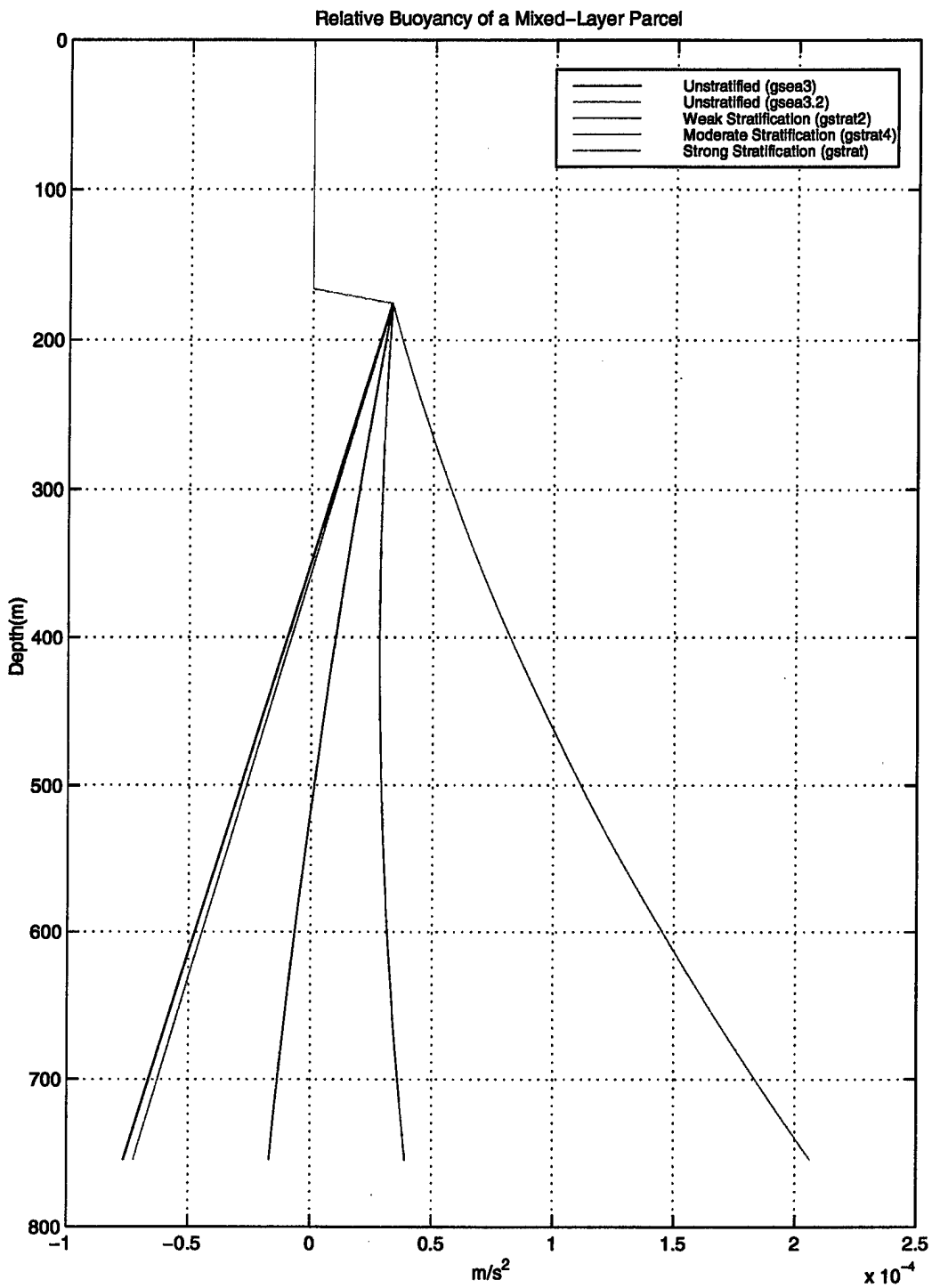


Figure 13. Profiles of buoyancy for a mixed-layer parcel if plunged to any depth below the initial interface.

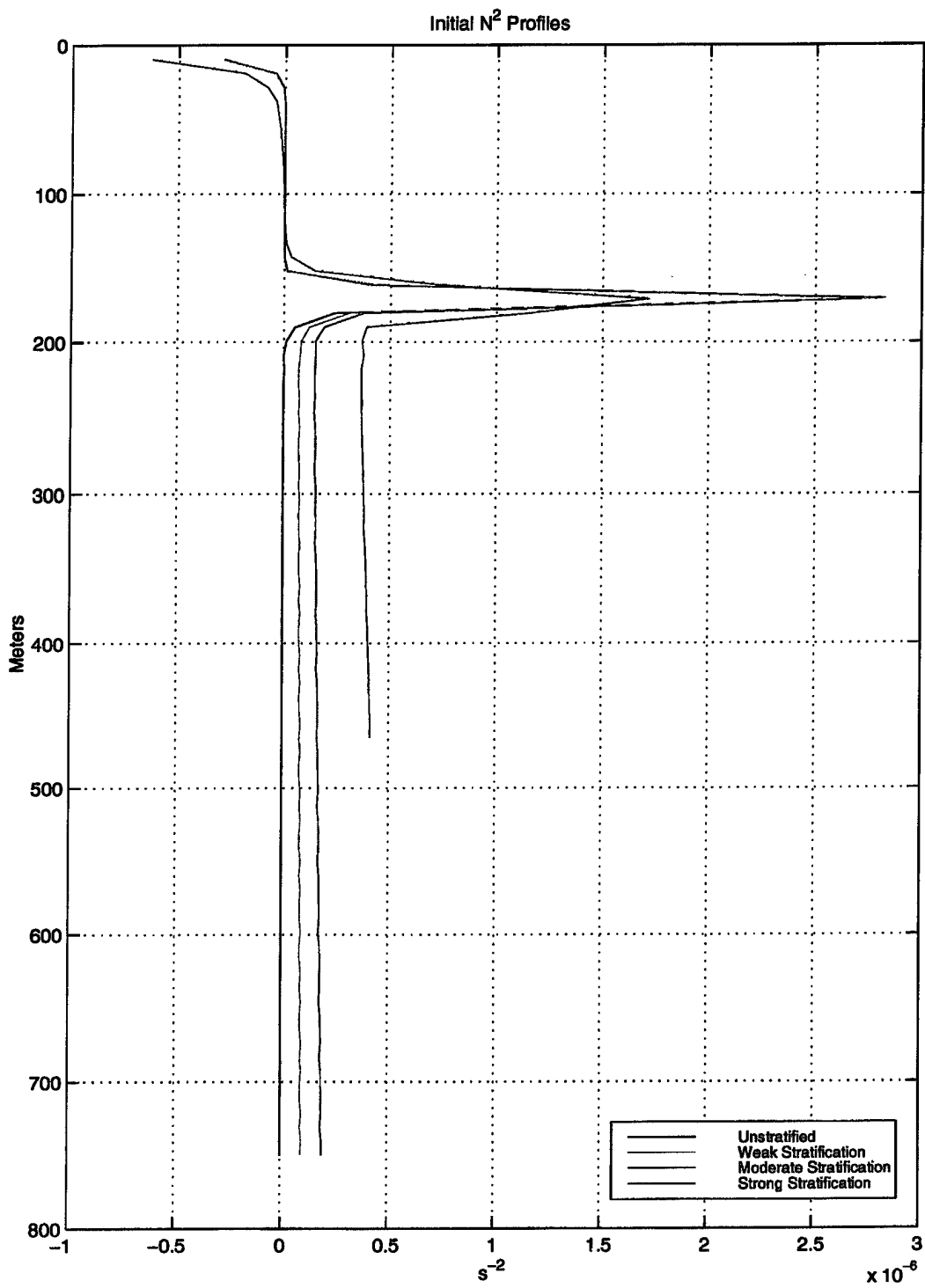


Figure 14. Initial N^2 profiles for the varied stratification cases.

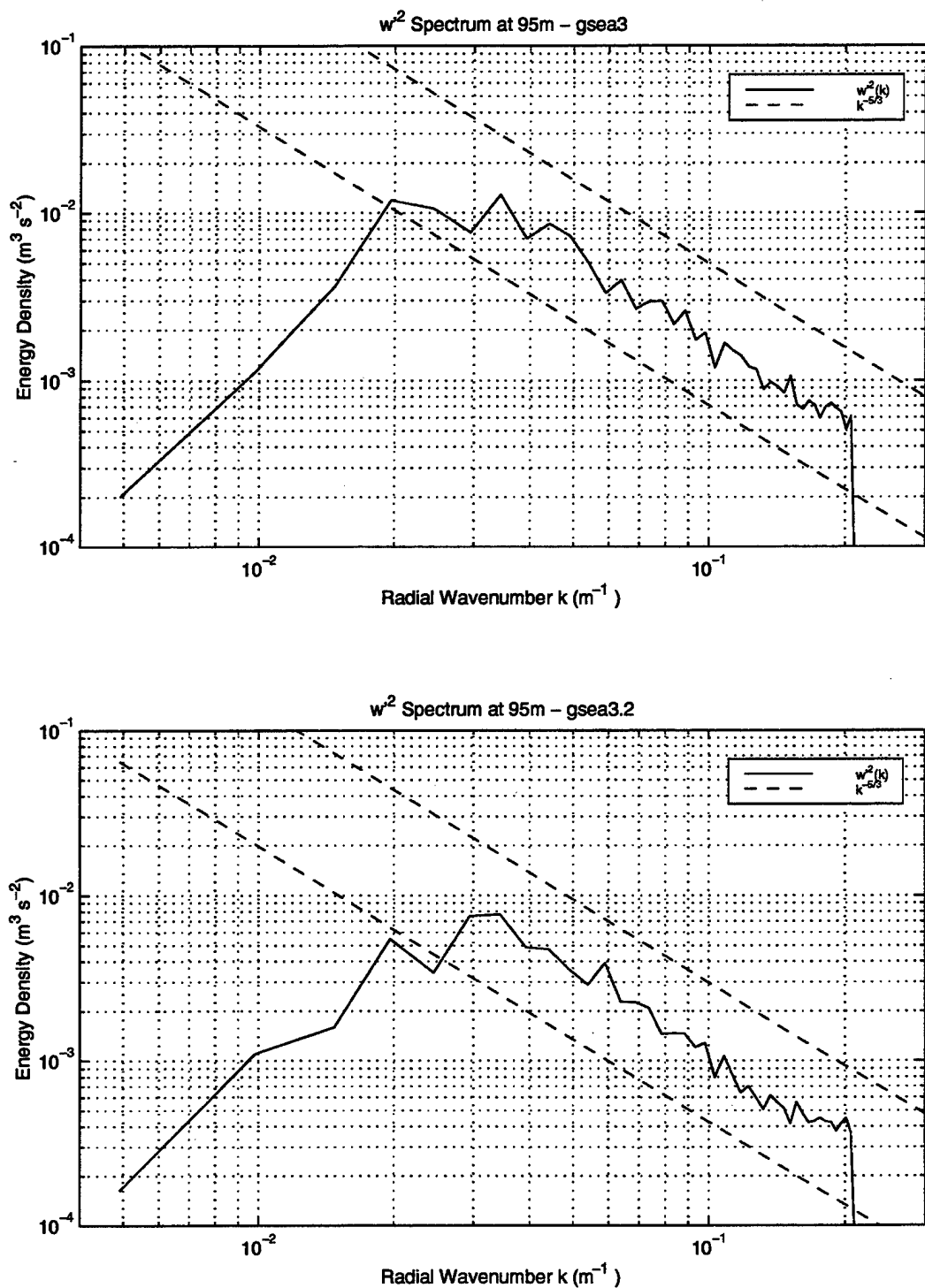


Figure 15. Energy-density spectra for vertical velocity at 95m ten hours after the onset of detrainment for two unstratified experiments. Top: gsea3 Bottom: gsea3.2

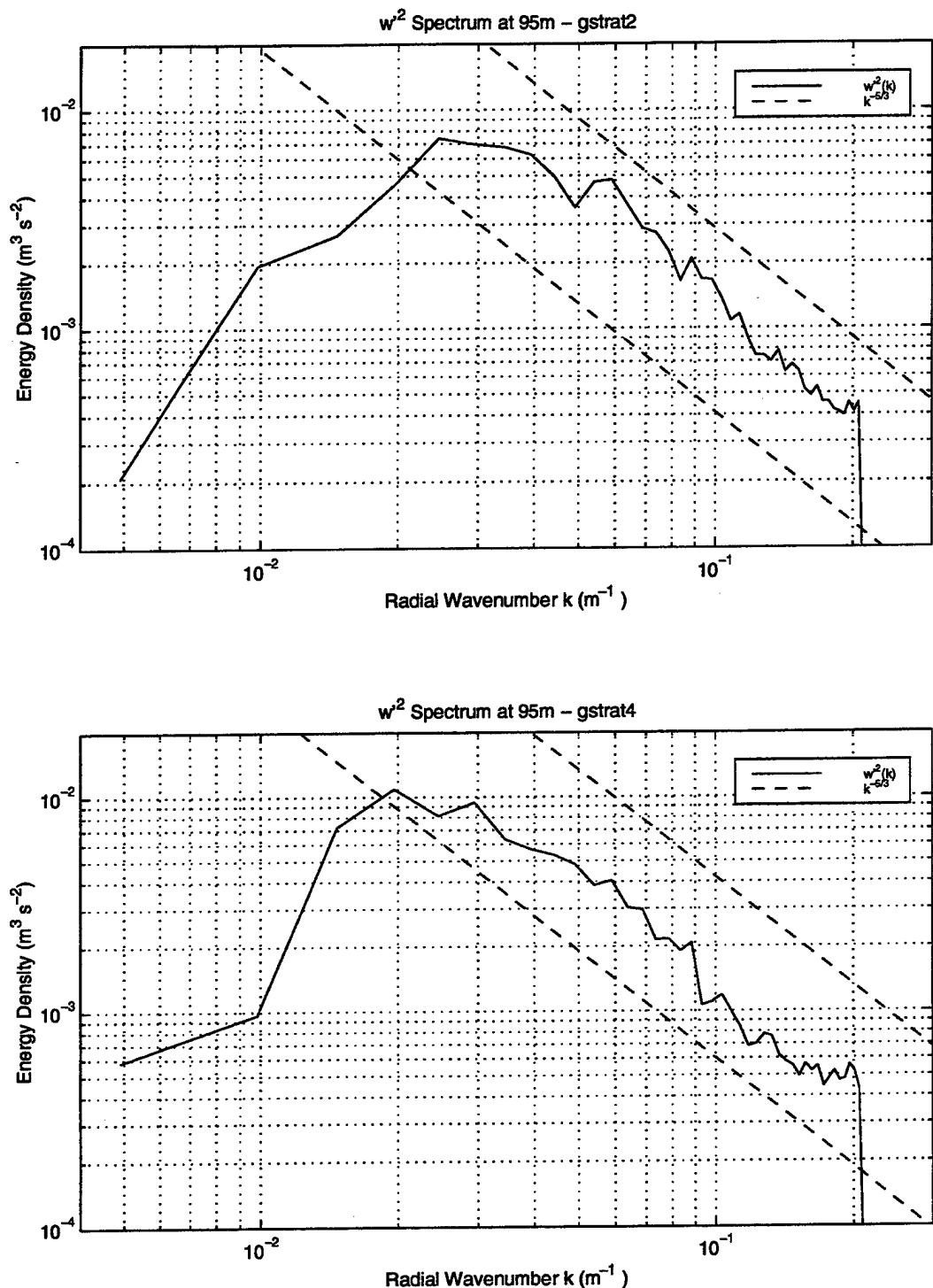


Figure 16. Energy-density spectra for vertical velocity at 95m ten hours after the onset of detrainment for two unstratified experiments. Top: gstrat2 Bottom: gstrat4



Figure 17. A field of detraining thermobaric plumes, rendered using an isosurface of temperature. Width of domain is 2.56km. Plumes are descending about 400m below the interface, which is at a depth of 200m.

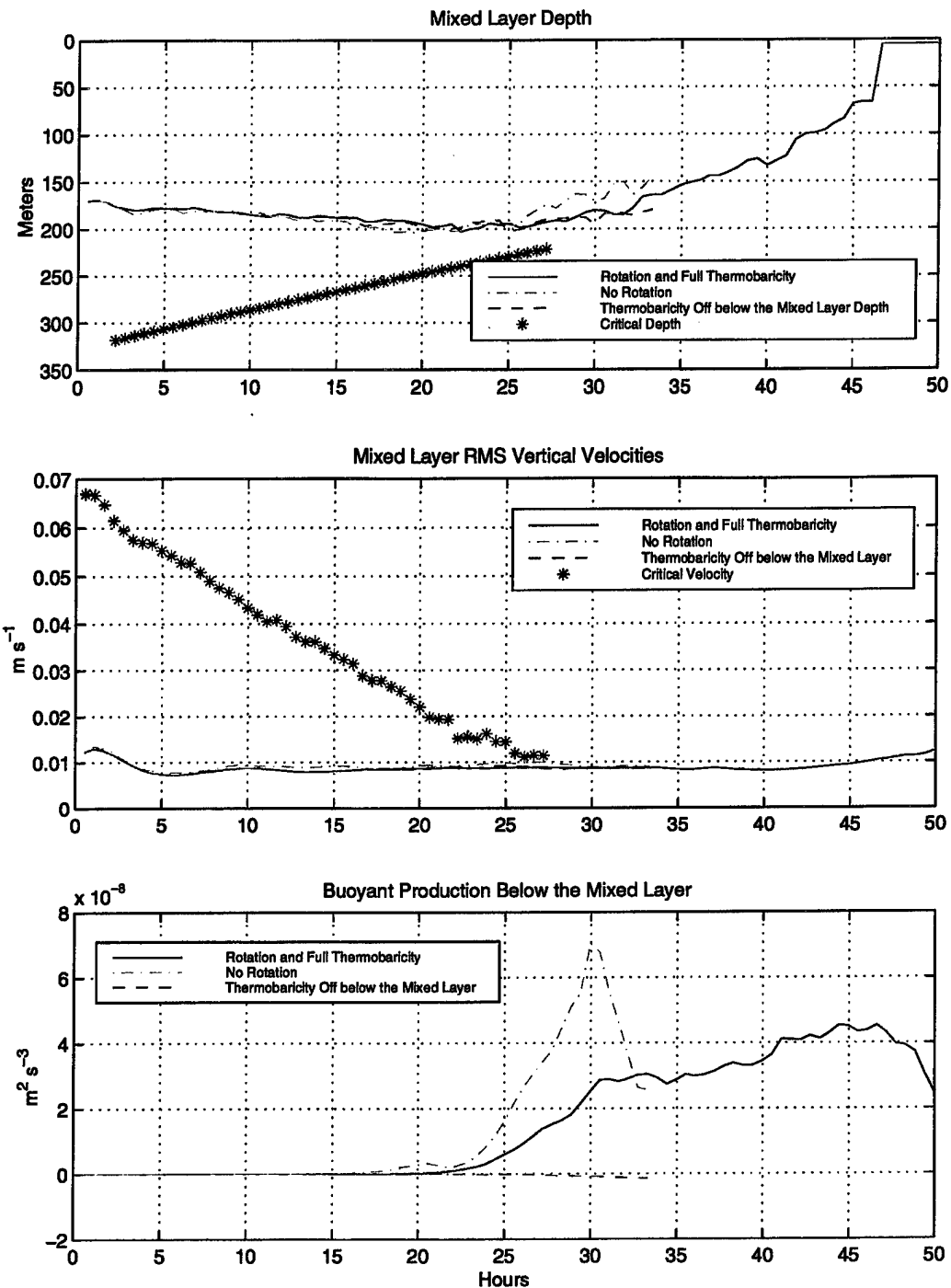


Figure 18. Time series from unstratified experiments. Top: LES-predicted mixed-layer depth and critical depth for thermobaric plume formation. Center: Bulk mixed-layer w_{rms} and critical velocity. Bottom: Bulk buoyant production below the mixed layer.

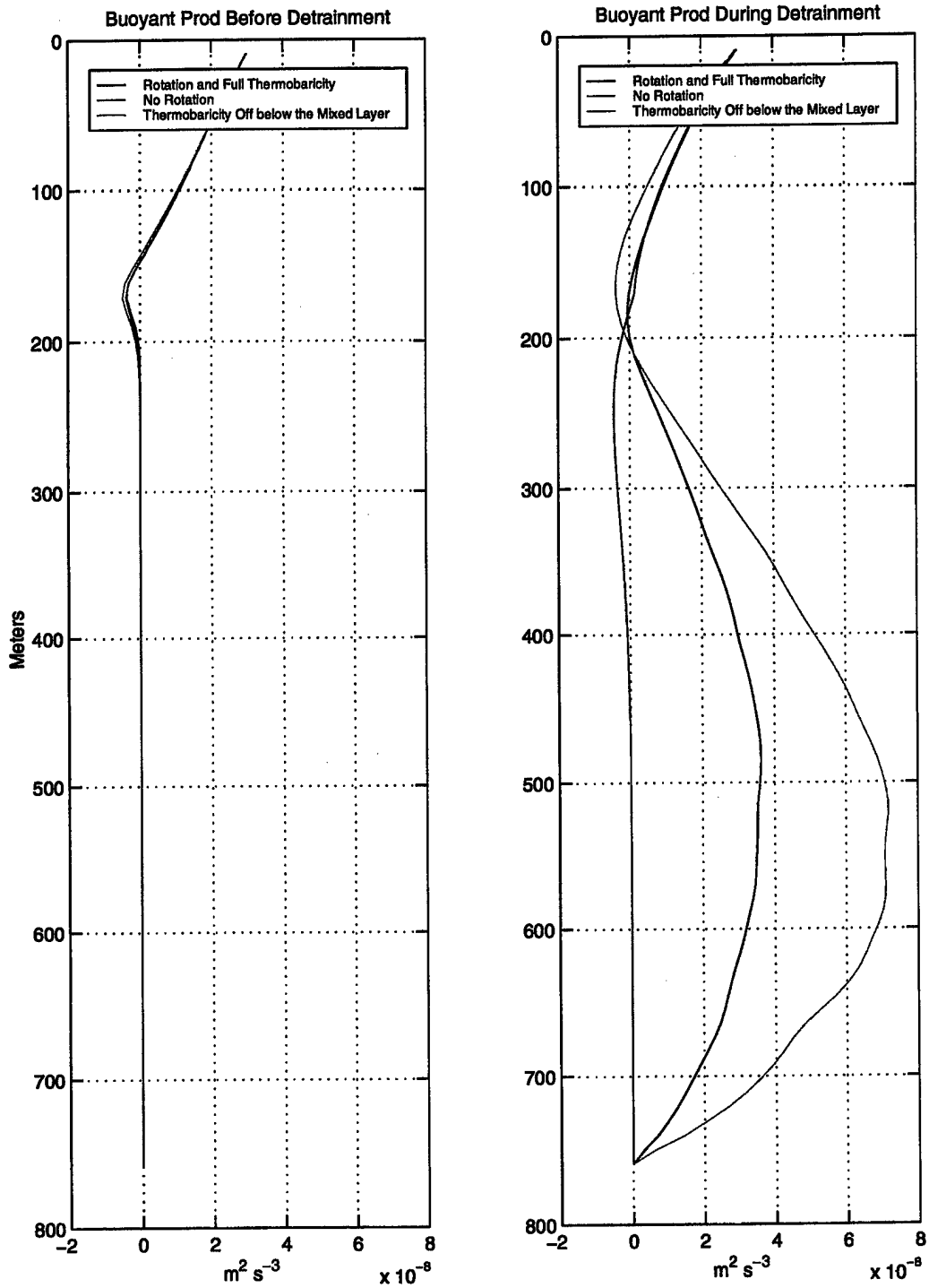


Figure 19. Profiles from unstratified experiments. Buoyant production (buoyancy flux) before detrainment (left) and during detrainment (right).

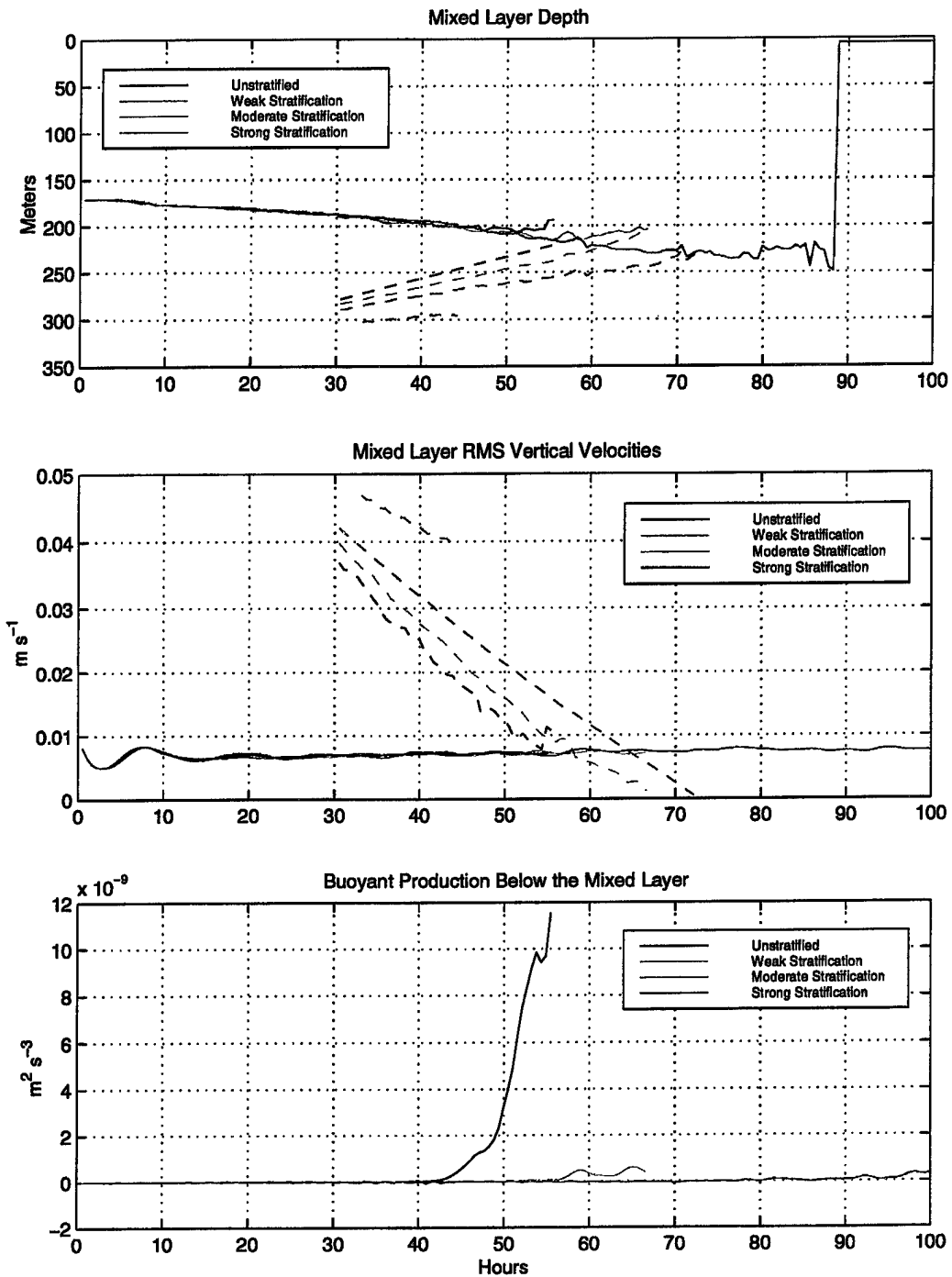


Figure 20. Time series from experiments varying the stratification. Dashed lines are critical values. Top: LES-predicted mixed-layer depth and critical depth for thermobaric plume formation. Center: Bulk mixed-layer w_{rms} and critical velocity. Bottom: Bulk buoyant production below the mixed layer.

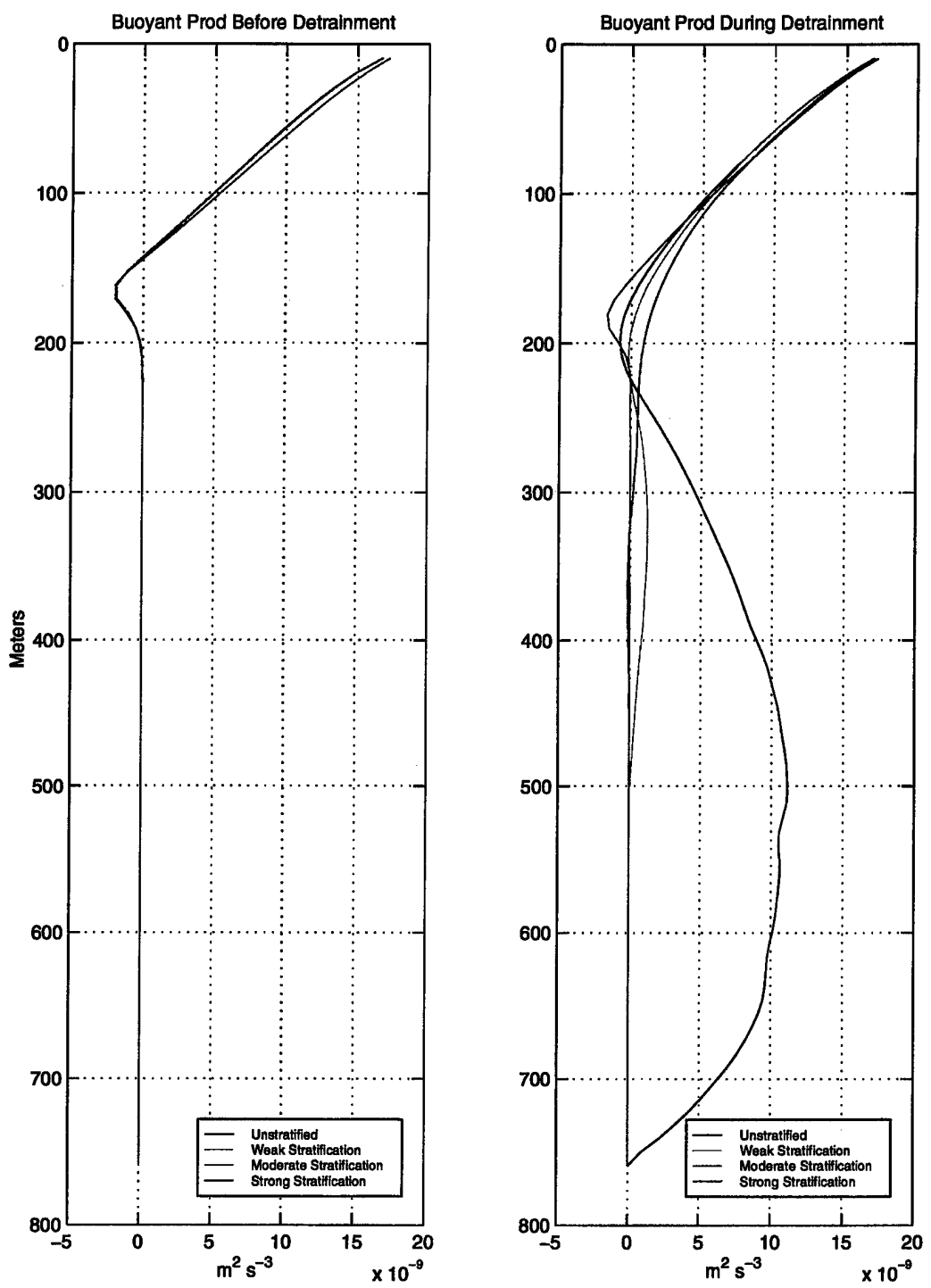


Figure 21. Profiles from experiments varying the stratification. Bouyant production (buoyancy flux) before detrainment (left) and during detrainment (right).

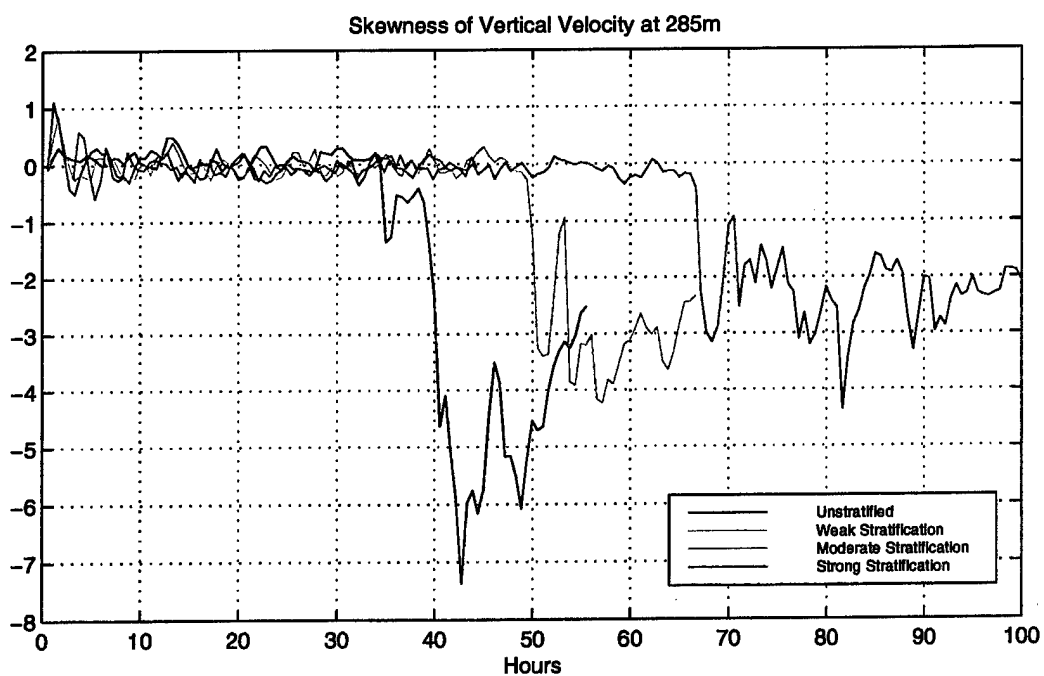
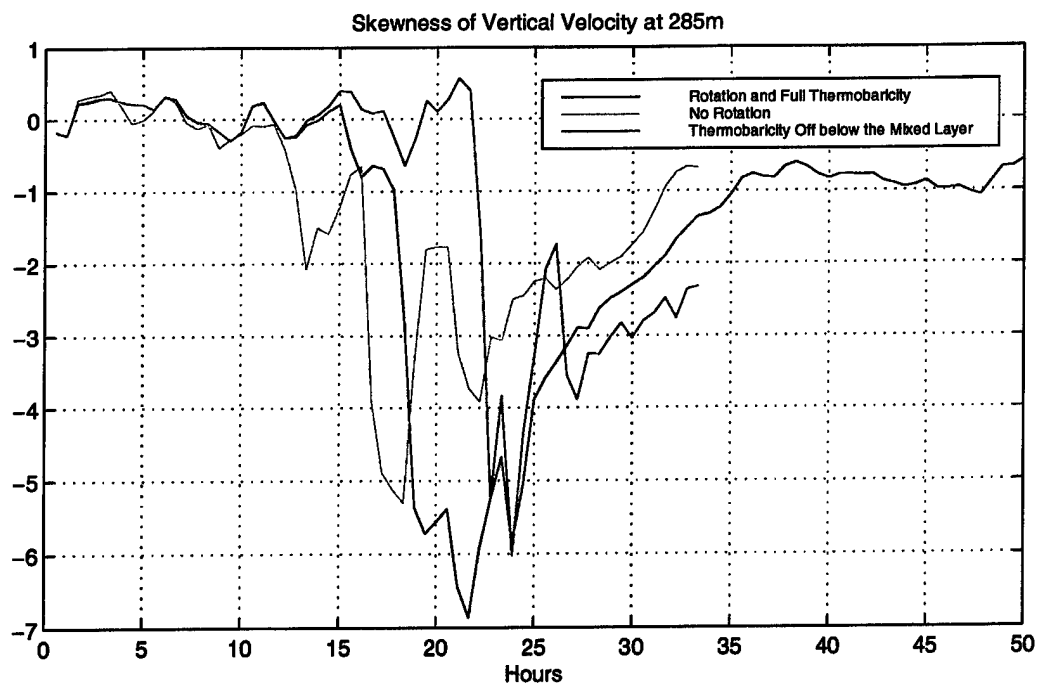


Figure 22. Skewness of Vertical Velocity at 285m. Top: from unstratified experiments. Bottom: from experiments varying the stratification.

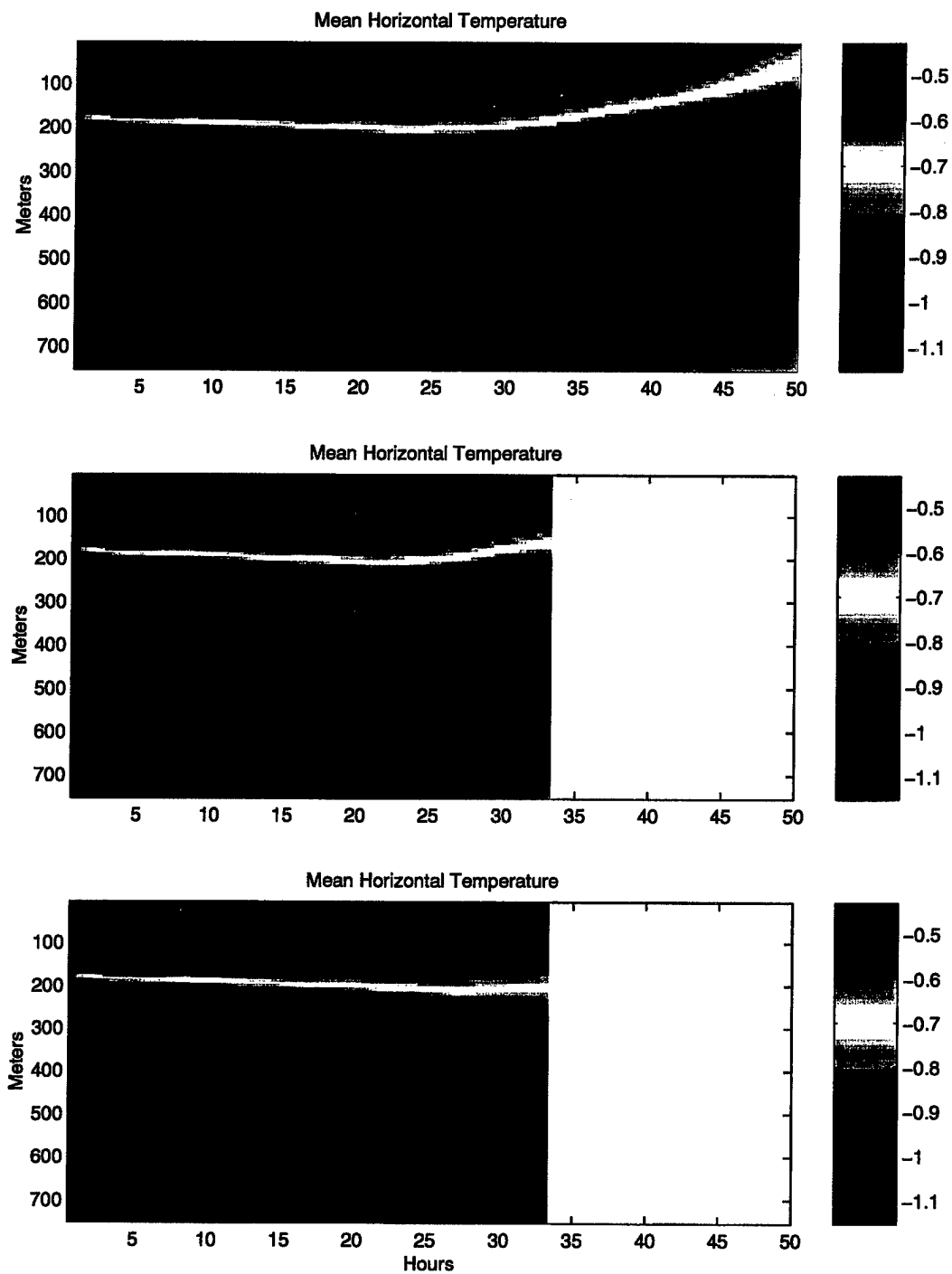


Figure 23. Plots of LES horizontal mean temperature as a function of depth and time, from unstratified experiments. Top: Rotation and Full Thermobaricity, Center: No Rotation, Bottom: Thermobaricity Off Below the Mixed Layer

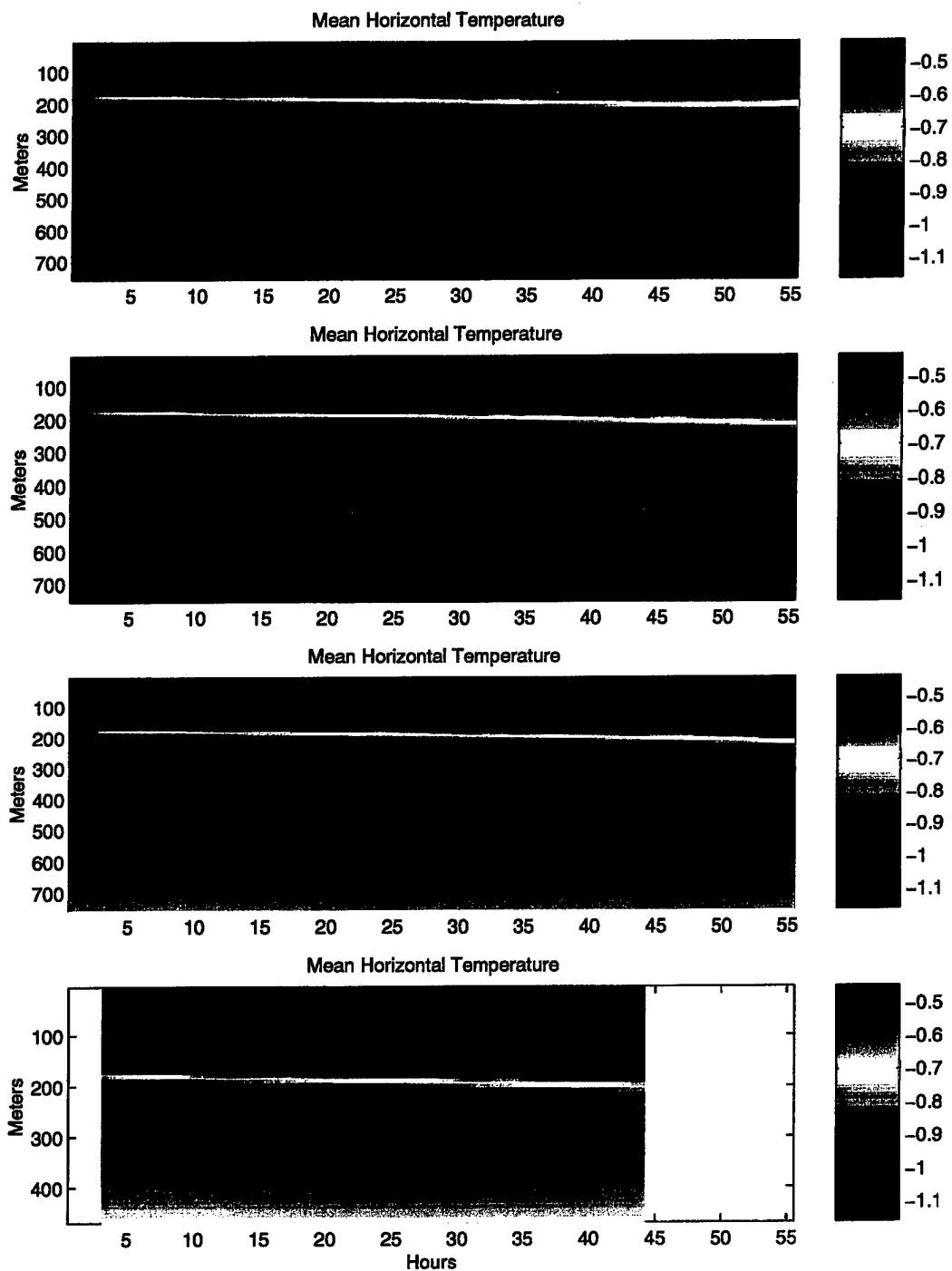


Figure 24. Plots of LES horizontal mean temperature as a function of depth and time, from experiments varying the stratification. Top: Unstratified, Upper Center: Weak Stratification, Lower Center: Moderate Stratification, Bottom: Strong Stratification.

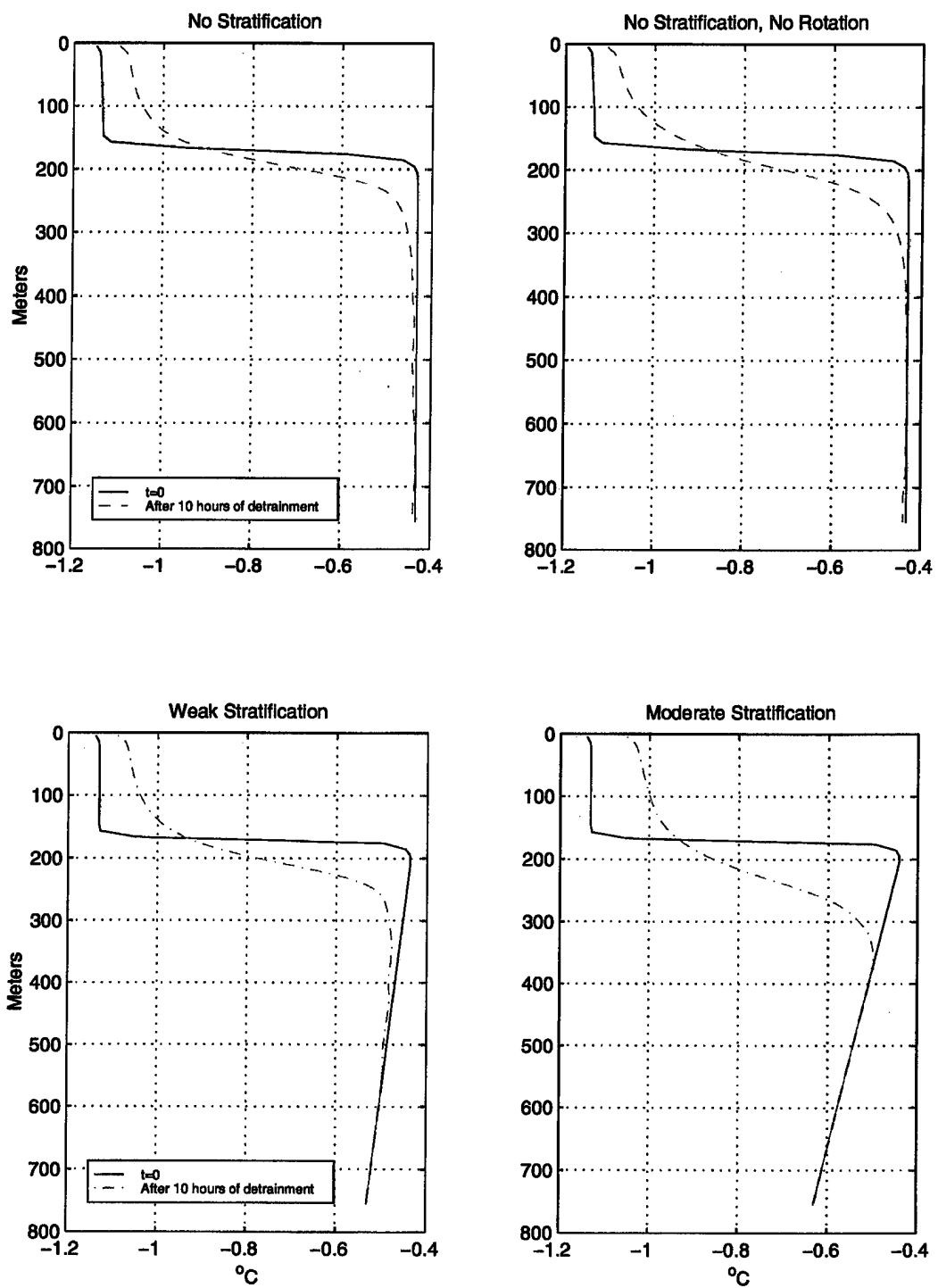


Figure 25. Profiles of temperature at the initial time and 10 hours after the onset of detrainment.

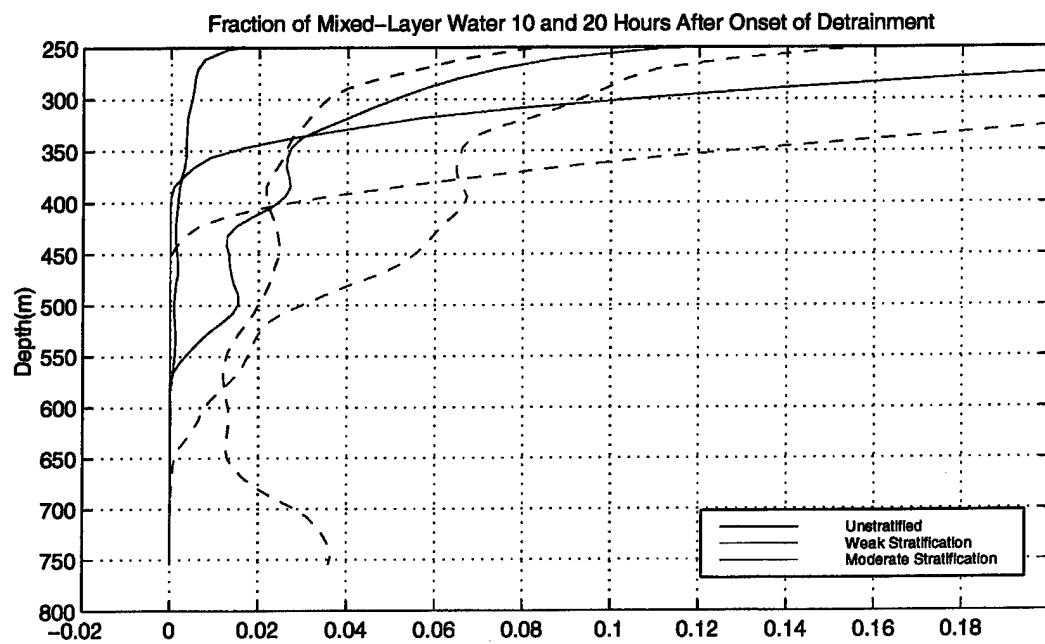
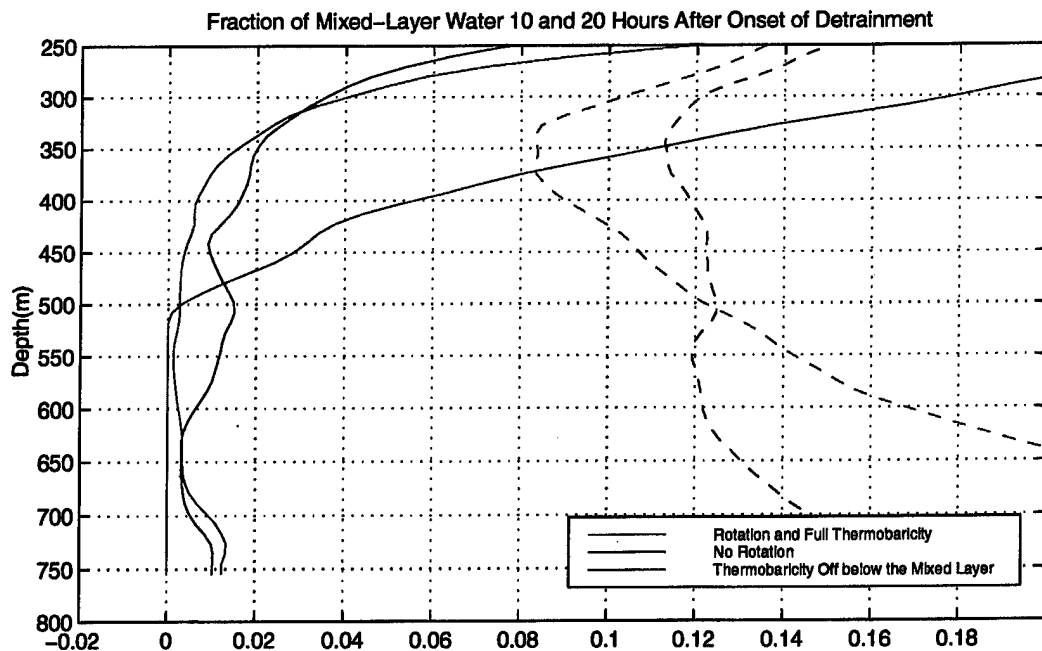


Figure 26. Profiles of the fraction of mixed-layer water present 10 and 20 hours after the onset of detrainment. Solid lines are at 10 hours; dashed lines are at 20 hours.

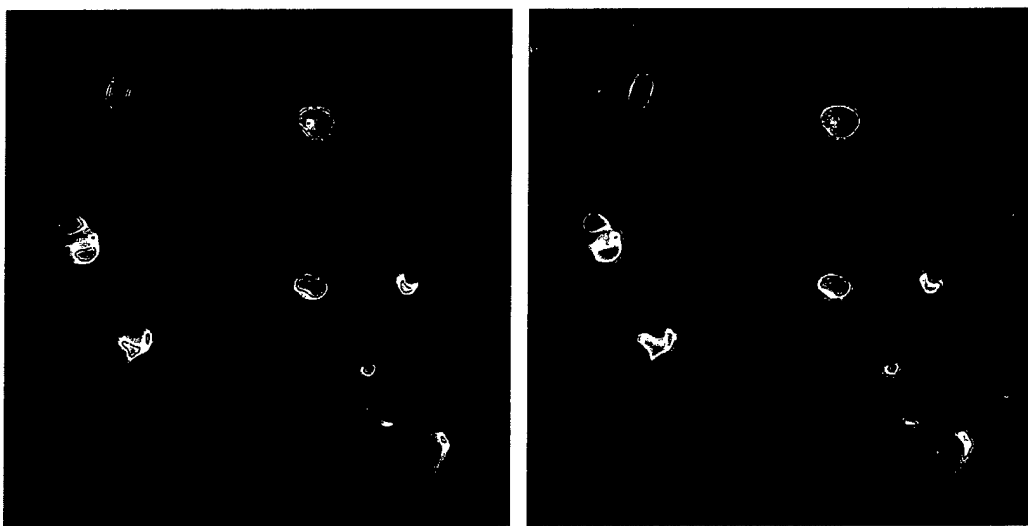


Figure 27. Horizontal cross-sections of temperature (left panel) and salinity (right panel) from gsea3.2 at mid-depth (400m). Box is 2.56km on a side. Contour intervals are $.1^{\circ}\text{C}$ and $.006 \text{ psu}$ respectively. Blue areas are the relatively cool and fresh detraining plumes.

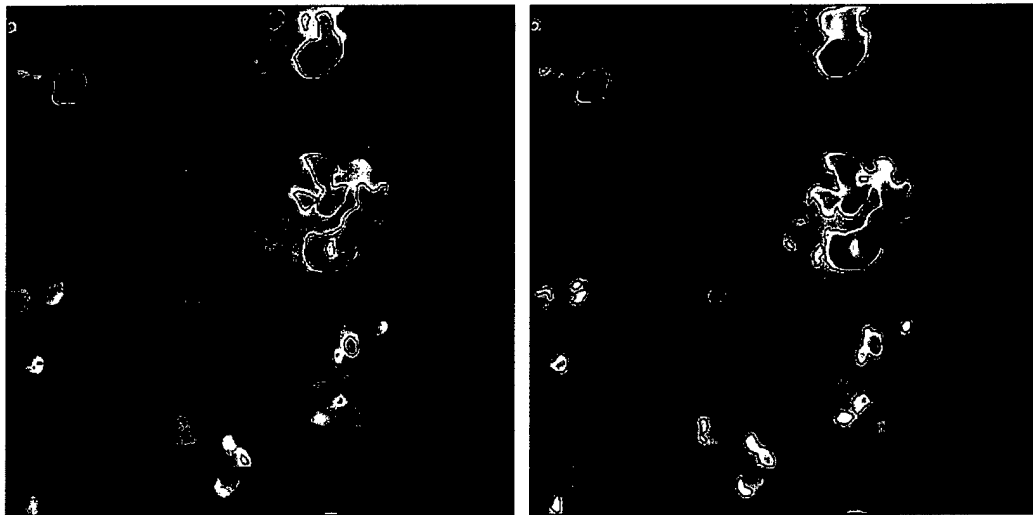


Figure 28. Horizontal cross-sections of temperature (left panel) and salinity (left panel) from gstrat2 at mid-depth (400m). Box is 2.56km on a side. Contour intervals are $.1^{\circ}\text{C}$ and $.006 \text{ psu}$ respectively. Blue areas are the relatively cool and fresh detraining plumes.



Figure 29. Vertical cross-section of vertical velocity from gsea3.2. Box is 2.56km wide by 800m deep. Contour interval is .02 m/s. Blue areas are the downward velocities of detraining plumes.

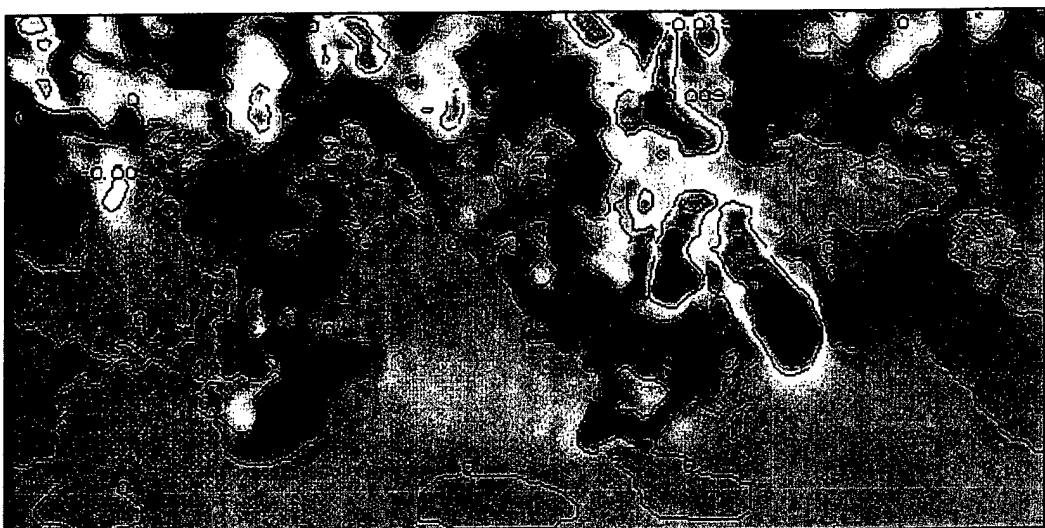


Figure 30. Vertical cross-section of vertical velocity from gstrat2. Box is 2.56km wide by 800m deep. Contour interval is .01 m/s. Blue areas are the downward velocities of detraining plumes.

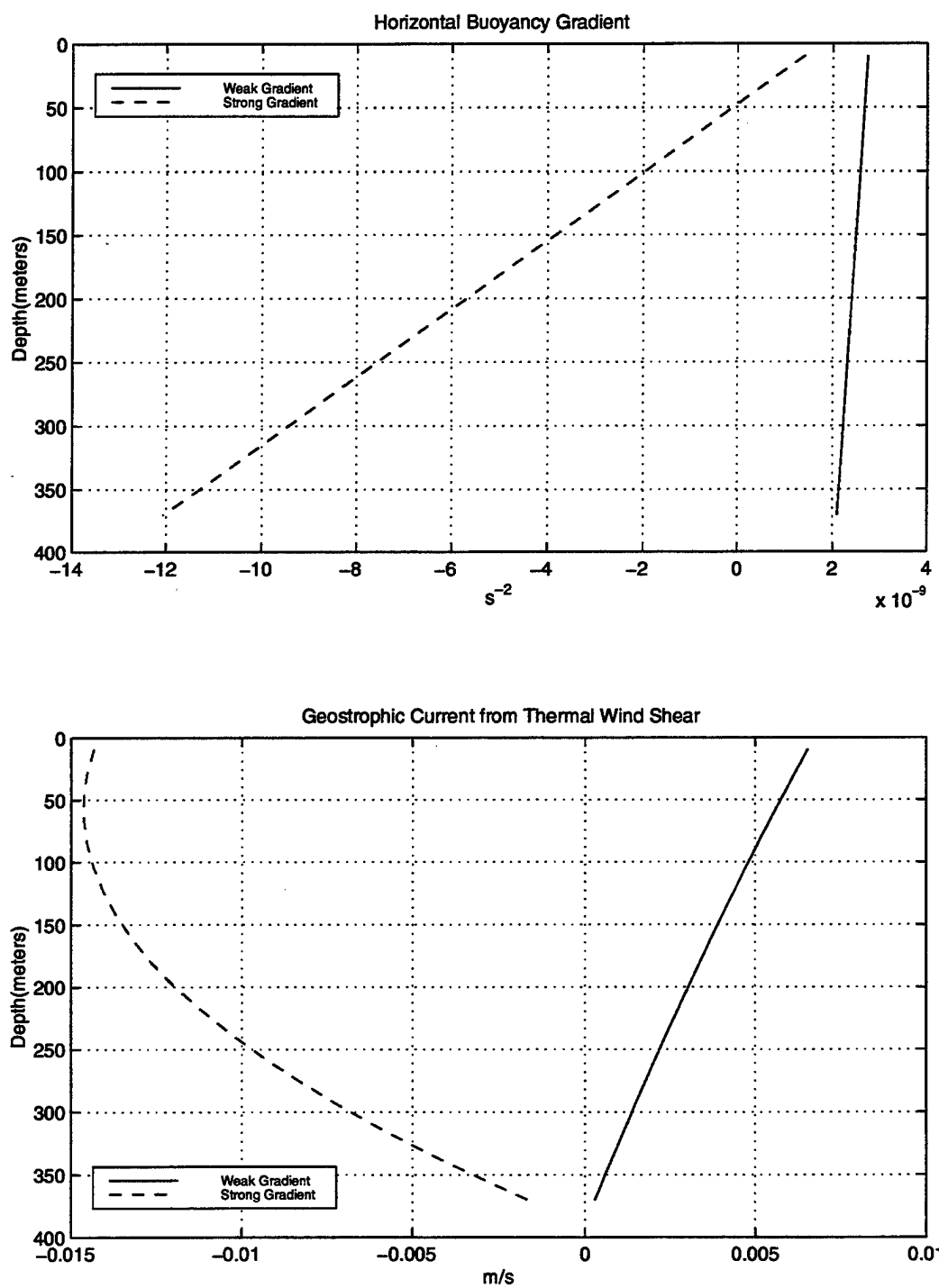


Figure 31. Conditions used in the horizontal gradient experiments. Top: Buoyancy Gradient as a function of depth. Bottom: Geostrophic Velocity resulting from thermal wind shear.

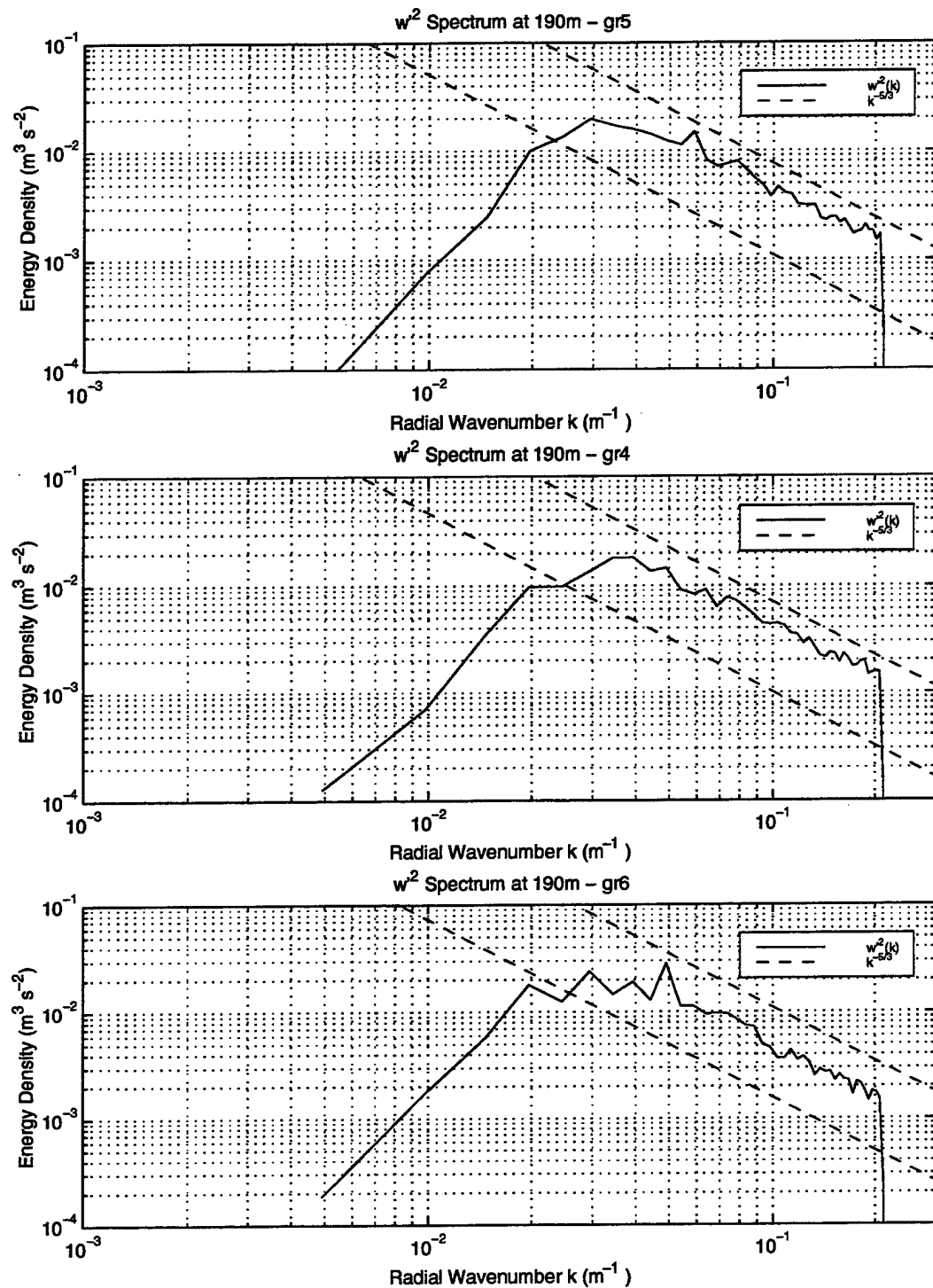


Figure 32. Energy-density spectra for vertical velocity at 190m 67 hours after cooling begins. Top: No Gradient (gr5) Center: Weak Gradient (gr4) Bottom: Strong Gradient (gr6)

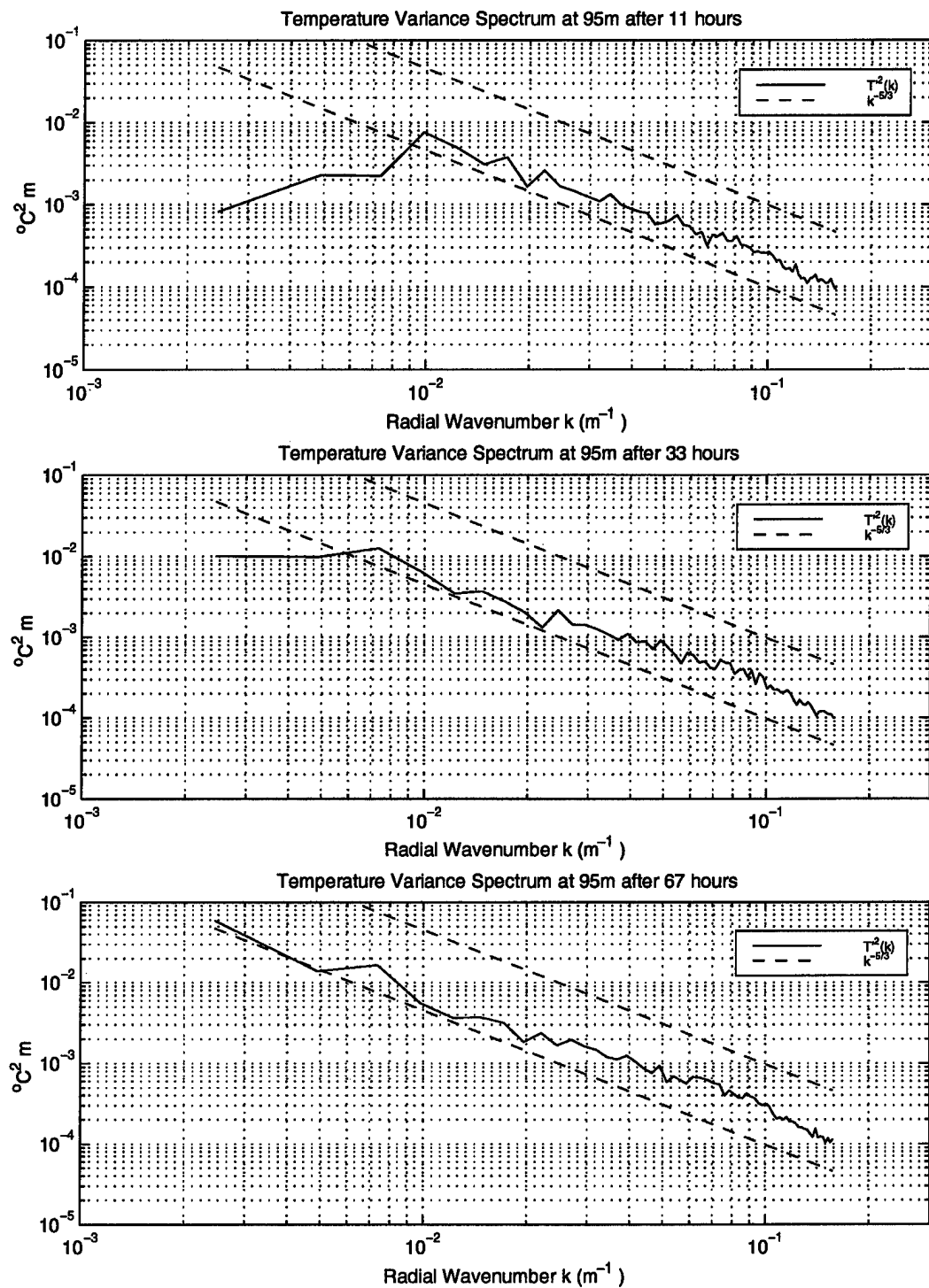


Figure 33. Temperature variance spectra at 190m at progressive times after cooling begins. Top: After 11 hours. Center: After 33 hours. Bottom: After 67 hours.

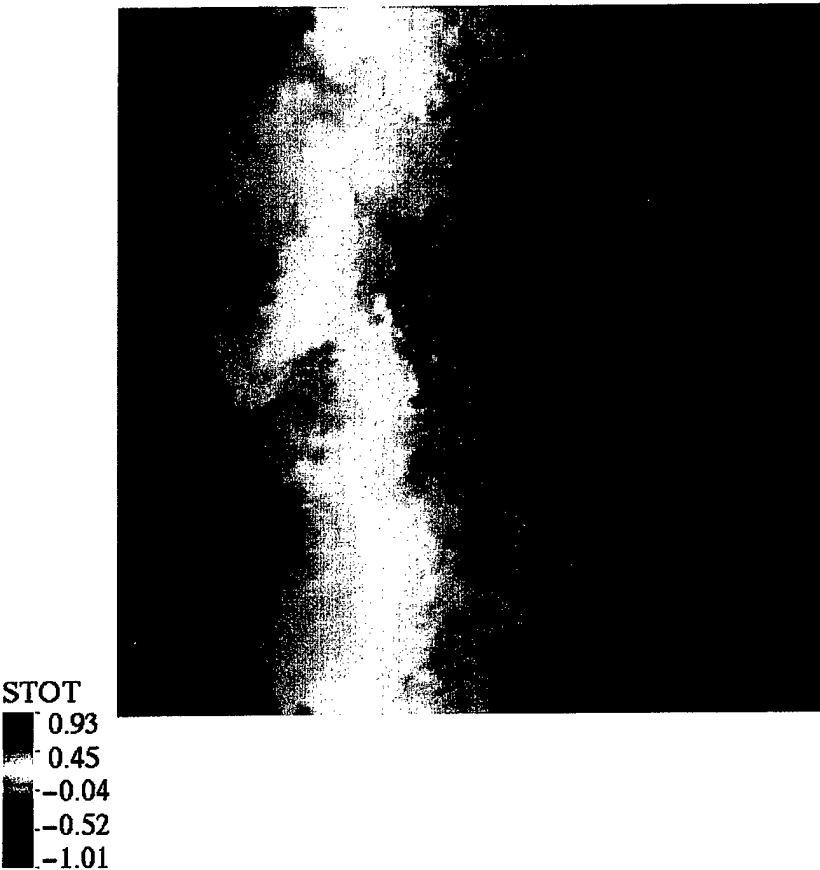


Figure 34. LES Salinity at a depth of 40m from the weak gradient experiment. Box is 2.56km on a side. The color scale is $(S-34.85)e-3$ psu.

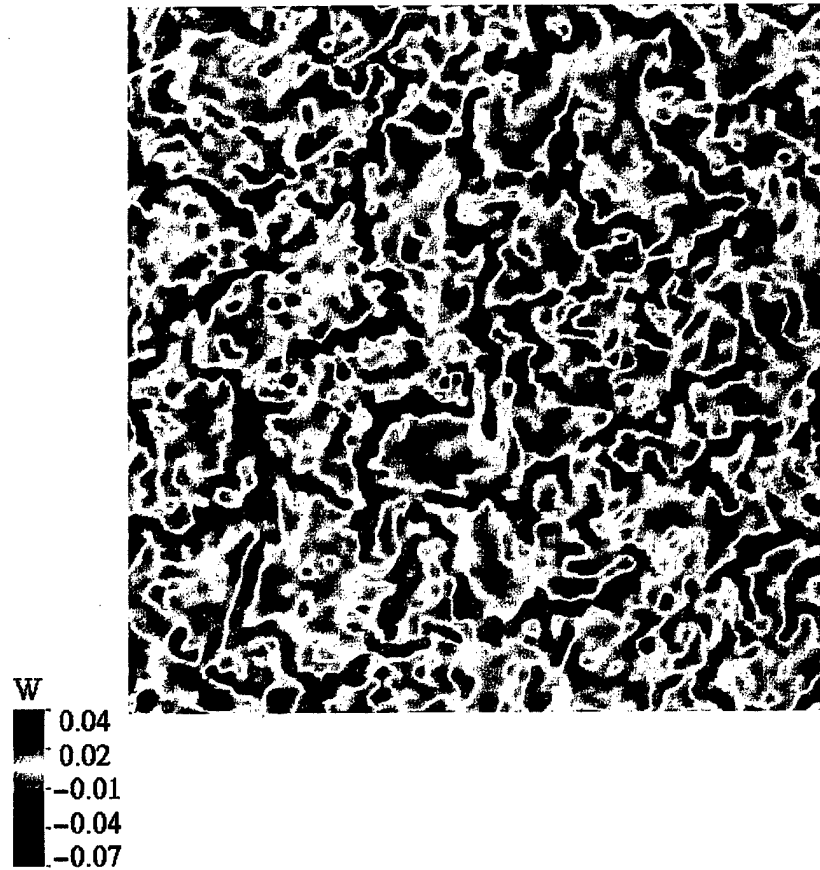


Figure 35. LES Vertical Velocity at a depth of 40m from the weak gradient experiment. Box is 2.56km on a side. The color scale is in m/s.

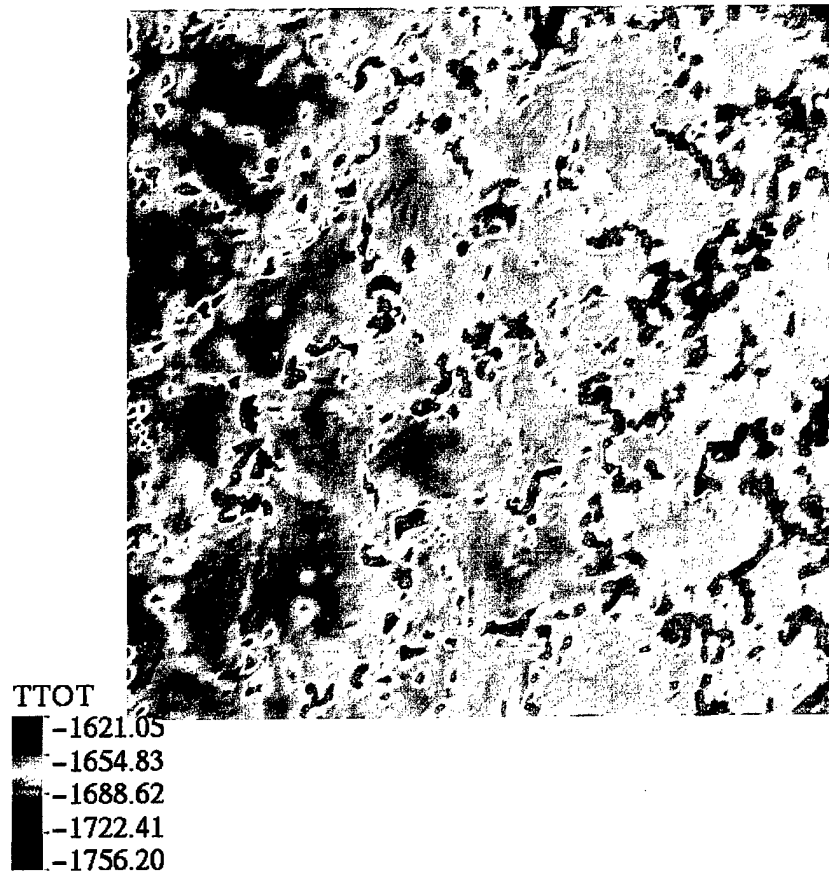


Figure 36. LES Temperature at a depth of 40m from the weak gradient experiment. Box is 2.56km on a side. The color scale is in $^{\circ}\text{C}$ -3.

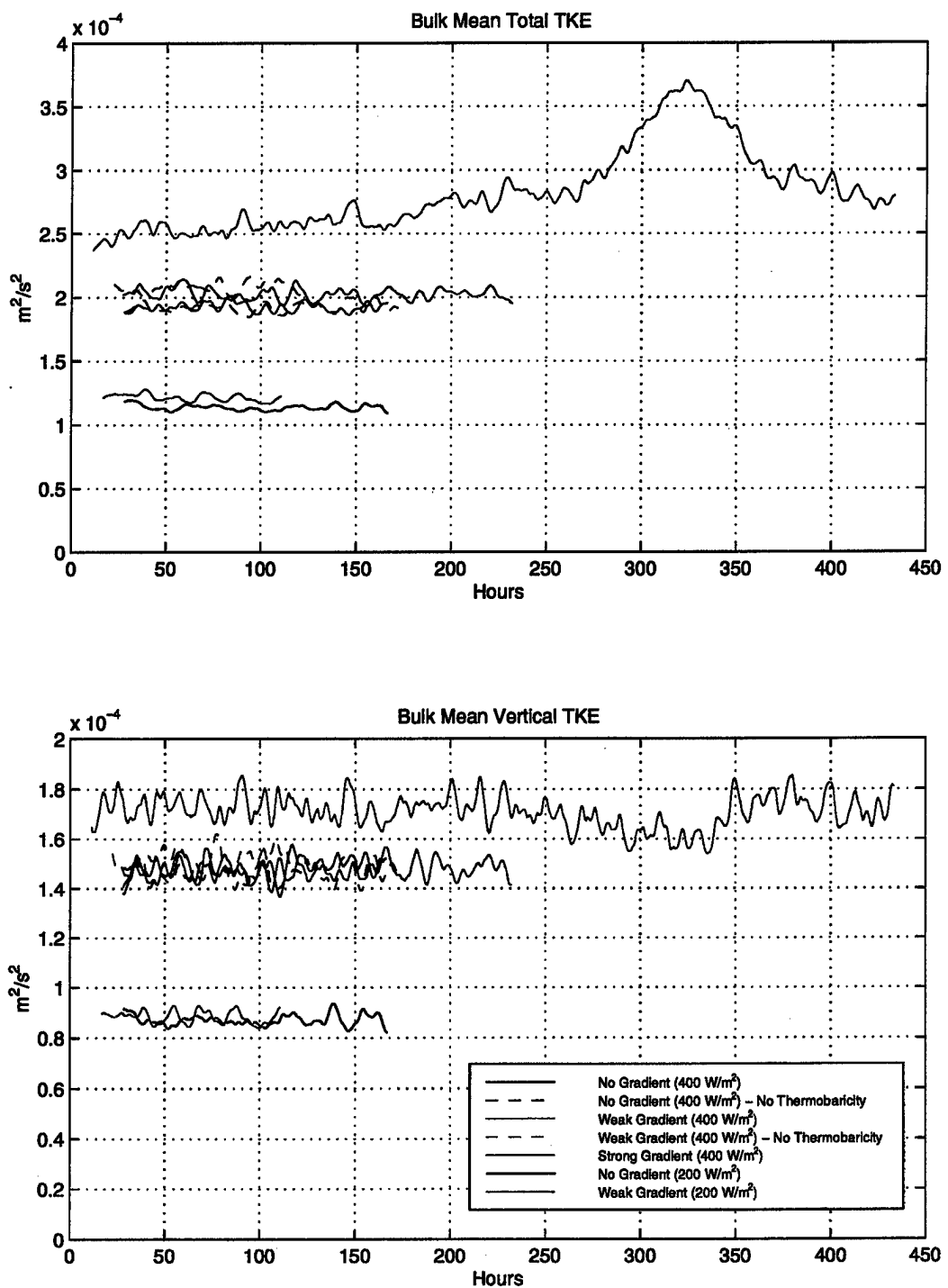


Figure 37. Bulk Mean Turbulent Energy as a function of time. Top: Total TKE. Bottom: Vertical component of TKE.

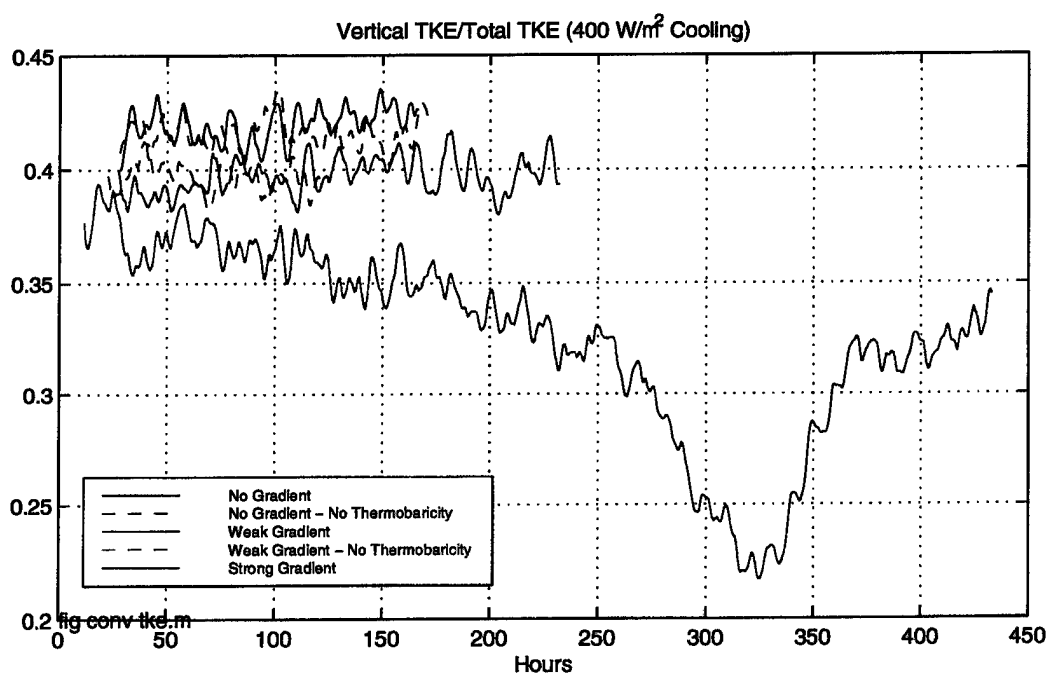
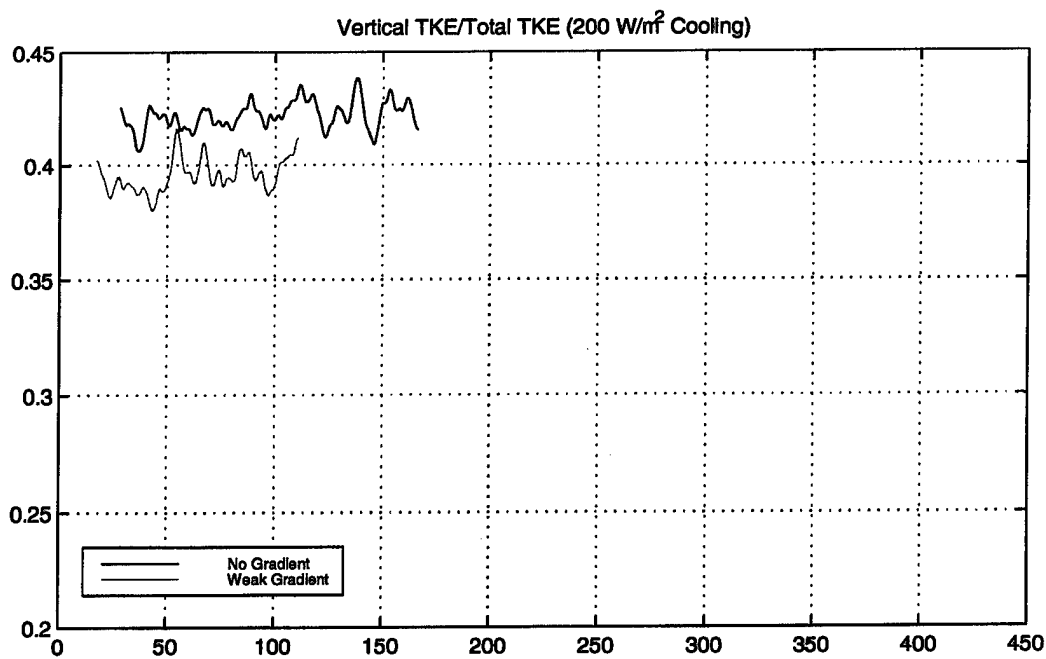


Figure 38. Ratio of Vertical to Total TKE.

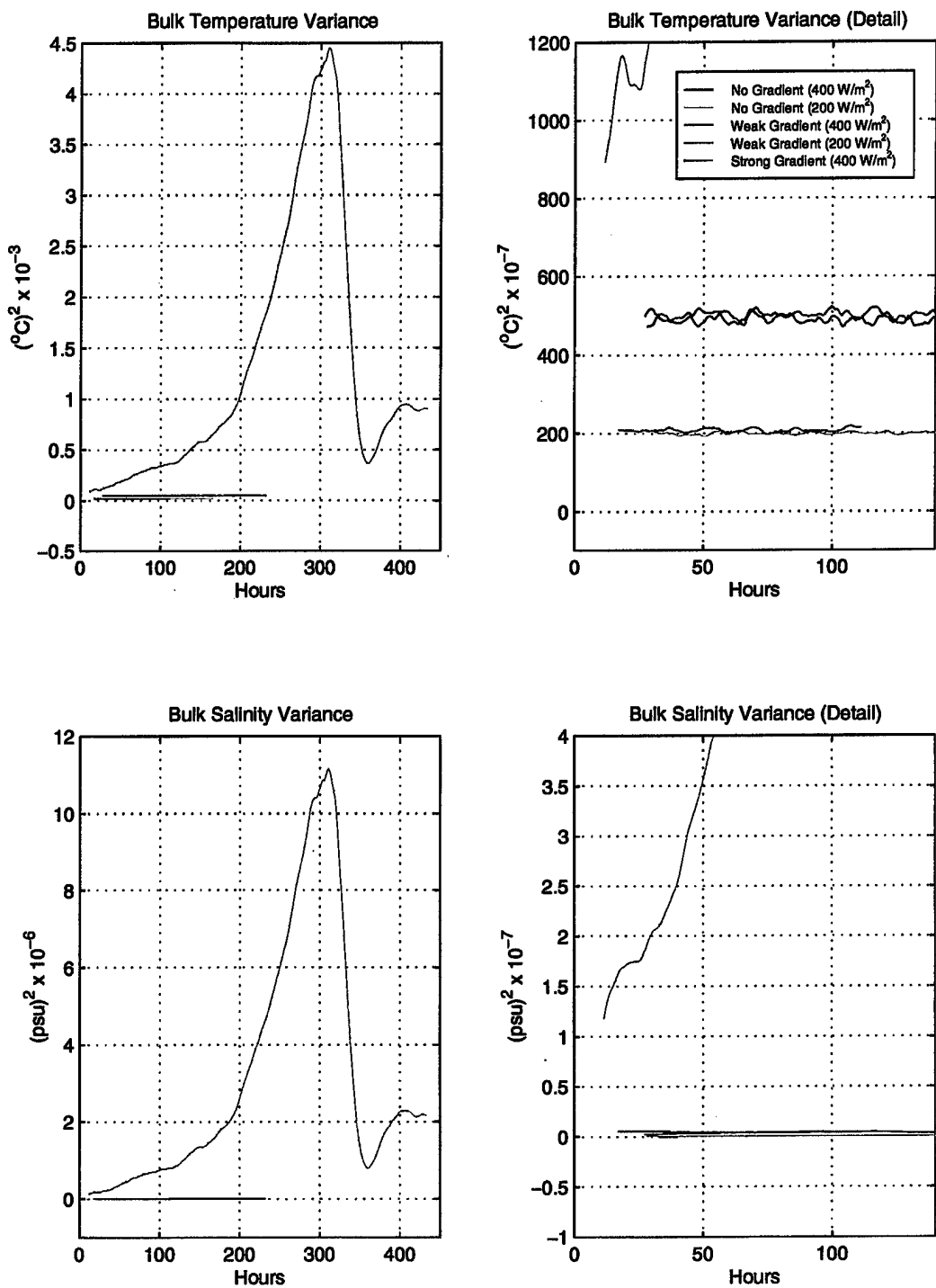


Figure 39. Bulk Temperature and Salinity Variances from horizontal means.

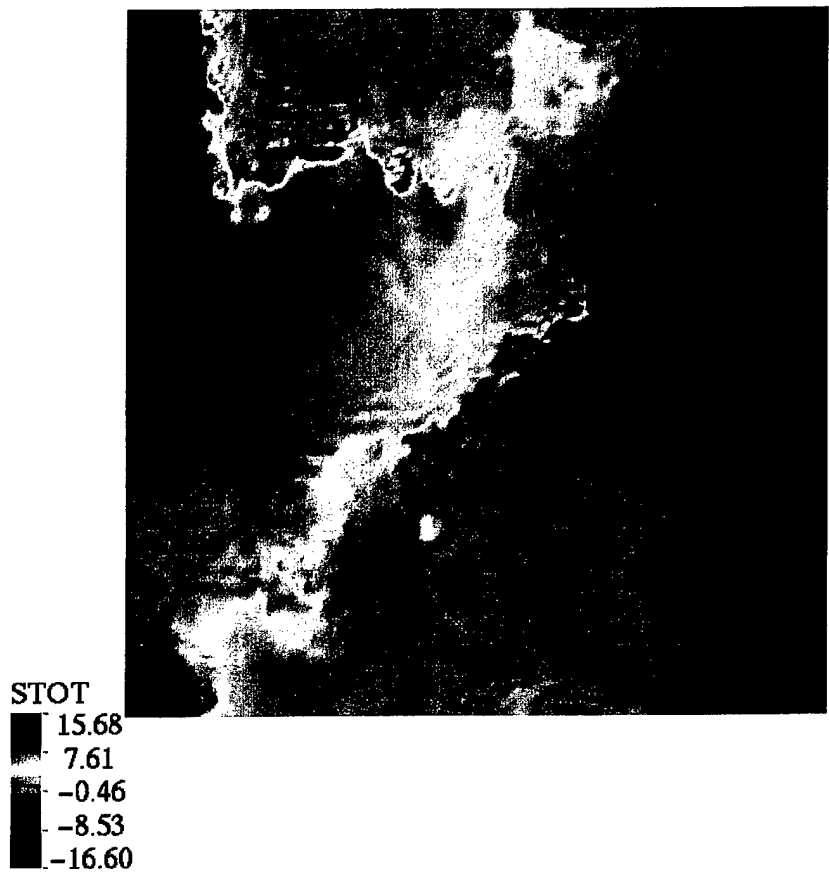


Figure 40. LES Salinity at 20m depth from the strong gradient experiment when the box mode is large. Box is 2.56km on a side. The color scale is in $(S-34.85)e-3$ psu.

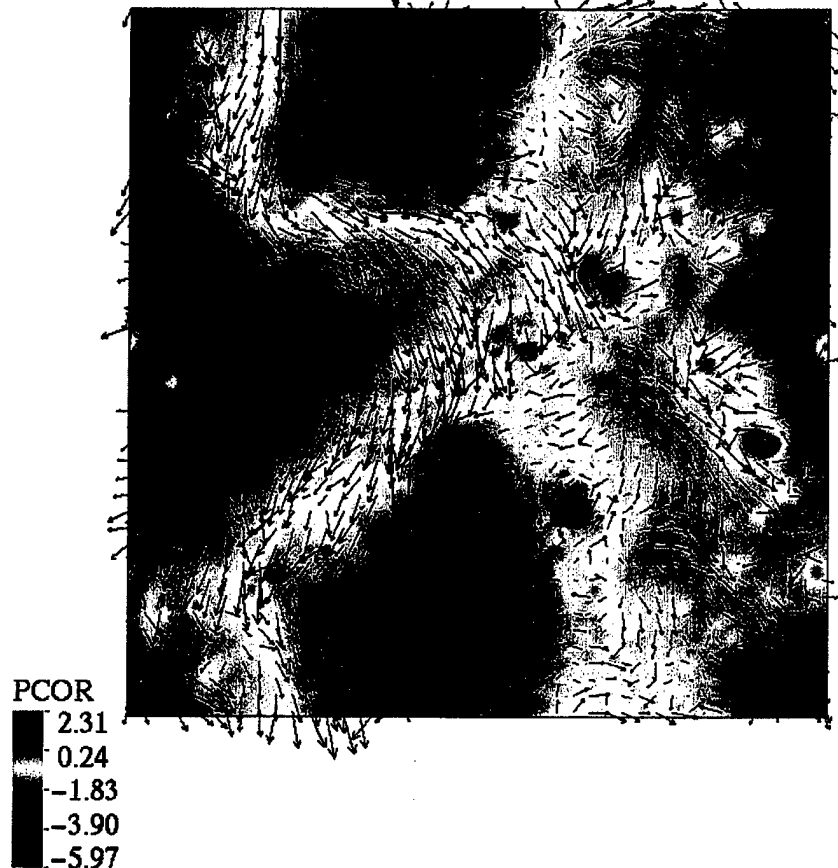


Figure 41. LES nonhydrostatic pressure per unit density and horizontal flow fields at 20m depth from the strong gradient experiment when the box mode is large. Box is 2.56km on a side. The color scale is in $m^2 s^{-2} e^{-3}$. The longest arrows represent horizontal speeds of 9 cm/s.

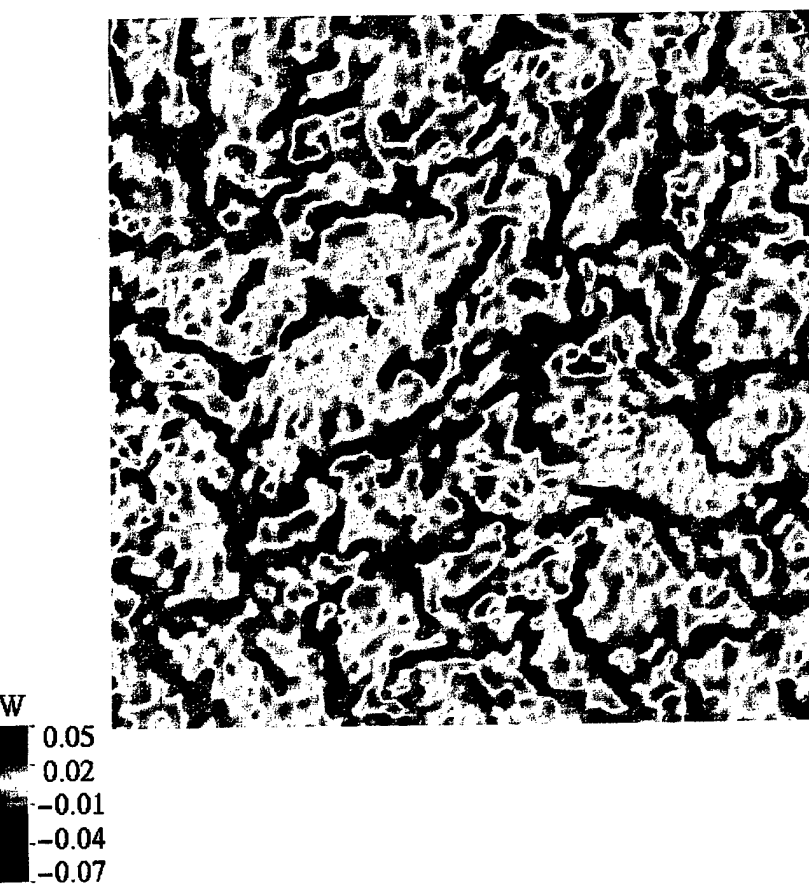


Figure 42. LES Vertical Velocity at 20m depth from the strong gradient experiment when the box mode is large. Box is 2.56km on a side. The color scale is in m/s e-3.

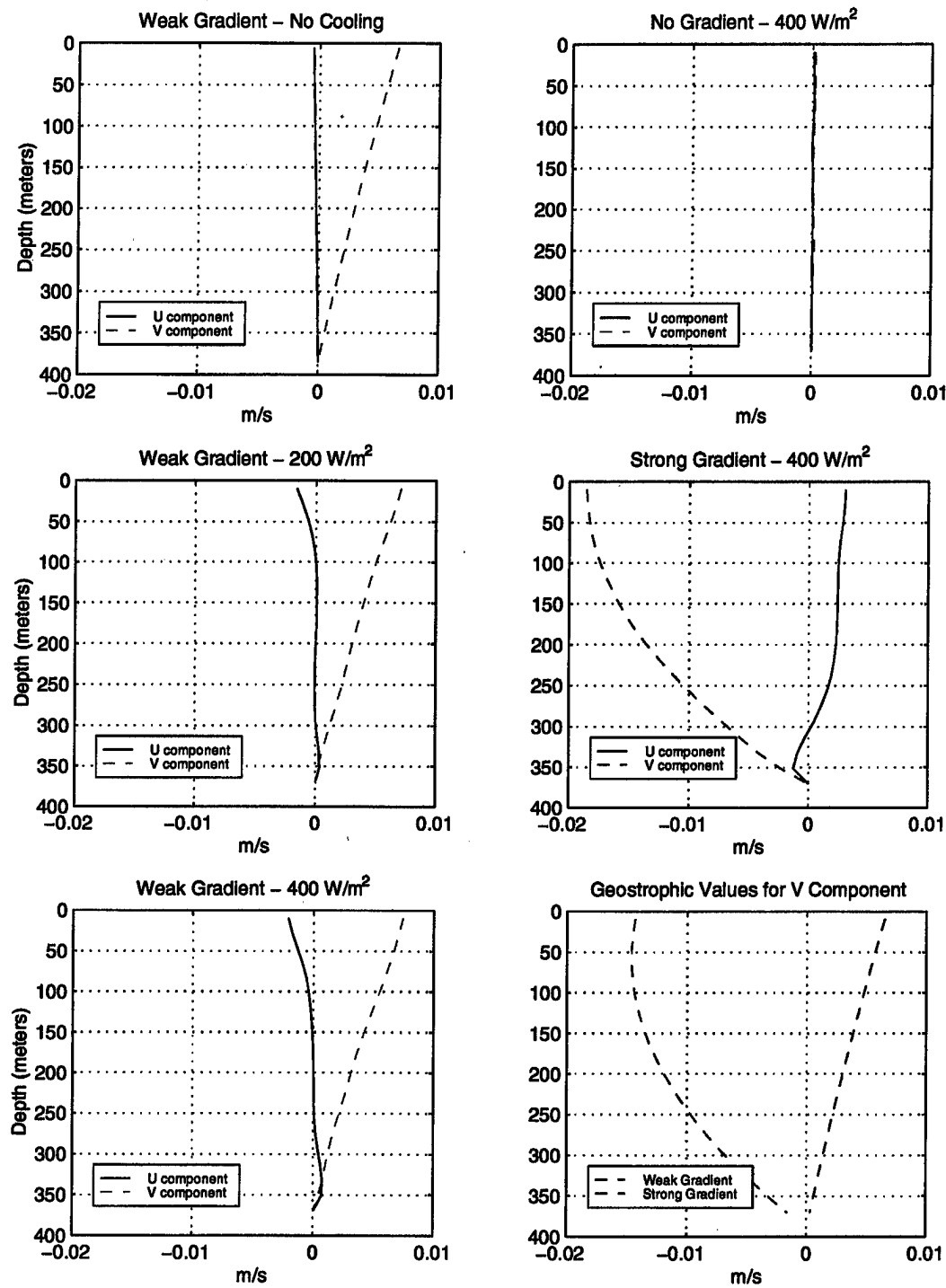
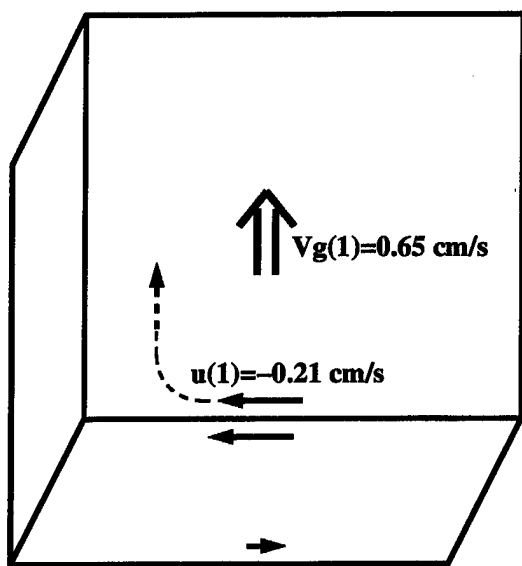


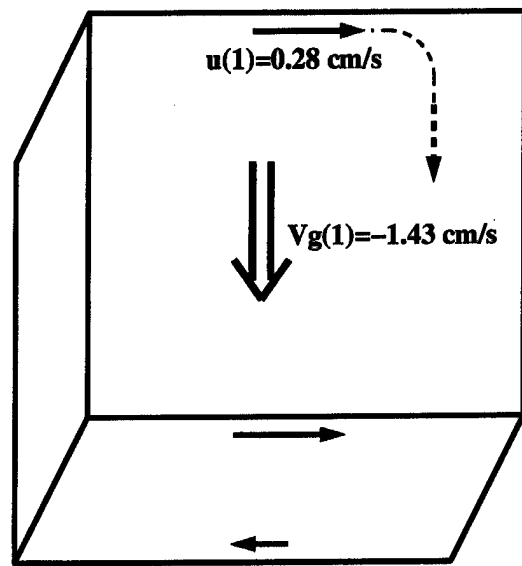
Figure 43. Mean Velocity Profiles.

WEAK GRADIENT



$$v_{\text{LES}}(1)=0.74 \text{ cm/s}$$

STRONG GRADIENT



$$v_{\text{LES}}(1)=-1.87 \text{ cm/s}$$

Figure 44. Schematic showing enhancement of geostrophic currents.

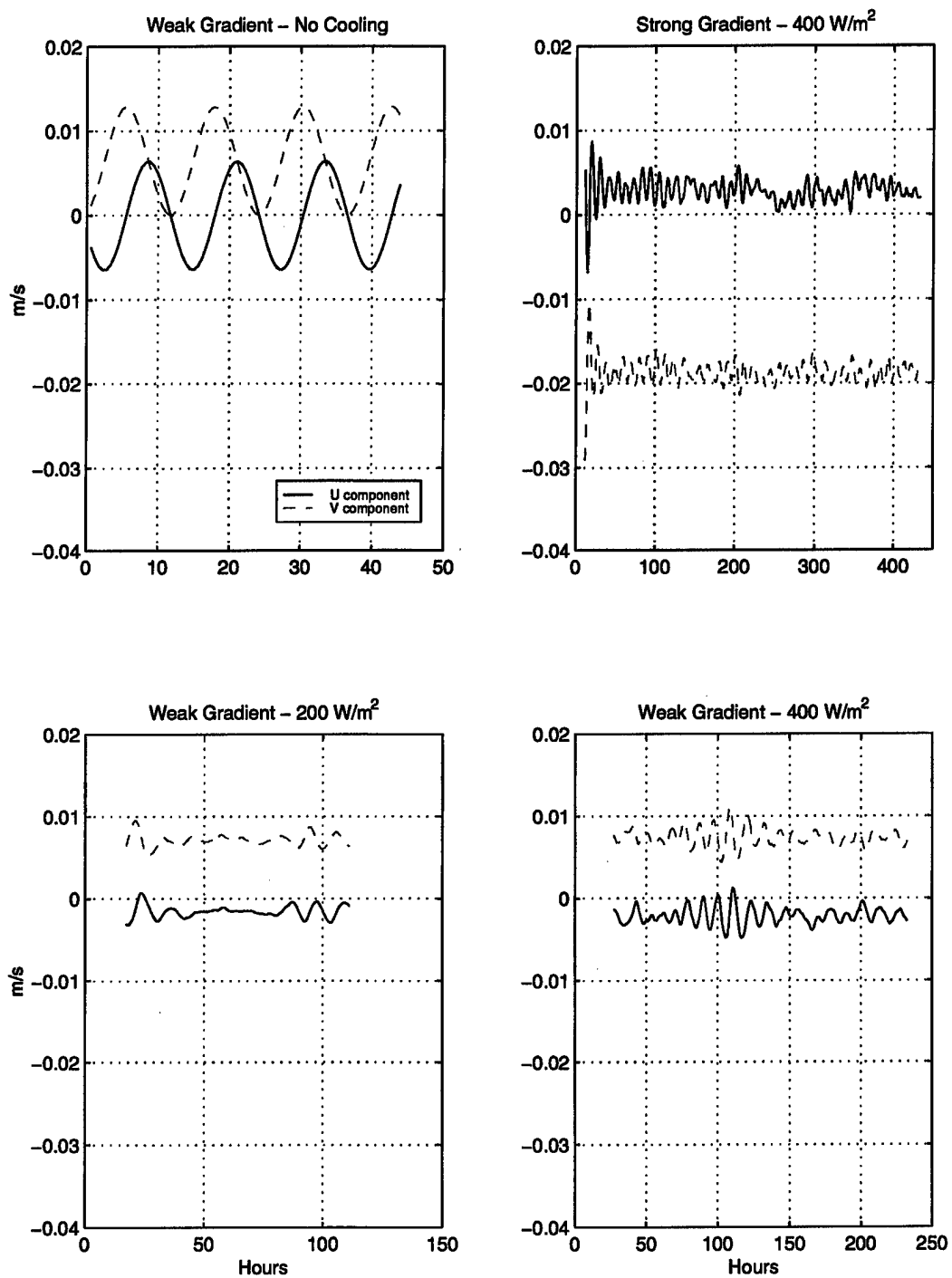


Figure 45. Horizontal-mean Velocity at the first grid level.

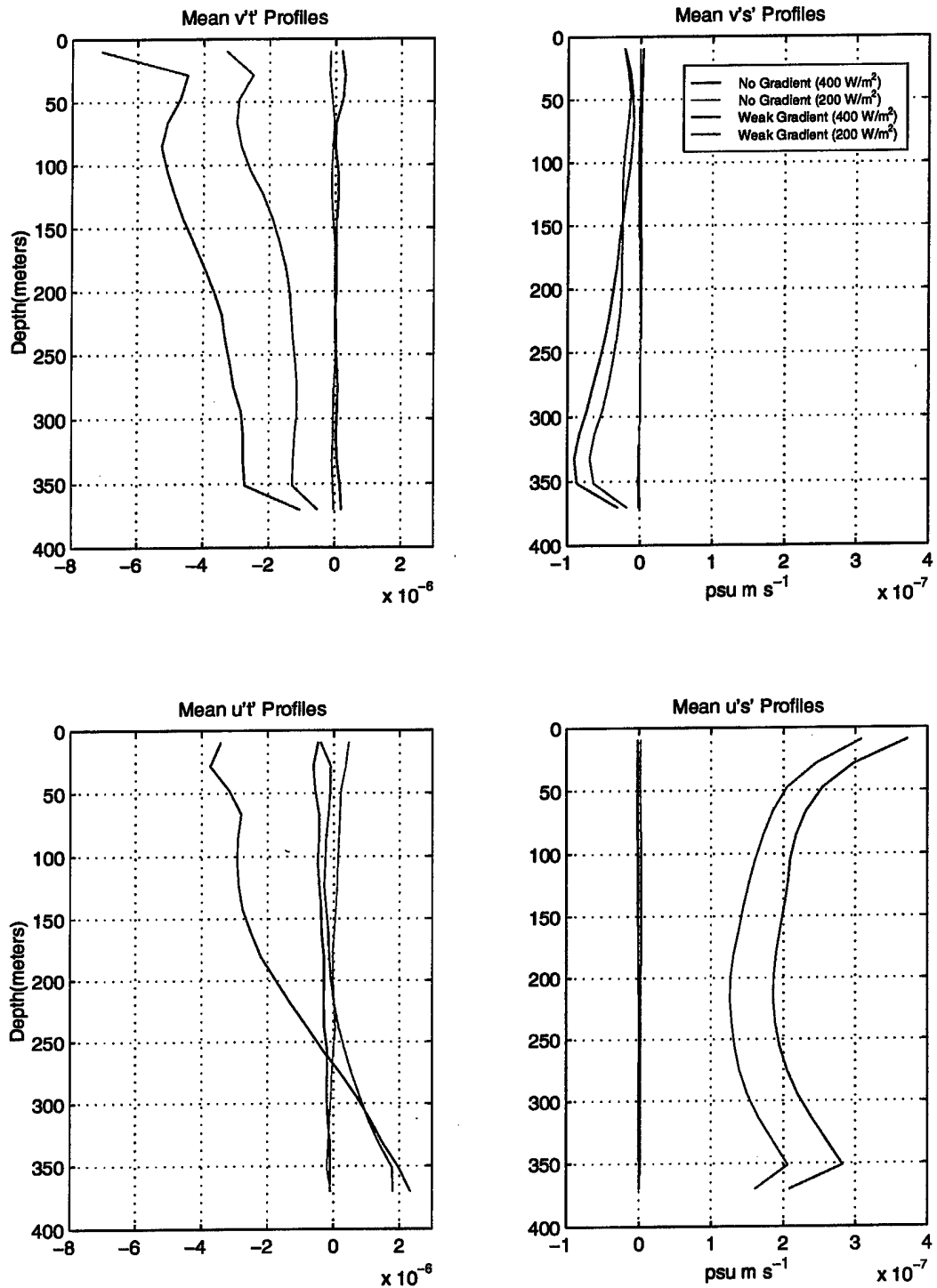


Figure 46. Horizontal Flux Profiles.

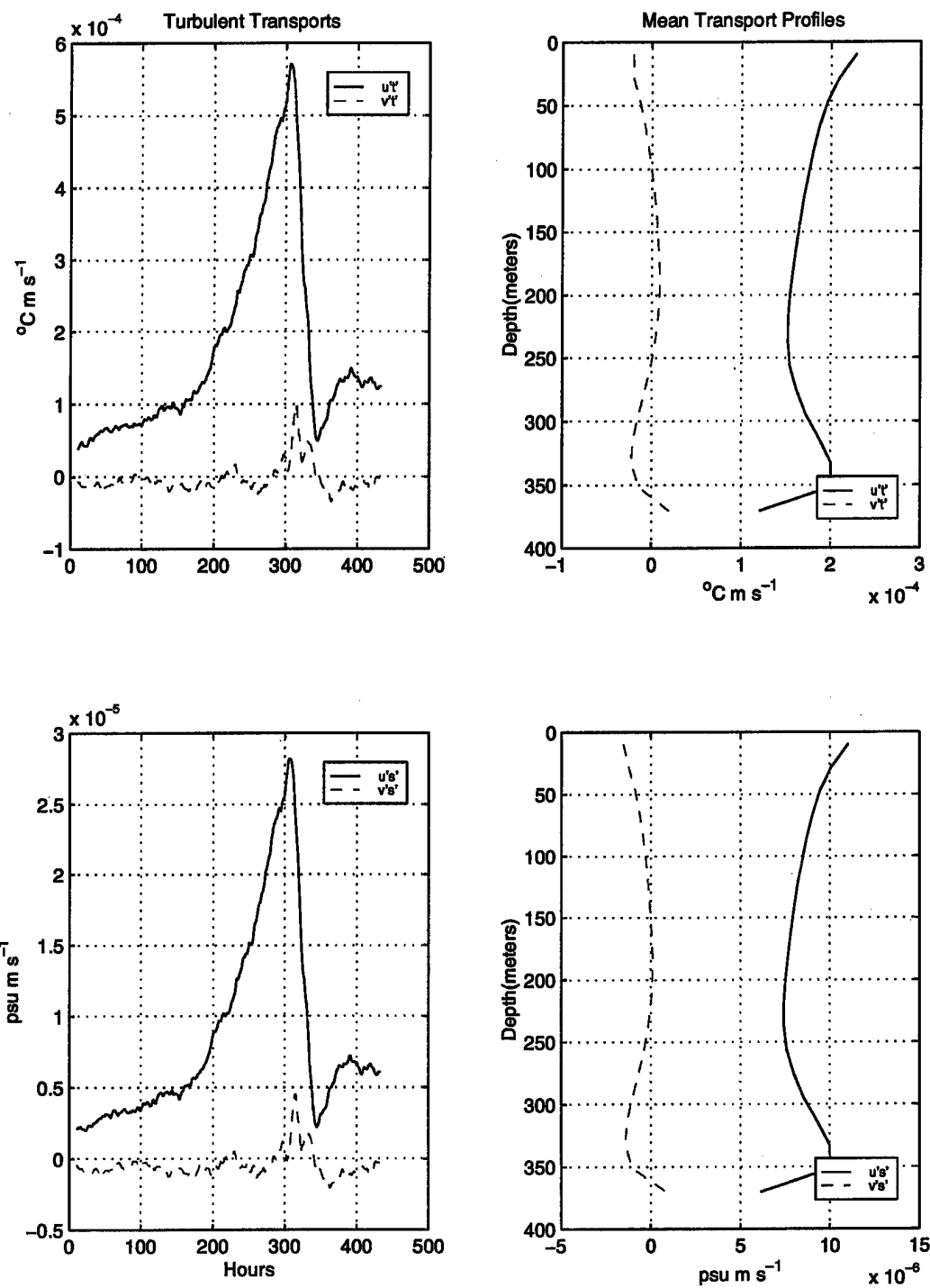


Figure 47. Horizontal Flux plots for the Strong Gradient case.

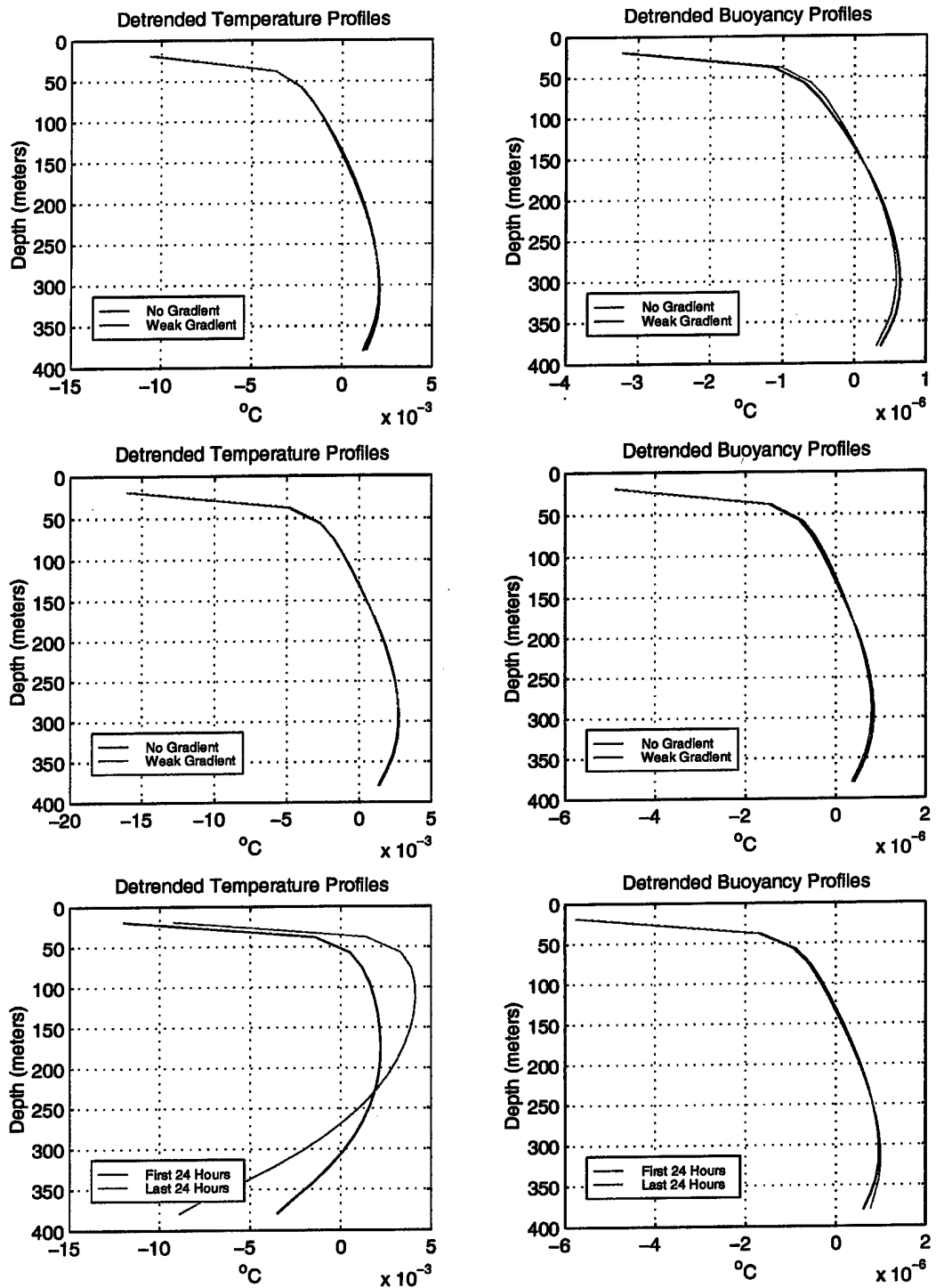


Figure 48. Profiles of detrended temperature and potential buoyancy. Top left and right are from the experiments with 200 W/m^2 . Center left and right are from the experiments with 400 W/m^2 . Bottom left and right are from the experiment with the strong gradient and 400 W/m^2 .

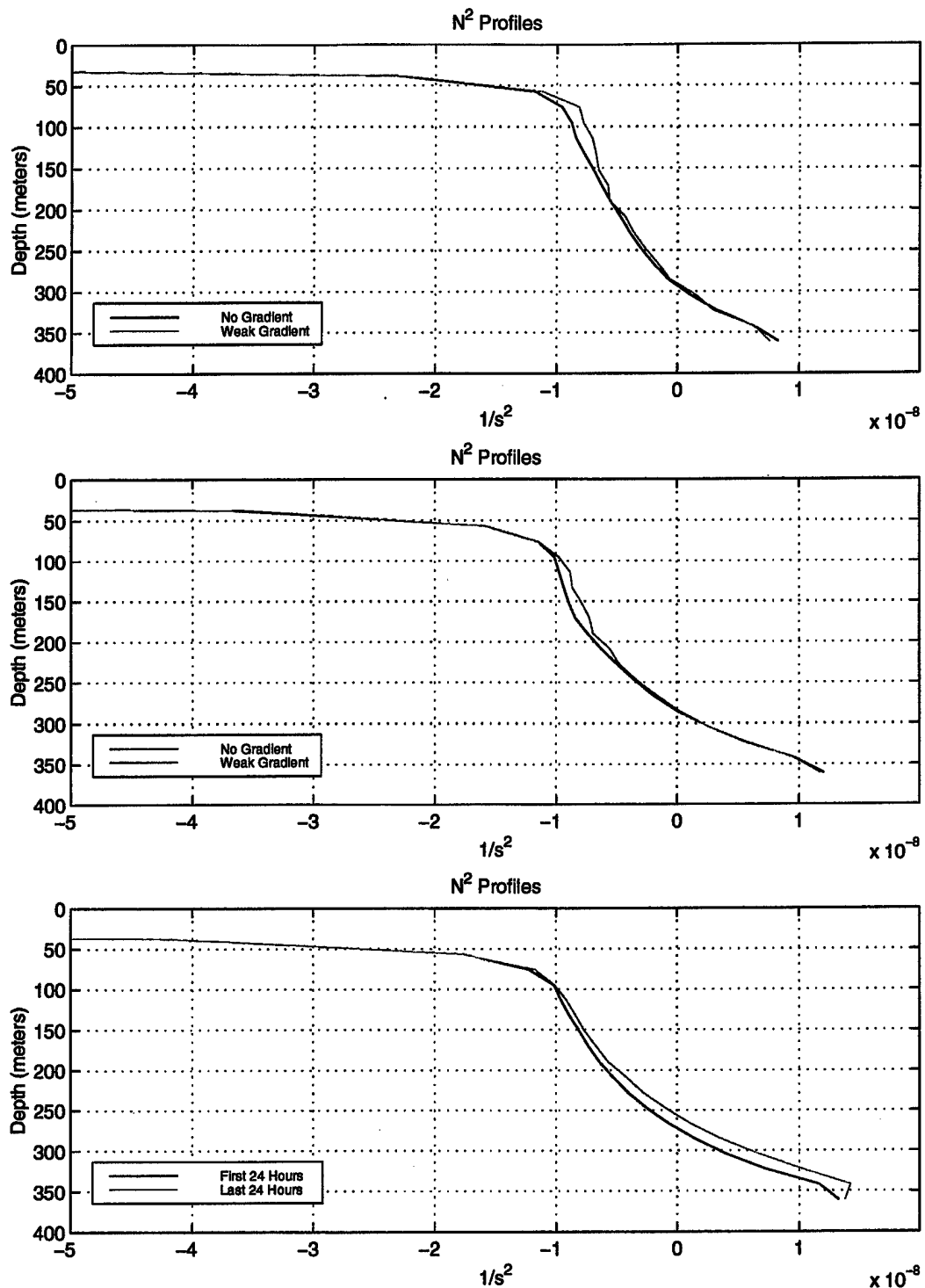


Figure 49. Stability (N^2) Profiles. Top is from the experiments with 200 W/m^2 . Center is from the experiments with 400 W/m^2 . Bottom is from the experiment with the strong gradient and 400 W/m^2 .

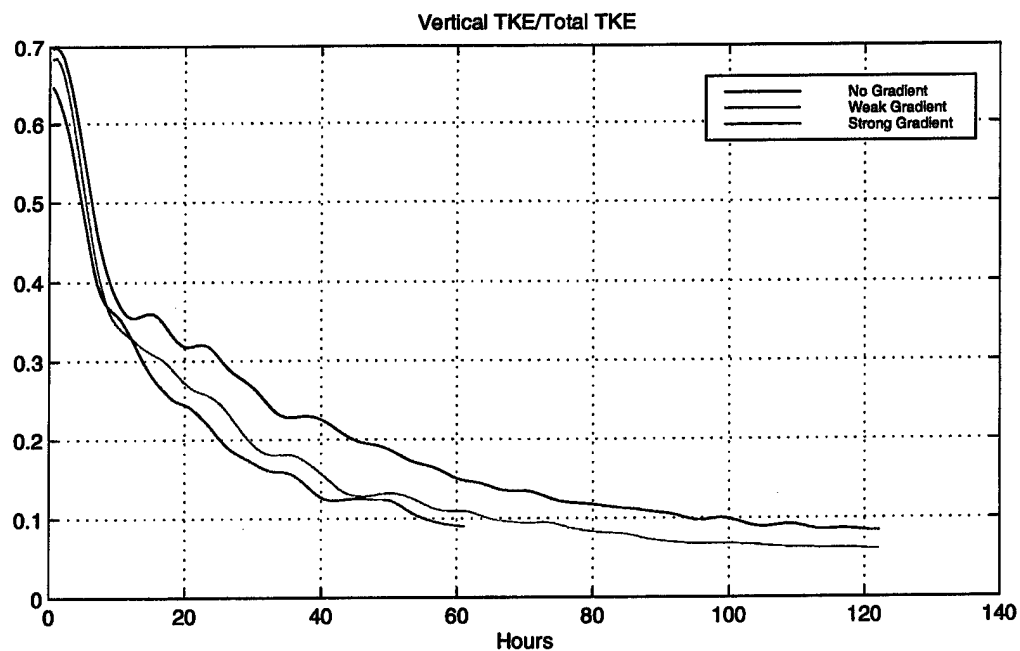
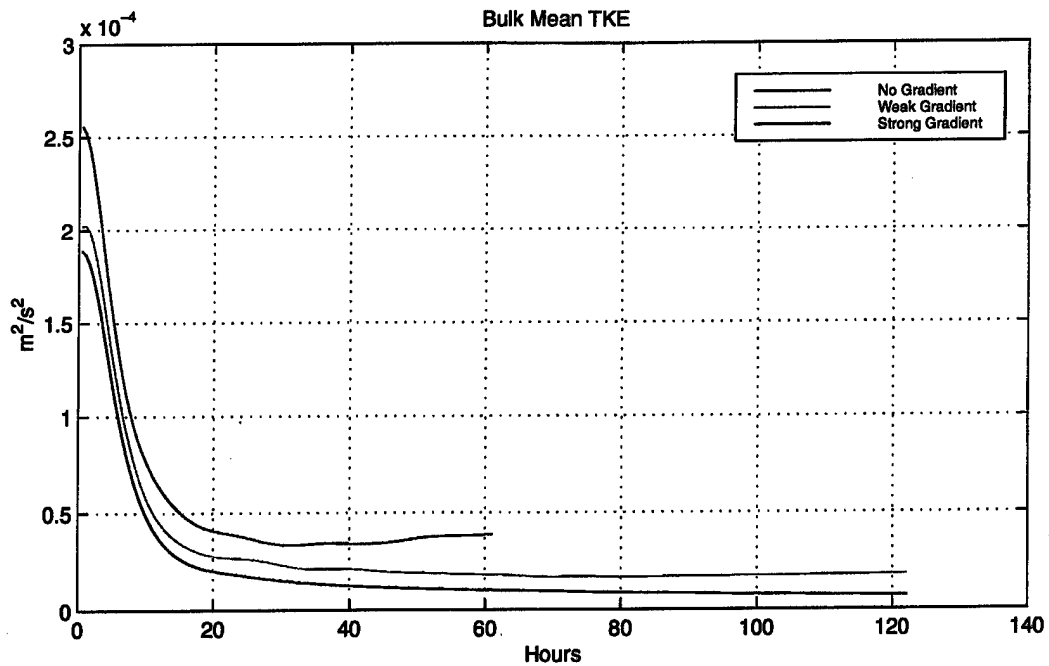


Figure 50. Postconvection Plots of TKE behavior in time. Top: Bulk Mean TKE
Bottom: Vertical TKE/Total TKE

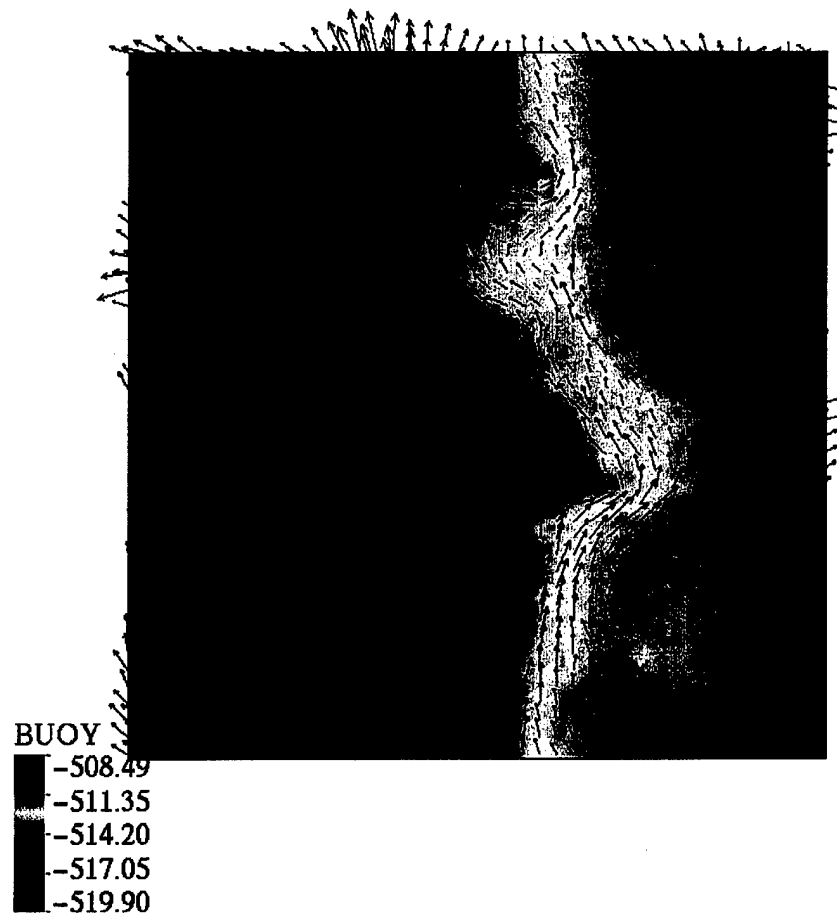


Figure 51. Potential buoyancy and horizontal flow 40m below the surface in the weak gradient experiment 48 hours after cooling stops. Box is 2.56km on a side. Color scale is in $\text{m/s}^2 \text{ e-3}$. The longest arrows represent horizontal speeds of 3 cm/s.

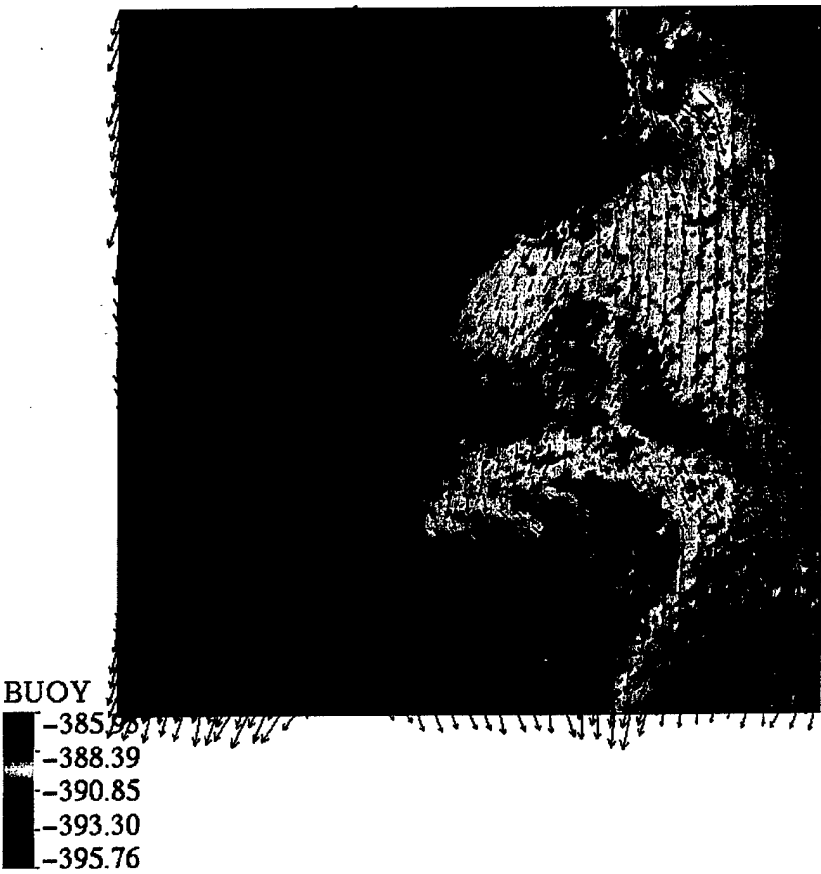


Figure 52. Potential buoyancy and horizontal flow 40m below the surface in the strong gradient experiment 48 hours after cooling stops. Box is 2.56km on a side. Color scale is in $\text{m/s}^2 \text{ e-3}$. The longest arrows represent horizontal speeds of 3.5 cm/s.

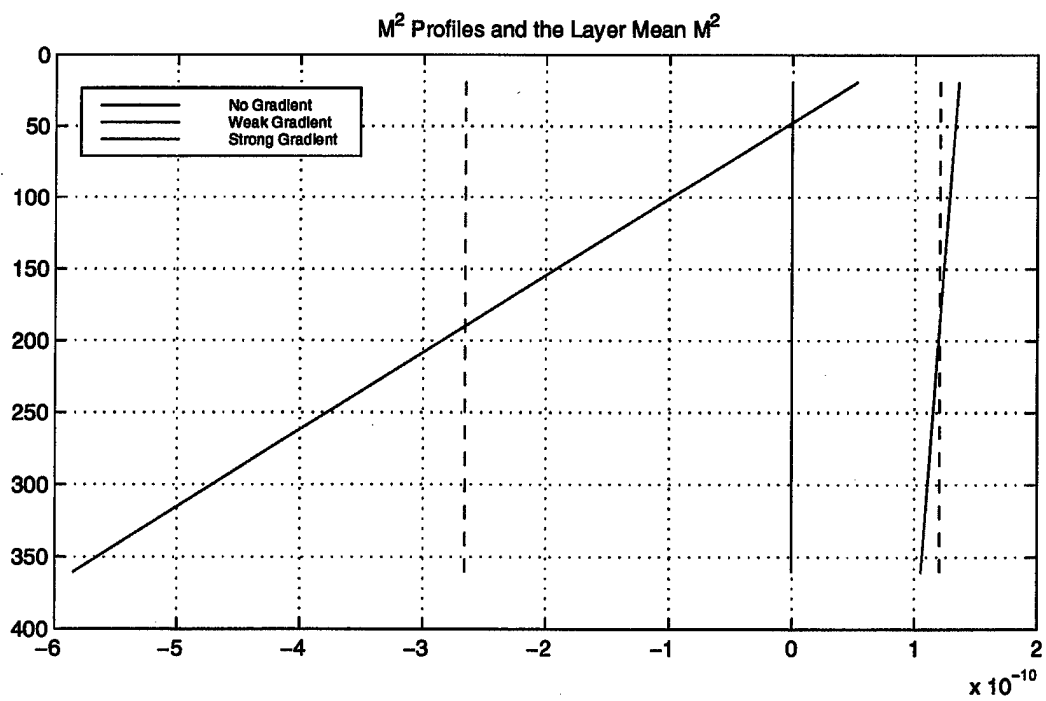
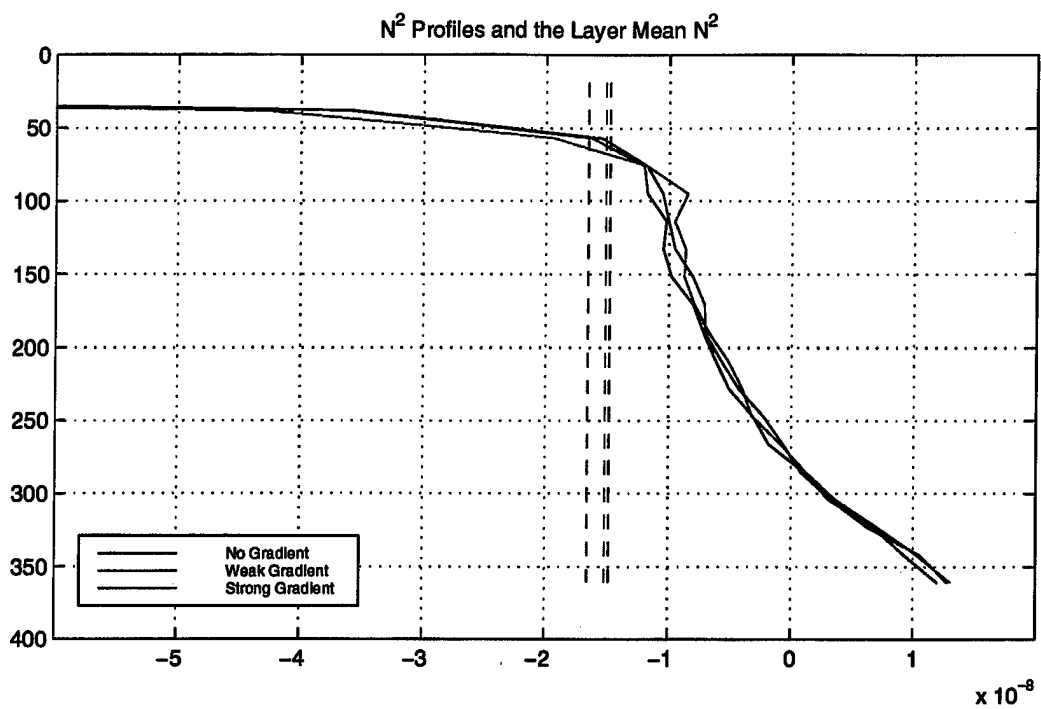


Figure 53. Postconvection Plots of N^2 and M^2 profiles 55 hours after cooling stops. Dashed lines are bulk averages.

INITIAL DISTRIBUTION LIST

1. Defense Technical Information Center 2
8725 John J. Kingman Rd., STE 0944
Ft. Belvoir, VA 22060-6218
2. Dudley Knox Library 2
Naval Postgraduate School
411 Dyer Rd.
Monterey, CA 93943-5101
3. Chairman, Code OC/Gd 1
Department of Oceanography
Naval Postgraduate School
Monterey, CA 93943-5101
4. Prof. Roland W. Garwood, Code OC/Gd 2
Department of Oceanography
Naval Postgraduate School
Monterey, CA 93943-5101
5. Prof. Peter S. Guest, Code MR/Gs 1
Department of Meteorology
Naval Postgraduate School
Monterey, CA 93943-5101
6. Mr. Ramsey Harcourt, Code OC/Ha 2
Department of Oceanography
Naval Postgraduate School
Monterey, CA 93943-5101
7. Prof. Albert J. Semtner, Code OC/Se 1
Department of Oceanography
Naval Postgraduate School
Monterey, CA 93943-5101
8. Prof. Wieslaw Maslowski, Code OC/Ma 1
Department of Oceanography
Naval Postgraduate School
Monterey, CA 93943-5101

9.	Dr. Pascale Lherminier, Code OC/Lh	1
	Department of Oceanography	
	Naval Postgraduate School	
	Monterey, CA 93943-5101	
10.	Office of Naval Research	1
	800 North Quincy Street, Ballston Tower One	
	Arlington, VA 22217-5660	
11.	Office of Naval Research	1
	Code 322OM	
	ATTN: Dr. Manual Fiadeiro	
	800 North Quincy Street	
	Arlington, VA 22217-5660	
12.	Office of Naval Research	1
	Code 322OM	
	ATTN: Dr. Terri Paluszakiewicz	
	800 North Quincy Street	
	Arlington, VA 22217-5660	
13.	Office of Naval Research	1
	Code 322PO	
	ATTN: Dr. Lou Goodman	
	800 North Quincy Street	
	Arlington, VA 22217-5660	
14.	Mr. Alan Hayashida	1
	NUWC DET Arctic Submarine Laboratory	
	48750 Fleming Rd.	
	San Diego, CA 92152-7210	
15.	National Science Foundation	1
	Office of Polar Programs	
	ATTN: Dr. Mike Ledbetter	
	4201 Wilson Blvd.	
	Arlington, VA 22230	
16.	Dr. Fiammetta Straneo	1
	School of Oceanography	
	University of Washington, Box 357940	
	Seattle, WA 98195-7940	

17. Prof. Toshiyuki Awaji 1
Department Of Geophysics,
Faculty of Science
Kyoto University
Kyoto 606-8502
JAPAN

18. LCDR Rebecca E. Stone 3
USS Boxer (LHD-4)
OPS DEPT
FPO AP 96661-1663